RADIATIVE CAPTURE OF PROTONS BY C^{12} AND C^{13} BELOW 700 KEV

Thesis by

Joseph L. Vogl

In Partial Fulfillment of the Requirements

for the Degree of

Doctor of Philosophy

California Institute of Technology

Pasadena, California

1963

ACKNOWLEDGMENTS

The author wishes to express his gratitude and thanks to the entire staff and personnel of the Kellogg Radiation Laboratory for their kind assistance during the course of this work. He is especially indebted to Professor William A. Fowler who suggested the problem and guided the work, to Professor Ward Whaling for many useful discussions and to Dr. Dale F. Hebbard for his assistance during the early part of these investigations. Special thanks are also expressed to Barbara A. Zimmerman for her help with many of the computations.

The author is also grateful for the graduate fellowships received from the National Science Foundation, the Ramo-Wooldridge Corporation, and the Electro-Optical Systems. He wishes to thank the Office of Naval Research and the U. S. Atomic Energy Commission for their joint program which financially supported this research and which provided personal financial support through Graduate Research Assistantships.

ABSTRACT

The radiative capture of protons by C^{13} has been investigated using anticoincidence techniques down to a laboratory energy of 92 kev, but no new levels are found that would influence the cross section at stellar energies. An upper limit is placed on the strength of radiative capture by any missed levels. From several of the same targets used for the $C^{13}(p, \gamma)$ measurements the yield of $C^{12}(p, \gamma)$ radiation has been measured below 450 kev, and the cross sections of both reactions are extrapolated to stellar energies. The extrapolated cross section factor S_o at 25 kev C. M. proton energy is 6.0 ± 0.8 kev-barn for the $C^{13}(p, \gamma)$ reaction, and is 1.33 ± 0.13 kev-barn for the $C^{12}(p, \gamma)$ reaction. The equilibrium ratio by number of C^{12}/C^{13} in the CNO cycle is thus 4.1 ± 0.7 at a temperature of 15×10^6 ^oK.

The parameters of the resonance controlling the low energy cross section in the $C^{13}(p, \gamma)$ reaction are determined—a resonance energy of 555 kev and a reduced width of 570 kev. The experimental cross section is fitted with the Breit-Wigner single level formula and, for comparison, a fit based on the Humblet-Rosenfeld theory of nuclear reactions is attempted.

A new level was found in the $C^{13}(p, \gamma)$ reaction at a resonance energy of 448.5 ± 0.5 kev (7.966 Mev excitation) with a total width of less than 400 ev. Angular distribution measurements, combined with the results of $N^{14}(\alpha, \alpha')$ by other workers, lead to an assignment $J^{\pi} = 2^-$ for this resonance.

TABLE OF CONTENTS

I. INTRODUCTION

The reactions $C^{12}(p, \gamma)N^{13}$ and $C^{13}(p, \gamma)N^{14}$ are, in addition to their usefulness as reactions for studying the properties of light nuclei, of particular importance since they represent half of the four reactions comprising the main branch of the carbon-nitrogen cycle. In stars which are burning hydrogen through this cycle the equilibrium abundances of C^{12} and C^{13} will be inversely proportional to the low energy cross sections of these reactions. These reactions, then, provide laboratory measurements for comparison with the measured C^{12}/C^{13} abundance ratios in stars and hence serve as a test of the postulated models of stellar interiors.

The carbon-nitrogen cycle is expected to be in operation in the cores of main sequence stars and in the shells of giant stars. Temperatures typical of the cores of main sequence stars such as the sun are calculated to be 12 to 30 million degrees while those of giants are in the range 40 to 50 million degrees. On the basis of these calculations, those protons with center of mass energies of from 20 kev to 55 kev contribute most to the reaction rates. Obtaining cross sections at these energies, which are, of course, much too small to hope to measure directly, necessarily involves extrapolation procedures; these extrapolation procedures have already been used for the $C^{12}(p, \gamma)$ reaction (Thomas, 1952 and Burbidge et al., 1957). However, in the case of the $C^{13}(p, \gamma)$ reaction, the extrapolation depends critically on the assumed absence of levels in N^{14} in the stellar energy region. The proton threshold occurs at an excitation energy of 7.546 Mev in N^{14} (see Figure 1), at which energy the known levels have an average

spacing of a few hundred kev (Ajzenberg-Selove and Lauritsen, 1959). The energy levels of N^{14} have been investigated in this energy region by several workers. Seagrave (1951) has measured the excitation curve of the $C^{13}(p, \gamma)$ reaction from a proton bombarding energy of 400 kev to 2600 kev, while the nature of the gamma radiation at each of the five resonances found by Seagrave has been studied by Woodbury, Day, and Tollestrup (1953). Milne (1954) has studied the elastic scattering of protons from C^{13} in the energy region from 450 kev to 1600 kev, and has been able to assign spins and parities to the levels found by Seagrave. Christy (1956) has analyzed Milne's data for the 500 kev resonance, and concludes that better agreement with theory would be achieved if Milne's cross sections were reduced by approximately ten percent.

The energy levels of N^{14} have also been investigated by means of the reactions $C^{13}(d, n)$, $N^{14}(p, p')$, $N^{14}(\alpha, \alpha')$, and $N^{15}(He^3, \alpha)$. Neutron groups from the deuteron bombardment of C^{13} have been detected by Benenson (1953) who found, in addition to the well-known level at 8.06 Mev, evidence for levels at 7.72 ± 0.04 and 7.50 ± 0.04 and 7.00 ± 0.04 Mev, as well as other levels of lower excitation. Gamma rays of energies 7.05 ± 0.04 and 7.30 ± 0.05 Mev from the $C^{13}(d, n)$ reaction are attributed by Bent, Bonner and Sippel (1955) to levels in N^{14} at 7.02 and 7.40 Mev after a Doppler correction is applied.

Inelastic proton scattering from N^{14} gives levels at 7.03 ± 0.02, 7.40 ± 0.02, and 7.60 ± 0.02 Mev. In this experiment of Burge and Prowse (1956) levels above 7.60 Mev were not observed because of

the very short range of the resulting protons which were detected in nuclear emulsions. Alpha groups from the He^3 bombardment of N^{15} have been detected by Clayton (1962). The states observed in N^{14} were at energies of 8.06 Mev, 7.97 Mev and 7.032 ± 0.010 Mev as well as other states at lower energies. A careful search was made for levels in the 7.1 - 7.9 Mev region but none were found.

Inelastic scattering of 21.5 Mev alpha particles has lead to the identification of a level by Miller et al. (1956) at an excitation energy of 7.94 ± 0.07 Mev. A level is also detected at 7.02 ± 0.08 Mev, but there are no alpha-particle groups corresponding to the levels reported between 7.4 and 7.8 Mev. The alpha-particle group to the 8.06 Mev level is also absent. It is presumed that the isobaric spin selection rule is operative in the case of the absent alpha-particle group to the 8.06 Mev level.

Recent experimental investigations of inelastic proton scattering from N^{14} by Brown (1963) revealed levels in N^{14} at excitations of 7.96 Mev, 7.03 Mev, and others at lower energies. However, his data gave no evidence for any levels between 7.03 Mev and 7.96 Mev at any of seven observation angles, in disagreement with the results of Burge and Prowse (1956) for the same reaction. Brown's (1963) results appear more reliable, however, since he had available a higher beam energy than did Burge and Prowse (1956) and used a solid state detector rather than emulsions to detect the proton groups.

There is general agreement on the presence of a level in N^{14} at an excitation of 7.02 Mev. It is tempting to suggest that the level

identified by Benenson (1953) at 7.50 Mev is the same level as that identified by Bent et al. (1955) and by Burge and Prowse (1956) at 7.40 Mev and is thus below the proton threshold. Similarly the 7.72 Mev level of Benenson (1953) would be identified with the 7.60 Mev level of Burge and Prowse (1956). Such a level, above the proton threshold, would not be observed by Bent et al. (1955) if the proton width or cascade gamma-ray widths were much larger than the ground state gamma-ray width. However, on the basis of Clayton's (1962) and Brown's (1963) results, grave uncertainties are cast on the existence of any level in the region between 7.02 Mev and 7.96 Mev excitation in N^{14}. In fact, on the basis of these two experiments it would seem reasonable to conclude that no resonance is present in this region. Nonetheless, because of its importance in stellar reactions, it is necessary to examine the region with great care in search of a possible $C^{13}(p, \gamma)$ resonance before being certain none exists.

The level below the proton threshold, probably at 7.40 Mev if it exists, can contribute to the $C^{13}(p, \gamma)$ reaction only if the proton reduced width is large, in which case there is a nonresonant contribution to the cross section at higher proton energies. This nonresonant contribution will not be easily distinguishable from the other sources of the nonresonant capture cross section, and so will be included in the cross section extrapolated from the measurable region to stellar energies.

The question of the existence of the 7.60 Mev or 7.72 Mev level is particularly important to resolve from the point of view of the stellar $C^{13}(p, \gamma)$ reaction rate. If the level exists, and if its excitation energy

is sufficiently high to permit detection, the position and characteristics of this level may be studied directly by means of the $C^{13}(p, \gamma)$ reaction.

This thesis therefore reports (see Section III) absolute measurements of the $C^{13}(p, \gamma)$ cross section as a function of energy down to a proton bombarding energy of 92 kev (7.634 Mev excitation) in order to estimate the relative importance of the resonant and nonresonant contributions to the cross section. The same data provides upper limits for the widths of unobserved resonances in this reaction. A measurement of the $C^{12}(p, \gamma)$ cross section has been made with a thin target which was also used for the $C^{13}(p, \gamma)$ measurement in order to determine the $C^{12}(p, \gamma)$: $C^{13}(p, \gamma)$ cross section ratio as a function of energy. This is reported in Section IV.

Humblet and Rosenfeld (1961) have recently suggested that the well known Breit-Wigner single level resonance formula may not provide the best fit possible for resonance data. The $C^{12}(p, \gamma)$ reaction provides an exceptionally suitable test for the hypothesis since the first excited level at 2.362 Mev is 1.2 Mev distant from the next excited state; this state corresponds to a bombarding energy of 460 kev. The state in N^{14} at 8.06 Mev is not nearly so well isolated but still might provide a test of the hypothesis. A discussion of the Humblet-Rosenfeld single level formula appears in Section V along with a detailed comparison of this formula with the Breit-Wigner formula and attempted fits to experimental data from the $C^{12}(p, \gamma)$ and $C^{13}(p, \gamma)$ reactions.

The cross section measurements of the $C^{12}(p, \gamma)$ reaction were carried out with protons of energies up to 680 kev and is reported on in Section IV. Section III contains the results of the $C^{13}(p, \gamma)$ measurements which were made up to the same proton energy.

A report is also made on the gamma-ray yields and angular distribution from a $C^{13}(p, \gamma)$ resonance at a proton energy of 448.5 kev, found during the course of this work. This resonance, at an excitation energy of 7.966 Mev, probably corresponds to the 7.94 Mev level found by Miller et al. (1956) and the 7.97 Mev level observed by Clayton (1962). Since this level is extremely narrow and of small yield it can be disregarded in the low energy cross section extrapolations. The discussion of this level will thus be treated independently of the main body of this thesis, in Part VII.

II. APPARATUS AND EXPERIMENTAL DETAILS

A. Preparation of Targets

All of the many targets used in this experiment, with one exception, were made in the same way. The backing used for the targets was 0.020 inch thick sheet tantalum, carefully polished with successively finer grades of emery paper, finishing with polishing alumina. The polished sheet was then cleaned with soap and water after which the target blanks were punched out. These blanks were placed into the glass target making apparatus shown in Figure 2. After pumping the system down below 10^{-5}mm the blank was outgassed by heating to incandescence with an induction heater. One branch of the apparatus contained one gram of iodomethane (methyl iodide, CH_3I) which freezes to a solid with vapor pressure less than 10^{-6}mm at liquid nitrogen temperatures. After freezing the methyl iodide all the valves were opened and the system pumped down below 10^{-5}mm again. The valve connecting the apparatus to the pumping system was closed and the methyl iodide was slowly melted. When the vapor pressure reached 10 mm, as measured on the manometer, the valve connecting the methyl iodide to the system was closed. The blank was again heated, causing the methyl iodide vapor to crack, leaving a thin film of carbon on the tantalum blank to serve as a suitable target. Methyl iodide is particularly well suited for target making because iodine vapor is released when this material is cracked. By observing the amount of iodine released, it is possible to estimate the amount of carbon deposited on the blank. The ultimate thickness of this deposited layer was a function of (1) the vapor pressure of the methyl iodide, (2) the length of heating time, and (3) the temperature to which the blank was heated.

It was found that the carbon layer adhered better to the tantalum if the outgassed blank was permitted to cool at atmospheric pressure after outgassing in a vacuum. This was accomplished by heating the blank with the induction heater to a yellow heat and then while turning off the heater simultaneously opening the system to the atmosphere.

This treatment of the backing was found to have no measurable effect on the background at any of the bombarding energies used in the experiment, although the appearance of the tantalum blank was greatly changed; that is, where the blank had been shiny and silver before it was now dull and grey. The treatment did, however, have beneficial effects on the targets since the carbon layer seemed to adhere better to the backing and, as will be mentioned later, the target had a longer lifetime under beam bombardment.

Chemically pure methyl iodide, which contains 1.1 percent C^{13} and 98.9 percent C^{12} was used in making the targets for the $C^{12}(p, \gamma)$ measurements. For measurements of the $C^{13}(p, \gamma)$ reaction methyl iodide enriched in C^{13} was used. The first supply was obtained from Eastman Kodak Corporation who quoted an enrichment of 61 percent. The enrichment does not change when the targets are made as has been shown by elastic scattering experiments (Hebbard and Vogl, 1960). Unfortunately, this original methyl iodide supply was depleted and no more was obtainable from Eastman. One gram of the material was then obtained from Merck and Company Ltd. who reported it to be enriched to 54.0 percent C^{13}.

B. Target Chamber and Gamma Ray Detector

Two separate, but quite similar, target chambers were used for this experiment. The first type was designed specifically for the measurement of gamma ray angular distributions and its use for this will be described in Part VII. In addition, however, it proved to be entirely adequate for all the cross section measurements between 200 kev and 700 kev proton bombarding energies.

This target chamber, shown in Figure 3, was constructed from pyrex tubing with a base and a lid of aluminum. The target was supported by a stainless steel rod which passed through the aluminum base. A second rod, passing through the base, supported a quartz disc which was used to observe and shape the proton beam and position the target.

The proton beam was analyzed electrostatically. The calibration of the analyzer and the energy resolution of the beam were determined by obtaining profiles of the 448 kev resonance in the $C^{13}(p, \gamma)$ reaction. These determinations are described in detail in Section III-C. The beam current was integrated with a standard laboratory integrator by charging a capacitor. The integrator was calibrated by measuring the time required to charge the capacitor with a known current.

A 4 inch by 4 inch NaI(Tl) crystal mounted on a Dumont 6364 photomultiplier tube was used to detect the gamma radiation for most of the experiment, although a similar crystal mounted on an RCA 7046 photomultiplier tube was used for the measurements above 450 kev proton bombarding energy. The crystal was placed 3.8 cm from the target for yield measurements between 303 kev and 440 kev proton energy. Below this energy, the detector was moved to within 1.9 cm

of the target by moving the target from the central rod to the rod supporting the quartz disc. This change was made to increase the measured yield, and, in fact, allowed yield measurements to be carried out down to 160 kev proton energy with reasonable accuracy. Below this energy, because of the rapidly decreasing cross section, it was not possible to obtain useful results. Although the maximum beam current from the Van de Graaff generator was monotonically decreasing with beam energy, the primary reason for the loss of accuracy below 160 kev was the large amount of background radiation detected by the 4 inch by 4 inch crystal.

This background consisted of two parts—that due to natural radioactive sources and that due to cosmic ray interactions. There are no known natural radioactive sources producing gamma rays with an energy greater than the 2.62 Mev gammas from ThC". Hence, the background present in the vicinity of the 8 Mev gamma peak from the $C^{13}(p, \gamma)$ reaction was assumed to arise from cosmic rays. Since cosmic rays consist primarily of charged particles, it is believed that they contributed by far the largest component to this background, the remainder resulting from neutral particles and gamma rays that interact with the crystal. Based on this assumption, a charged particle anticoincidence shield was designed and constructed in an attempt to carry the cross section measurements to still lower energies.

C. The Anticoincidence Shield

The central component of this shield was the plastic scintillator shown in Figure 4, which was obtained, completely finished, from Nuclear Enterprises, Ltd. A hole 7/8 inch in diameter was provided in the front of the plastic scintillator, so that a target could be located inside the shield as close as possible to the sodium iodide crystal.

(The target and target chamber are shown schematically in Figure 3.) The wall thickness of this scintillator, 3.2 cm., insures an energy loss of at least 7 Mev for minimum ionizing particles. With this loss a light collection efficiency of only 0.2 percent will give a signal to noise ratio greater than 5 to 1. A 2 inch Dumont 6292 photomultiplier tube was used to detect this radiation loss. This phototube was light coupled to scintillator through a lucite cylinder 1/2 inch long and 1 1/2 inches in diameter cemented to the flat front surface of the scintillator.

The NaI(Tl) crystal could not be easily shielded from particles incident from the backward direction but this was not of great importance. The total solid angle available for these particles with the geometry chosen was 15 percent of 4π steradians. This figure, however, is based on the assumption of an isotropic distribution of cosmic ray secondaries. The distribution is actually strongly peaked in the vertical direction and follows closely a $\cos^2 \theta$ law where θ is the angle measured from the local zenith (Greisen, 1943). This distribution reduces the effective solid angle to 5 percent of 4π. A second important effect which has been neglected will reduce the effective solid angle still further. Only a small fraction of those particles that miss the anticoincidence shield but hit the sodium iodide crystal contribute to the background, since those particles must lose only 8 Mev in the crystal. Moreover, most of these particles that lose 8 Mev will pass through the crystal and into the plastic shield to be detected there, thus producing an anticoincidence pulse. In the effect, then, only those charged particles with energies close to 8 Mev will contribute to the background with the shield in place. This results in a further reduction in background since, without a shield in

place, no limits can be placed on the incident energy of those particles that lose 8 Mev in the crystal.

A brass container with an inside diameter large enough to accommodate the 4 inch by 4 inch crystal and mount was fabricated to enclose the scintillator (Figure 5). A brass tube fitted with an "O" ring to give a light tight seal was used to hold the 2 inch photomultiplier tube in place. Before placing the scintillator in its enclosure it was completely covered, except for the face of the light pipe, with aluminum foil in order to improve the light collection efficiency. Sheet foam rubber was used as shown in Figure 5 to keep the scintillator firmly in place in its container. The phototube was held firmly against the light pipe by means of three set screws located in the brass cylinder.

The anticoincidence circuit designed for use with this shield was not required to be of very sophisticated design for two reasons. First the counting rates were very low (always less than 100 cts/sec) so that several microsecond dead times could be used, and, second, linear circuitry was not required since the 100 channel analyzer was provided with a coincidence input that acted as a linear gate. To use this coincidence input a circuit with the following characteristics was designed:

1) With both NaI(Tl) and plastic scintillator inputs, no output

2) With only a NaI(Tl) input, a negative output of magnitude greater than 11 volts.

3) With only a plastic scintillator input, no output.

Another simplification in circuit design was achieved by using the delayed coincidence input on the 100 channel analyzer. If the prompt coincidence input has been used, the analyzer input signal would have

had to have been delayed by a time at least as long as the transit time of the pulse passing through the anticoincidence circuit. On the other hand, the use of the delayed coincidence required stretching the anticoincidence output pulse beyond 4 microseconds. This time represents the difference between the prompt and delayed coincidence signal that is required to store a pulse in the analyzer. Since the count rate was very low, the anticoincidence output pulse was widened to 10 microseconds to make certain all the real pulses would be counted.

The circuit designed with these properties is shown schematically in Figure 6. The core of this circuit is the 6BN6, a pentode with two control grids. A negative signal greater than 2 volts on either of these grids cuts off the tube. Three diodes in series were connected between the NaI(Tl) input and ground to limit this input pulse height to 0.5 volts. This clamp prevented the small conduction that would occur in the 6BN6 if a very large NaI(Tl) pulse was impressed on one grid even though a plastic scintillator pulse was in coincidence with it. Limiting the input pulse height to 0.5 volts had the further advantage of producing an output pulse of constant amplitude.

Using this circuit many background runs were made to determine the effectiveness of the plastic scintillator shield. The first of these runs was made with the gain in the plastic scintillator circuit as the parameter. (Both the phototube voltage and the amplifier gain were varied.) As the gain was increased the background intensity decreased monotonically until reaching a limit. Further gain increases did not affect the background. This result was quite encouraging since it indicated that virtually all of the light pulses produced in the plastic scintillator were activating

the anticoincidence circuit, and that no further effort to increase the light collection efficiency was necessary.

The next background runs, performed to determine the effectiveness of lead shielding, established that placing 4 inch of lead above the scintillator yielded a further background reduction. To take advantage of this effect, a lead shield which, except for the back face, completely enclosed the scintillator, was cast and machined. This shield consisted of, first, a flat circular plate 2 inches thick for the front, and second, 180° sections of a cylindrical shell for the top and bottom. The bottom shells were 1.5 inches thick, the top, 2.5 inches thick.

In Figure 7 a comparison of the background spectra for four different conditions is shown. The 8 Mev gamma ray peak is drawn on the figure for reference. The significant results of these comparison runs were as follows:

Type of Run	Counts/sec
no anticoincidence, no lead	7.55
anticoincidence, no lead	2.95
no anticoincidence, lead	5.41
anticoincidence, lead	1.18

The "count/sec" column gives the total number of counts over the channels in which the 8 Mev gamma ray peak occurs, i.e., the region included between the two vertical arrows in Figure 7. The reduction in background effected by the anticoincidence counter and the lead shield was thus a factor of 6.5, i.e., 85 percent of the background originally present had been eliminated. Moreover, it is interesting to note that this reduction

factor approaches 20 at the spectrum point corresponding to 10 Mev gamma rays. This latter observation leads to the probable conclusion that a large fraction of the background below 10 Mev is caused by (n, γ) reactions in the crystal. This energy region is reasonable since the Q-value for neutron capture in iodine is 8 Mev.

The investigations of V. Tongiorgi (1949) provide further clarification of this point. His experiments, performed at an altitude of 260m above sea level and thus quite applicable to this experiment, indicate some of the problems encountered when attempting to shield a counter from cosmic radiations. Tongiorgi (1949) made a series of measurements with a neutron counter shielded by both lead and paraffin. First, he found that a 5 cm thick lead shield increased the neutron count rate by a factor of 2.4 over the normal cosmic ray rate. Second, he found that removing the lead and placing 25 cm of paraffin around his counters led to a 56 percent decrease below the normal cosmic ray background rate. This reduced rate increased but by only 20 percent when 7.5 cm of lead was placed around the paraffin.

These results indicate that a background radiation is present which is not absorbed in lead and is capable of producing neutrons in lead, the great majority of which are stopped in 25 cm of paraffin. It thus seems probable that, for the experimental arrangement used here, the lead shield placed around the anticoincidence counter, while decreasing the overall background by absorbing the gamma ray component most strongly, increased the neutron background thus leading to a larger number of (n, γ) reactions in the crystal. This supposition could help to explain the peaks that appear near channel 60 in the background spectrum shown in Figure 8. From Tongiorgi's (1949) results, we would expect that

covering the anticoincidence counter with 25 cm of paraffin and then enclosing this with a 7.5 cm lead shield would have further reduced the background. However, such a shield would have required very large quantities of paraffin and of lead, and was thus not very seriously considered.

The pyrex target chamber used in conjunction with the anticoincidence shield is shown in Figure 9. To allow the same base, top, and vacuum connections to be used with both this target chamber and the one previously described, the main body of both were constructed with identical dimensions. The added tube on this new chamber was small enough to fit through the hole in the front surface of the plastic scintillator, thus permitting a target location close to the NaI(Tl) crystal. Enlarged detail drawings are included in Figure 9 which show the method used to position the target in this tube and collect the charge from the target. The phosphor bronze spring clip kept the target firmly in place and provided a positive electrical contact with the target. Since large beam currents were used in the experiment, a copper heat radiator was attached to the aluminum cap at the end of the target chamber tube to prevent overheating of the "O" ring seal. Charge leakage, which would have occurred if the copper radiator touched any of the surrounding conductors, was eliminated by inserting a quartz disc between the target and the aluminum cap.

Since the target was not visible when using the anticoincidence shield, the target chamber had to be aligned before the shield was in place. When the alignment was satisfactory, i.e., when the beam hit the center of the target, the position of the beam was noted on a piece of quartz on the target rod in the main section of the target chamber. (Cross hairs on the quartz

and a line scribed on the target rod marked this position.) Thus, after the anticoincidence shield was in place, the beam was aligned on the target by performing observations in the main chamber. The accuracy of this procedure was demonstrated when targets were removed after use. In every instance, these targets exhibited a beam spot completely contained within the target and very close to the target center. Thus, it was certain the beam had not hit the target chamber walls causing erroneous charge integrations.

A preliminary proton run at 450 kev using the anticoincidence shield indicated that no correction to the 8 Mev gamma spectrum between 5 and 8 Mev would be required from anticoincidences produced in the shield. This result was surprising since secondary electrons and photons escaping from the NaI(Tl) crystal were expected to produce pulses in the plastic. Closer examination, however, showed that the experimental result should not have been a surprise. First, the energy of each electron from the pair production interaction is less than 3.5 Mev. The range of such an electron is $2 g/cm^2$, a distance of only 5.5 mm in sodium iodide and 2.4 mm in brass. This latter figure is less than the wall thickness of the brass can. Thus, none of the energetic electrons produced in the crystal could reach the plastic scintillator to give an anticoincidence blanking pulse. Second, the angular distribution of the Compton scattered photons is strongly peaked in the forward direction (the differential cross section at 45° is 1/12 of that at 0°) and those photons that pass normally through the anticoincidence shield have a 0.07 absorption probability. The actual spectrum of energy loss in the plastic for a given interaction in the crystal is too complex to attempt to calculate, but its relative

magnitude should be quite small. The experimental result mentioned above is thus not in contradiction with qualitative theoretical predictions.

D. Experimental Modifications for the Low Energy Region

The first data run using the anticoincidence shield included proton bombarding energies down to 130 kev. It became immediately apparent that the minimum energy at which useful data could be obtained was limited not by the cosmic ray background but by an insufficient beam current. At low energies the beam intensity dropped quite sharply with decreasing beam energy; this sharp fall off coupled with the rapidly decreasing reaction cross section indicated that experimental data could probably not be obtained below 120 kev.

Of the possible techniques useful for increasing the low energy beam current, utilization of the mass-two beam of H_2^+ ions was thought to offer the most promising solution. A mass-two beam of energy E and current I is equivalent (except for the small binding energy of the H_2^+ ion) to a mass-one beam of energy E/2 and current 2I. Since the van de Graaff electrostatic generator produces larger currents at higher energies, it is easily seen that the utilization of a mass-two beam increases the effective beam current at a given proton energy in two distinct ways.

Using the mass-two beam a proton current of 65 μa was obtained at a net bombarding energy of 92 kev, while the current obtainable at this energy with a mass one beam was less than 1 μa. Though the yields at this energy are small ($\backsim 10^{-19}$), these large beam currents, coupled with the reduction in background, permitted useful data to be taken. However, two problems of considerable importance did arise.

The first of these problems concerned the targets themselves. The targets used for the first runs were deposited on blanks that had not been subjected to all the preparations described in Section II, A above. In particular, they had not been cooled with air from a red heat after the outgassing was completed. This had no observable effect on the targets (as determined by the constant yield at a given bombarding energy) until a large quantity of charge (1/2 coulomb) had been deposited in the target backing. As the deposited charge was further increased the gamma ray yield at the low proton bombarding energies began decreasing, slowly at first and then quite rapidly, although the yield at 450 kev remained unchanged. No completely adequate explanation was found for this behavior although the dilution of the thin carbon target by the diffusion of the relatively large quantity of hydrogen in the backing furnished a possible solution. This dilution of the target material would tend to decrease the yield more effectively at low energies than at high since, at low energies, the differential gamma yield as a function of target depth decreases very rapidly with increasing depth, while at 450 kev this decrease with depth is much less pronounced.

Following the discovery of the above effect, all future targets were fabricated by depositing the carbon layer on blanks that had been cooled in air after outgassing. Adding this extra step led to the apparent disappearance of the dilution effect; the explanation of this further change is not understood. To obviate any possibility of utilizing erroneous experimental results caused by this dilution, no data was considered that had been obtained from targets following the deposition of 0.5 coulombs of charge. In addition, the yield was plotted as a function of the deposited

charge before the 0.5 coulombs had been deposited in order to make certain no systematic changes were occurring.

The second of these problems was with the background. In particular, a beam dependent background appeared as an unmistakable gamma ray peak in the 100 channel analyzer display at an energy of 5 Mev. The peak was initially assumed to be due to the well known gamma ray from the F^{19} (p, $\alpha\gamma$) reaction. A CaF_2 target had been used in the target chamber for calibration purposes and it was believed that some of the CaF_2 had contaminated the vacuum system. After many attempts to clean the system were unsuccessful, data was taken with the contaminant peak present in the spectrum. Since this peak was below the energy range of importance in the C^{13} (p, γ) reaction (6 to 8 Mev) the data obtained in this way was expected to be satisfactory. After all the low energy data had been taken, a target bombardment with a deuteron beam was made to check the possible background increase from the small percentage of D^+ ions that were inevitably present in any H_2^+ beam. (The mass difference between H_2^+ and D^+ was too slight to permit separation in either the magnetic cross field or the electrostatic analyzer.) This run yielded an unexpected and somewhat embarrassing spectrum. The same "fluorine" gamma peak appeared but with a greatly increased intensity, and, in addition, a high energy tail not related to the peak appeared in the spectrum. The peak itself was presumably caused by gamma rays from the C^{13} (d, α) reaction in the target. The high energy tail was extremely critical because it extended into the important region of the C^{13} (p, γ) spectrum. Although it was possible to correct for this additional background, data taken without it would have been more desirable. This improved data

had to be obtained with a mass-one beam, which implied, of course, greatly increasing the maximum attainable beam current at low proton energies. To reach this goal, several design improvements in the beam controlling system had to be made.

First, the electronic circuitry controlling the cross field current was completely redesigned. Adjustable cross field slits, previously absent, were installed just before the main target chamber, and the electrostatic analyzer slits were rebuilt; with these modifications the positions and the separations of both sets of slits could be accurately controlled and measured. The RF ion source bottle and canal were replaced, the electrostatic analyzer plates cleaned and the analyzer painstakingly aligned for maximum beam current at a 300 kev proton energy. Following these extensive preparations, it was possible to attain a maximum beam current of 45 μa at a proton energy of 240 kev. At 170 kev, the maximum current dropped to 32 μa. Three of the ten column resistors in the electrostatic generator were then shorted out in an attempt to increase this beam current to 45μa. The reasons for expecting this increase were as follows:

> The beam tube in a van de Graaff electrostatic generator provides weak focussing, most of which occurs when the beam is moving slowly. As the beam accelerates down the column each succeeding gap focusses less efficiently than the one before. Thus, shorting out the last three accelerating gaps should have a small effect on the focussing properties of the entire column. However, to obtain the same beam energy from the generator, the gradient across each remaining gap must be increased. Thus, shorting out three

of ten gaps required the gradient to be increased in the remaining ones by a factor of 10/7 = 1.43. Under these conditions, a beam of energy 170 kev passes through accelerating gaps whose gradients are normally those associated with a machine energy of 240 kev. One would thus expect the machine to operate as if the beam energy were really 240 kev, except for a somewhat smaller maximum beam current since the focussing of the last three gaps, though small, is no longer present.

In actual application, however, the above theory did not fit the experimental observations. In fact, the beam current at 170 kev dropped to 28 μa from the previous 32 μa. This loss in current reflected the loss in focussing resulting from the shorting of the last three gaps, as had been expected. The anticipated increase in current failed to materialize. Since there was now no hope of obtaining a mass-one beam of sufficient intensity at low proton energies, the effort to obtain accurate mass-one data to replace the already obtained mass-two data below 120 kev was terminated.

The energy range from 400 kev to 680 kev for both the $C^{12}(p, \gamma)$ and $C^{13}(p, \gamma)$ reactions was then examined using the original Pyrex target chamber without the anticoincidence shield.

III. THE $C^{13}(p, \gamma)$ REACTION

This reaction was experimentally observed with protons whose bombarding energies were varied from 92 kev up to 680 kev. Over this energy range the yield data was taken in three distinct sections, the first covering the range from 445 kev down to 160 kev, the second the range below 200 kev, and the third, the range above 400 kev.

The energy range was divided into these regions because of the wide variations in yield that occurred. The first region covered an energy range in which no resonances were present and in which the background was small. In the second region, the yield was small and thus the anti-coincidence shield described in Section II-C was used. The third region was dominated by the resonance at 554 kev and was examined in finer detail than either of the other two regions so that the resonance parameters could be determined accurately.

A. Gain Change Corrections

In all cases, the pulse height data was stored in a 100 channel analyzer, printed out, and plotted graphically. This last step was necessary for checking the spectrum shape and determining what, if any, gain change had occurred. The background spectrum shown in Figure 8 indicates why an accurate gain change determination was important. For the position of the gamma peak shown in the figure (the region between the vertical arrows) the difference between the background rate at the two arrows was (0.08 - 0.02) = 0.06 counts/minute channel. For a 600 minute run at 92 kev, 195 ± 69 real counts were obtained. A one channel error in the position of the gamma peak would change the background correction by 0.06 x 600 = 36 counts, more than half the statistical error in the yield.

By comparing the positions of gamma ray peaks in the spectra it was possible to determine accurately the magnitude of the change that occurred from run to run. However, the data obtained at very low proton energies was more difficult to correct for these changes. At 103 kev and 92 kev the reaction yield was so small that no recognizable peak was observed in the spectrum. (Several gamma spectra are shown in Figure 10 for reference.) Thus, for these energies, complete reliance for determining the gain change was necessarily placed on the position of background peaks in the spectra. Moreover, the only peak that could be utilized, that from the 2.62 Mev gamma of ThC", rose to only 1/3 the magnitude of the reaction gamma ray. Thus, the error in determining the position of the latter would be three times as great as any error in the former. In addition to a gain change, there also existed a small uniform spectrum shift of one channel or less, presumably caused by bias level changes in the 100 channel analyzer which was found by feeding the output from a pulser into the analyzer. Of course, measuring the shift in only one point, the thorium peak, was not sufficient to determine the relative importance of these two causes for shifting the position of the reaction gamma ray peak. However, there were several independent runs at 92 kev and at 103 kev (8 and 5 runs respectively) and each of these runs was over 60 minutes long, so that, on the average, the effect of random gain changes and bias level changes could be expected to be small. To test this expectation, the background subtractions at these energies were made in three ways. First, it was assumed that no changes in gain or bias level had occurred. Second, the change in the position of the thorium peak was assumed to be caused entirely by a bias level change. Third, this change in position was

assumed to result entirely from a gain change. The yields obtained by using these three were essentially identical and the variation among them was less than one standard deviation. However, the variation in yield from run to run for the data analyzed by the third technique was much larger and not within the statistical variation expected. The use of techniques one and two led to internally consistent yields. It was thus felt that, at least at 92 kev and 103 kev, the entire change in position of the thorium peak, and of the full energy reaction gamma ray peak as well, resulted from a change in bias level. Since these changes in position were small—less than 1/2 channel in almost all cases—and random in direction, this assumption should not have led to systematic errors. (The gain change that normally occurs from counting rate variations was no problem at these energies since the background rate was considerably greater than the real rate.)

B. Corrections for the Deuteron Background

As mentioned above, the use of a mass-two beam introduced a beam dependent background caused by the deuteron component in the beam. The gamma ray spectrum obtained by bombarding a C^{13} enriched target with a 400 kev deuteron beam is shown in Figure 11. The existence of the high energy tail extending to channel 82 should be noted, in addition to the prominent peak at channel 46. A gamma spectrum for 200 kev bombardment of the same target with the mass-two beam is presented in Figure 12. A comparison of Figure 12 with Figure 28 dramatically displays the spectrum changes caused by the deuterons in the beam; the high energy tail has both changed the shape of the full energy peak and increased the relative amplitude of the compton tail. The corrections for this additional

background were calculated by determining the shape of this high energy background tail. This tail can be fitted, within experimental error, by a straight line, with an energy intercept of 8.2 Mev, i.e., a function of the form:

$$G(E) = m(8.2 - E) \tag{3.1}$$

in which G is the background as a function of energy, and m is an empirically determined constant. (This form for the tail simplified the correction calculation somewhat, but was not of any fundamental importance.) The method used to extract this background from the data can be most easily described by reference to the schematic spectrum drawn in Figure 13 which represents the yield after the time dependent background subtractions have been made. (In Appendix A, the calculation of the gamma yield from the 200 kev proton bombardment is carried out in detail.) The composite gamma ray spectrum has been divided into two regions, the first from 5.4 Mev to 6.5 Mev, and the second from 6.5 to 8.7 Mev. In each of these regions, gamma rays from both the proton and deuteron reactions are present. There are thus four distinct yields labeled A, B, C, and D in Figure 13. The reaction yield desired is the sum B + D. As there are four known and independent quantities, each of the four yields, and thus the sum B + D, can be determined. The straight line function, equation 3.1, gives the ratio $A/C \equiv \alpha$. The ratio $B/D \equiv \beta$ can be obtained from Figure 28. The third and fourth relations are obtained directly from each spectrum. These are simply the sums $A + B \equiv x$ and $C + D \equiv y$, the total counts in each region. Combining these four relations and solving for B + D, one obtains:

$$B + D = \frac{1 + \beta}{\alpha - \beta} (\alpha y - x) \tag{3.2}$$

The variables α and β take on different values at each proton bombarding energy. This is caused by a slight shift in the position of the ground state gamma ray as the proton energy is varied. Although the shift in this position of the peak is small (the Q value for the $C^{13}(p, \gamma)$ reaction is 7.546 Mev) this effect was considered in the data analysis. In all cases, however, the change in yield caused by the change in gamma ray energy was much less than the statistical error. The value of α varied from 0.591 to 0.624; β was experimentally determined as 0.1602 ± 0.0016.

The quantities x and y were obtained from the gamma ray spectra by subtracting the time dependent background after the gain change corrections had been completed.

The error in the quantity B + D is given by

$$\Delta(B + D) = \frac{1 + \beta}{\alpha - \beta} \left[(\alpha \Delta y)^2 + (\Delta x)^2\right]^{1/2} \tag{3.3}$$

in which the errors in α and β are neglected being small compared to the errors, Δy and Δx, in y and x.

The values of Δy and Δx are given by:

$$\Delta y = \sqrt{(B + A) + b_y + \frac{t}{\tau} b_y}$$

$$\Delta x = \sqrt{(C + D) + b_x + \frac{t}{\tau} b_x} \tag{3.4}$$

where

t = time of run

τ = time of background run

b_x = time dep. background in the C + D region

b_y = time dep. background in the A + B region.

The error $\Delta(B + D)$ in each point was greatly increased by the presence of the deuteron induced background. At the lowest bombarding energy attained, 92.4 kev, this background increased the percentage error by a factor of 1.8.

The full energy capture gamma ray in the composite of all gamma ray spectra taken at either 92.4 kev or at 103 kev could not be visually detected. The composite gamma ray spectrum from the 92.4 kev bombardment is shown in Figure 14, and should be compared with the background spectrum of Figure 8 to demonstrate the similarity between the two. This similarity is not surprising since the time dependent background was 6 times greater than the reaction yield at 92.4 kev and 5 times greater at 103 kev.

A consistency check was made on the reaction yields obtained in these two cases. This check was performed by utilizing two independent techniques. First, the raw yields of all the runs at each beam bombarding energy were divided into two energy regions, the first from 6.5 to 7.5 Mev, and the second from 7.5 to 8.7 Mev. After both the time dependent and the beam dependent background were subtracted independently, the ratio of the two net yields was obtained. This ratio was compared with one measured with a mass-one beam at high energy where the background was negligible. The difference between these ratios was well within the statistical errors. Second, the total number of runs at each proton bombarding energy was arbitrarily divided into two groups and the yields from each group analyzed independently. Once again, the yields were consistent with the statistical errors. These checks lent confidence to both the method used for correcting the beam dependent background and to the gain change determinations on which the time dependent background correction were based. As a point of interest, the net experimental yield at 92.4 kev was 117 ± 42 counts

per coulomb of protons. In all, 1.72 coulombs of protons were used to measure the cross section at this energy. Other runs were made at this energy (totaling over 1 coulomb of charge) which were not included in this analysis because the targets had already become "worn out" (see page 19 of this thesis) and could not be utilized.

C. Target Thickness and Energy Calibration

Many targets were used in the experiment. The thickness of these targets could not be kept constant because slight variations in the target preparation parameters were unavoidable. It was thus necessary to determine independently the thickness of every target used. The newly found $C^{13}(p, \gamma)$ resonance at 448 kev, discussed in detail in Section VII, provided a simple and straightforward means for measuring this thickness, as described below.

In Figure 15 two excitation functions taken in the vicinity of this resonance are shown. A discriminator biased out all gamma rays of energy less than 5 Mev; these figures are thus primarily excitation functions of the ground state radiation. Once the energy of this new resonance was accurately determined (described in Part VII of this thesis) every excitation function taken provided a calibration of the electrostatic analyzer. Since the total width of the 448 kev resonance had already been fixed at less than 300 ev (Part VII), the excitation function also provided a measurement of beam resolution. The excitation function shown in Figure 15a is of a target 3.17 ± 0.30 kev thick, measured at a proton bombarding energy of 448 kev. The beam width was 870 ± 100 ev; the increased width in the back edge of the excitation function was caused by proton straggling in the target. Although the straggling changes the

shape of the excitation function, the position of the mid points of the rising and falling edges in the profile is unchanged to first order, because the straggling, again to first order, occurs symmetrically about the mean energy for the small energy losses occurring here (Gove, 1959).

Targets grouped into three different thicknesses were used in different regions of bombarding energies. Below 400 kev, where the gamma yield was relatively small and the cross section changed slowly with energy, the targets used were 8 to 12 kev thick. In the immediate vicinity of the 554 kev resonance (510 through 590 kev) where the yield was large and the cross section changed rapidly with energy, the target thickness varied between 2.5 and 3.0 kev. In the other regions which were intermediate between these two (400-510 kev and 590-680 kev) the targets were 5 to 6 kev thick.

D. Obtaining Cross Sections from the Gamma Ray Yield

Since the targets used in this experiment were never either "thick" or "thin," it was not possible to use any of the usual approximate formulas for reducing yield measurements to cross sections. Thus more accurate procedures had to be used. The exact expression (neglecting straggling) for the yield from a target of any thickness is given by

$$Y = \int_{E_2}^{E_1} \frac{\sigma}{\epsilon} dE \qquad (3.5)$$

where E_1 is the particle (proton) bombarding energy, E_2 the particle energy at the back surface of the target, E the laboratory proton energy, and ϵ the stopping cross section. In this experiment, however, the cross section, σ, is unknown and the yield, Y, has been experimentally determined. In order to use this formula, a trial value for the cross section

must be assumed and the integral numerically evaluated. The yield obtained is then compared with the experimental yield and the trial cross section varied until the two results are in agreement.

Since the reaction cross section was believed to be primarily determined by the 554 kev resonance, the trial function used was a single level Breit-Wigner resonance formula as follows:

$$\sigma = \pi \lambda^2 \frac{\omega \Gamma_p \Gamma_\gamma}{(E - E_\lambda - \Delta_\lambda)^2 + \frac{\Gamma}{4}^2} \tag{3.6}$$

in which the level shift, Δ_λ, given by $\Delta_\lambda = -S\gamma^2$ where $S = (FF' + GG')/(F^2 + G^2)$ and γ^2 is the reduced width of the level, was defined so that $E - E_\lambda - \Delta_\lambda = 0$ at the resonant energy, E_R. The widths Γ_p and Γ_γ contain, respectively, the energy variations of the penetration factor and of the gamma ray energy. The total width, Γ, can be correlated with the laboratory width, Γ_{lab}, by approximating the level shift, Δ_λ, with a linear energy dependent term only, i.e., $\Delta_\lambda = c(E - E_R)\gamma^2$, where c is a constant that can be determined from the slope of -S at $E = E_R$ (see Figure 19). Substituting into equation 3.6 gives:

$$\Gamma_{lab} = \frac{\Gamma}{1 - c\gamma^2} \cdot \tag{3.7}$$

To obtain the proton reduced width from the measured laboratory width we note that:

$$\Gamma_p = \frac{2kR}{A^2} \gamma_p^2 \tag{3.8}$$

and, since $\Gamma_\gamma << \Gamma_p$,

$$\Gamma_{lab} = \frac{2kR/A^2}{1 - c\gamma_p^2}\ \gamma_p^2 \tag{3.9}$$

which gives:

$$\gamma^2 = \frac{\Gamma_{lab}}{2kR/A^2 + c\Gamma_{lab}} \tag{3.10}$$

in which k is the proton wave number, R the interaction radius and $A^2 = F^2 + G^2$, the sum of the squares of the regular and irregular coulomb wave functions.

For protons at 555 kev lab energy incident on carbon 13, c = 0.750 Mev^{-1}, obtained from Figure 19, and, for s-waves $2kR/A^2 = 0.0957$. The calculation of the penetration factor was based on the use of published tables and a computer program and is described in Appendix B. The value of R used in the calculations, which were quite insensitive to the value of R actually chosen, was obtained from

$$R = 1.44\ (A_o^{1/3} + A_1^{1/3})\ \text{fermis} \tag{3.11}$$

or, for this reaction, R = 4.68 fermis.

In order to use a computer to calculate the gamma ray yield, sixth order polynomials of powers of the energy were fitted to the stopping cross section ϵ, the level shift parameter S, and the penetration factor $2kR/A^2$. This last factor varied too rapidly with energy to allow an accurate polynomial fit. However, by first factoring out a term of the form $\exp(-2\pi\eta)$ (see Appendix B for a definition of η) the remaining

variation with energy is slowly varying and can easily be fitted with a polynomial in E. Thus the computer actually calculated the product of two terms for the penetration factor, i.e.,

$$\left(\frac{2kR}{A^2}\, e^{2\pi\eta}\right) \times \left(e^{-2\pi\eta}\right)$$

The ground state radiative width, Γ_γ, was calculated by using a transition probability proportional to the cube of the gamma ray energy (dipole radiation), i.e.,

$$\Gamma_\gamma = \frac{(7.546 + 13E/14)^3}{(7.546)^3}\,\theta$$

where the constant θ was chosen to make $\omega\Gamma_\gamma = 10.1$ ev at E = 555 kev in agreement with the measurement of Seagrave (1951).

In order to fix the limits of integration in equation 3.5 the proton bombarding energy and the target thickness had to be known. The former was easily given. The latter presented a problem as the target thickness, in energy units, changes with the bombarding energy. Since the number of atoms/cm^2, N, in a target clearly is a constant independent of energy, this number was calculated for each target by integrating

$$N = \int_{E_2}^{E_1} \frac{dE}{\epsilon} \,. \qquad (3.12)$$

In all cases in this experiment E_2 = 448.5 kev and E_1 = 448.5 kev + ΔE, where ΔE was the experimentally determined target width at the 448 kev resonance discussed in Section III-C. Once N has been determined for a target the thickness in energy units for any bombarding energy E_1 can

be obtained by carrying out the above integral with the lower limit of integration as the unknown. If we define N(w) as

$$N(w) = \int_{w}^{E_1} \frac{dE}{\epsilon}$$

then, by decreasing w, a comparison of N(w) with N can be made until N(w) = N, which then gives the value of w for that particular target and bombarding energy. Once w has been determined, the integral

$$Y_c = \int_{E_2=w}^{E_1} \frac{\sigma}{\epsilon} dE \qquad (3.12a)$$

can now be evaluated and the experimental yield, Y_e, can be compared with the yield, Y_c, calculated from equation 3.12a.

The general technique for obtaining an experimental cross section from yield measurements involves the use of a series of successive approximations in equation 3.12a. For an isolated single level a first approximation for σ in this equation would be the Breit-Wigner single level formula (equation 3.6). The yield Y_c is calculated using this σ; the ratio Y_e/Y_c is then plotted as a function of energy. If this ratio is a constant independent of energy a fit has been obtained. If not, a new cross section $\sigma' = \sigma Y_e/Y_c$ is used in equation 3.12a and the above series of steps carried through again, yielding a plot of the ratio Y_e/Y_c', where

$$Y_c' = \int_{E_2=w}^{E_1} \frac{\sigma'}{\epsilon} dE \cdot \qquad (3.12a')$$

A third trial cross section $\sigma'' = \sigma' Y_e/Y_c'$ is now used in equation 3.12a. This procedure is continued until the ratio of experimental to theoretical yield

within the limits of experimental error is a constant. The trial value for the cross section that yielded this constant ratio now represents the experimental cross section.

In the $C^{13}(p, \gamma)$ reaction in the proton energy region below 500 kev this procedure proved quite successful. There were two reasons for this. First, the monotonically increasing cross section in this region (except in the vicinity of the 448 kev resonance which was too narrow to have any effect a few kev away) led to a slowly varying value for Y_e/Y_c which in turn led to a rapid convergence of the yield ratio to a constant. Second, the ratio Y_e/Y_c was theoretically expected to deviate from a constant value in a known way. This deviation could be caused by two processes. There was the possible interference of a non-resonant capture with the resonant capture (s-waves with channel spin 1) which has been treated by R. G. Thomas (1952) who included a factor

$$\left[1 + \alpha (E_{Res} - E)\right]^2 \qquad (3.13)$$

multiplying the resonance expression 3.6, the constant α depending on nuclear factors. There may also be non-interference terms contributing to the integrated cross section. These non-interference terms were estimated by computing the tail of the 1250 kev $C^{13}(p, \gamma)$ resonance over the range of energies investigated experimentally. It was found that, to 2 percent, the ratio $\sigma(E_R = 1250)/\sigma(E_R = 555) = cE_p + b$, a linear function of the energy, for all $E \leq 450$ kev. Since the tail of the 1250 kev resonance is dominated by the barrier penetration factor, it was expected that any other noninterfering non-resonant process, also dominated by the barrier

penetration factor, will give a linear function of energy when compared with the 555 kev resonance tail. Furthermore, the coefficient α in the extra term suggested by Thomas for the interference process is of such a magnitude that equation 3.13 is very nearly a linear function of energy below 500 kev. Using α as a parameter, an excellent fit to Y_e/Y_c was obtained in the energy range below 500 kev. The second trial value for σ produced a fit to the data that was within the experimental error down to the lowest energy at which data was taken. However, this lowest energy point, taken at a proton bombarding energy of 92.4 kev, was found to lie 1.5 standard deviations above the curve of equation 3.13. This was not considered unusual since one of twenty points is expected to fall outside two standard deviations and one of three outside one standard deviation. As this point represented the lowest energy at which data was taken, however, the discrepancy led to the unsuccessful attempt described in Section II-D to remeasure the cross section at 92 kev by using a mass-one beam.

The success in fitting the experimental data in the low energy region by using the successive approximation technique was not repeated in the vicinity of the resonance at 555 kev. In this energy range the technique proved virtually useless since the ratio Y_e/Y_c varied unpredictably with energy and any fit that could have been made to this ratio would not have had any significance in relation to the Breit-Wigner single level formula. Small changes in the resonance energy or the reduced width led to gross changes in the shape of this ratio. A satisfactory fit to the experimental yield was eventually obtained by choosing the resonance parameters in the cross section through trial and error. However, the sensitiveness of the yield ratio to changes in the resonance energy and in the reduced width

led to quite an accurate determination of these parameters. Thus, a variation of the resonance energy by less than 500 ev would nullify the fit. This error is, of course, only a relative value since the error in the calibration constant of the electrostatic analyzer gives an energy error of ±1.5 kev.

When the resonance parameters obtained were substituted into equation 3.5 and equation 3.6, Y_c was found to fall considerably below Y_e at higher energies. At the highest energy attained, 680 kev, the single level formula (omitting the Thomas correction factor) fell 25 percent low. The inclusion of the Thomas correction, which would have led to an even greater discrepancy since it is less than unity above the resonance energy, was not justified, since, as explained above, the empirically determined value of α in equation 3.13 represents the sum of contributions from both interfering and non-interfering distant resonances. Above the 555 kev resonance this sum can give a factor either greater than or less than unity since the non-interfering contributions are additive here as well as below the resonance. Presumably, then, the discrepancy at higher energies is a result of the presence of the tails of noninterfering resonances of higher energies. The cross section below 680 kev of the 1250 kev resonance in the $C^{13}(p, \gamma)$ reaction was of insufficient magnitude to secure a fit to the data. However, there appear to be inconsistencies in the analysis of the experimental data that led to the 1250 kev assignment for the resonance energy. These inconsistencies are directly related to the Humblet-Rosenfeld resonance theory and will be discussed in some detail in Section V. The lack of high energy data of sufficient accuracy made it impossible to extrapolate, with any

precision, cross sections to the region below 700 kev and thus precluded the attainment of a fit to the experimental data above an energy of 570 kev.

E. Results and Comparison with Other Measurements

In Figure 16 a plot of Y_e/Y_c for all the data taken in this experiment is presented. The cross section used to calculate Y_c for all these points was the Breit-Wigner single level formula without the Thomas factor. The curve drawn in Figure 17 represents an empirical fit using the Thomas factor with a value for a of 0.684 Mev^{-1}. This curve fits the data quite well below 580 kev. In the vicinity of the resonance (from 535 to 575 kev) the single level formula (equation 3.6) fits the data to slightly better than 1 percent which can be seen in Figure 16. The parameters used to obtain this fit are:

$$\begin{aligned} \gamma_p^2 &= 570 \text{ kev or} \\ \theta_p^2 &= 0.190 \\ E_\lambda &= 555 \text{ kev} \\ a &= 0.684 \text{ Mev}^{-1} \end{aligned} \qquad (3.14)$$

The allowable variation in γ_p^2 that will still give a fit to the data is ±10 kev, and, as mentioned above, the error in E_λ is ±1.5 kev.

At the resonant energy the total width calculated from $\gamma_p^2 = 570$ kev is 38.2 kev. The laboratory width (full width at half maximum) is 37 kev. The maximum cross section occurs at a proton laboratory bombarding energy of 553.5 kev, 1.5 kev below the resonance energy.

The energy region from 538 kev through 590 kev was covered in 2.5 kev steps, and the two regions between 430 kev and 538 kev and between 590 kev and 682 kev were covered in 5 kev steps. The small steps, thin

targets, and excellent fit to the data in the 530 to 580 kev range indicate that the Breit-Wigner single level formula provides, in detail, an excellent theoretical formula to fit resonance data. The calculations of Humblet and Rosenfeld (1961) point to a slightly different expression for a single level formula. The differences between these two formulas will be examined in detail in Section V, in which a fit to this same data using the Humblet-Rosenfeld single level formula is attempted. The results reported here do not agree very well with the cross section values of Hester and Lamb (1961) for energies 100 kev $\leq$ Ep $\leq$ 140 kev and this discrepancy remains unresolved. However, the agreement with the measurement by Woodbury and Fowler (1952) at 129 kev, is good. The results from both these experiments are included in Figure 26.

Figure 17 is a plot of the $C^{13}(p, \gamma)$ cross section measured from 90 kev to 680 kev, a region in which the cross section varies over 9 decades. The curve through the data points is the Breit-Wigner single level formula with the parameters of equation 3.14.

Table I lists these experimentally measured cross sections as a function of energy; the error of each point is included. To obtain these cross sections, the gamma radiation was assumed to be isotropic. Previous observations (Broude, et al., 1957 and Wilkinson and Bloom, 1957) indicated that the excited state at 555 kev decays isotropically with 82 percent transition probability to the ground state, 14 percent to the 3.95 Mev 1^- level, and 4 percent to the 2.31 Mev 2^- level. Since these experiments were performed at the 555 kev resonance only, measurements were necessary at lower energies to supply a basis for the assumption of isotropic radiation at all energies. This assumption was tested by obtaining gamma

yields with the NaI(Tl) crystal at two angles, 90^{o} and 0^{o} with respect to the proton beam. Above 303 kev proton bombarding energy the crystal was at 90^{o} to the proton beam at a distance of 3.8 cm from the target and below 303 kev proton energy the detector was at 0^{o} at a distance of 1.9 cm. At the change-over energy of 303 kev, the change of count rate corresponded to that expected for an isotropic distribution. Additional data points, taken at 0^{o} above a proton energy of 400 kev further confirmed the assumption of isotropic radiation since the yields at 0^{o} were equal to those at 90^{o}. Changes in the transition probabilities were also looked for and not found. Yields of gamma rays from the $C^{13}(p, \gamma)$ reaction above 200 kev proton energy were measured between 3.2 Mev and 5 Mev and between 5 Mev and 8 Mev and indicated that no change in the proportions of the radiation was taking place.

An upper limit may be placed on the strength of radiation from any resonances in the $C^{13}(p, \gamma)$ reaction. Except at 448 kev and 555 kev no such resonances were observed in the energy range from 70 kev (the back edge of the target at a bombarding energy of 100 kev) up through 680 kev. This covers the excitation range in N^{14} from 7.61 Mev through 8.18 Mev. If the high yield at 92.4 kev was caused by an unknown resonance rather than a statistical fluctuation, this resonance must lie between 60 and 70 kev. This location is determined by, first, an increased yield at 92.4 and a normal yield at 102.5 kev, and, second, a target of thickness 32 kev at a proton energy of 100 kev. The excitation energy of this level in N^{14} would be 7.60 Mev. The existence of such a level is to be seriously doubted, however, for two reasons. First, the deviation of the last data point, the only one to indicate the level's possible existence, from the expected value was not statistically significant, and, second, the reduced width of this level, if it were formed by an s-wave proton

capture, would be on the order of $1 - 3 \times 10^{-7}$ of the Wigner limit, a value much smaller than any previously observed resonance in the light nuclei (Vogt, 1959).

In Table II the upper limits to unobserved resonances are tabulated as a function of energy. For comparison, a proton width corresponding to 1 percent of theWigner limit is tabulated for various proton orbital angular momenta. It is clear that levels up to J = 5 would stand a very good chance of having been detected, the limit being provided by the radiative width, rather than the proton width. Radiation up to octopole order could probably have been detected, and there are states up to J = 3 below 7.5 Mev excitation that could participate in cascades to the ground state.

IV. The $C^{12}(p, \gamma)$ Reaction

A. Targets

The yield of gamma radiation produced by the bombardment of C^{12} with protons was determined, as in the C^{13} case, in three distinct energy regions, uutilizing three different techniques. The first region included energies above 300 kev and below 480 kev, in which targets of 61 percent C^{13}, 39 percent C^{12}, of accurately known thicknesses were used. The second region, below 300 kev, was investigated with a soot target of unknown thickness while in the region above 480 kev, targets of a calculable thickness, produced by cracking methyl iodide, were utilized.

1. Measurements with Enriched C^{13} Targets

Targets enriched in C^{13} were useful in measuring yields of gamma rays from $C^{12}(p, \gamma)$ reaction because the thicknesses of these targets could be easily measured using the technique described in Part III-C. In fact, the same spectra that provided measurements of the $C^{13}(p, \gamma)$ cross section in the energy range below 445 kev provided suitable data for determining the $C^{12}(p, \gamma)$ cross section. Since the time-dependent background subtraction was known accurately in all cases, subtracting it presented no problems. However, the estimate of the subtraction necessary to eliminate the $C^{13}(p, \gamma)$ spectrum was considerably less accurate. The intensity of the 2.31 Mev gamma ray, coming from several different cascades in this reaction (see Figure 1), is not known with sufficient accuracy. Therefore, the $C^{12}(p, \gamma)$ yield from the C^{13}-enriched targets was used in the cross section determination only down to 295 kev. At 295 kev proton energy, the beam dependent background subtraction was considerably less than the $C^{12}(p, \gamma)$ yield, but the magnitudes reversed within the next

50-kev lower proton energy. Therefore, below 295-kev the C^{13}-enriched targets were no longer useful for measuring the $C^{12}(p, \gamma)$ cross section.

2. Measurements with Soot Targets

Cross section measurements in the energy range below 295 kev were made with a carbon target of natural isotopic abundance. This target was made by holding a tantalum target blank over a gas flame. In the energy range from 380 kev to 195 kev, a calculation of the ratio of yield to cross section as a function of target thickness was made. Since the target used was thought to be 18 kev thick, thicknesses of 9 kev, 18 kev, and 27 kev were used in this calculation. The differences in the energy dependence of the ratio for these three cases were less than the errors in the experimental yield, and thus the energy dependence of the experimental cross section obtained from this yield was not strongly influenced by the assumed target thickness. The cross sections in this energy range were normalized so that, in the overlap with the range 303-380 kev measured with the enriched targets, the two sets of data fitted together smoothly. Yield measurements could not be continued below 195 kev because of the increasing importance of the time dependent background. Most of this background was contributed by the 2.62 Mev gamma ray from the decay of environmental Thorium C" . However, several previous measurements of the reaction cross section had been made in the energy range below 195 kev (Hall and Fowler, 1950, Lamb and Hester, 1957 and Bailey and Stratton, 1950) and it was unnecessary to extend the measurements to lower energies in this experiment.

3. Measurements with Natural Methyl Iodide Targets

Above 480 kev the subtraction necessary to eliminate the $C^{13}(p, \gamma)$ spectrum became too large to permit using the C^{13} enriched targets. The gamma yield from the tail of the resonance at 555 kev in the $C^{13}(p, \gamma)$

reaction increases rapidly with energy while the yield from the tail of the resonance at 462 kev in the $C^{12}(p, \gamma)$ reaction decreases. Since the peak $C^{13}(p, \gamma)$ cross section is an order of magnitude greater, the $C^{13}(p, \gamma)$ reaction dominates the spectrum above 480 kev. Measurements above this energy were made using targets obtained by cracking methyl iodide synthesized from natural carbon. The cracking procedure was as nearly identical to that used for making the C^{13} targets (part II-A) as possible; the experience gained in making the C^{13} targets would then permit making reasonable thickness estimates of the C^{12} targets. Since there are no narrow $C^{12}(p, \gamma)$ resonances in the energy range under observation, a procedure different from that used with the C^{13} -enriched targets was necessary to obtain accurate estimates of the C^{12} target thicknesses. The procedure used is described in some detail below.*

The $C^{12}(p, \gamma)$ spectrum in the range from 400 to 480 kev proton energy was detected using first an enriched target. Since the $C^{13}(p, \gamma)$ yield is relatively small in this energy region, it contributed a small uncertainty to the $C^{12}(p, \gamma)$ yield from the enriched target. The thickness of the enriched target, Δt_e, had been accurately determined by the method described in Section III-C. With the known target thickness (two targets were actually used of thicknesses 4.1 kev and 8.7 kev) and experimental yield data it was then possible to extract a cross section for the $C^{12}(p, \gamma)$ reaction by the same method as described in Section III-D, i.e., by integrating

*Determining the target thickness by elastic scattering of protons would have presented several difficulties. The greatest of these would be caused by the buildup of carbon that would occur during the measurements. The problem of nonuniformities in the target and the rather poor (for elastic scattering) surface finish of the tantalum backing provided additional problems.

$$Y_e(E_1) = \int_{E_1 - \Delta t_e}^{E_1} \frac{\sigma}{\epsilon_e} dE \qquad (4.1)$$

where the subscript "e" refers to the enriched target. Once σ had been determined, the measurement was repeated with a natural target of unknown thickness, Δt_n, and the integral

$$Y_n(E_1) = \int_{E_1 - \Delta t_n}^{E_1} \frac{\sigma}{\epsilon_n} dE \qquad (4.2)$$

evaluated, in which the subscript "n" refers to the natural target. The unknown in equation 4.2 is Δt_n, the thickness of the natural target, which is determined by integrating the expression with a variable lower limit and comparing the result with the experimentally measured $Y_n(E_1)$. The value of ϵ_e and of ϵ_n in these equations is given by $\epsilon_e = \epsilon/P_e$ and $\epsilon_n = \epsilon/P_n$ where ϵ is the tabulated stopping cross section of carbon (Whaling, 1958), and P_e and P_n are, respectively, the number percentages of C^{12} present in the enriched and natural targets.

Once the value of Δt_n had been determined for a particular target, this target could be used to extend the $C^{12}(p, \gamma)$ cross section measurements above 480 kev by again using equation 4.2 but with σ as the unknown.

Gamma ray yield data were obtained up to an energy of 680 kev at which point the electrostatic analyzer broke down electrically. Several targets of thicknesses from 8 to 17 kev were used. After the thickness of the first had been determined by the above described technique, the thickness of each of the others was determined by a yield comparison with this first target.

B. Obtaining Cross Sections from the Gamma Ray Yield

1. The Resonance Parameters

The conversion from yield to cross section was accomplished for the $C^{12}(p, \gamma)$ reaction in the manner used for the $C^{13}(p, \gamma)$ reaction as explained in Section III-D. The first trial value for the cross section in equation 3.5 was again a Breit-Wigner single level formula, including all the energy dependences that were calculated for the $C^{13}(p, \gamma)$ case.

The trial value of E_λ (Equation 3.6) was taken to be 462 kev, the value found by Milne (1954). A satisfactory fit to the data was obtained using the following parameters, all of which refer to the laboratory system:

$$\begin{aligned} E_\lambda &= 462 \text{ kev} \\ \gamma_p^2 &= 1695 \text{ kev, or} \\ \theta_p^2 &= 0.567 \\ \omega\Gamma_\gamma &= 1.52 \text{ ev} \\ R &= 4.64 \text{ fermis} \end{aligned} \tag{4.3}$$

These parameters lead to a peak cross section of 127 μb at an energy of 460.5 kev, the cross section measured by Seagrave (1951).

The experimental data was of insufficient accuracy to rule out a resonance energy of 461 kev, the value reported by Jackson and Galonsky (1953). However, calculations made with a resonance energy of 456 kev, as reported for the $C^{12}(p, \gamma)$ reaction by Hunt and Jones (1953), fell outside the uncertainty in the data.

The proton width quoted in equation 4.3 was determined by the method of approximation described in Section III-D. At the resonant energy the

theoretical laboratory width, obtained from equation 3.9 using γ_p^2 = 1695 kev, is 36 kev. The laboratory width (full width at half maximum) is 35 kev. Previous investigations led to estimates for the laboratory width of 34 kev (Jackson and Galonsky, 1953) and of 35 kev, (Milne, 1954) in good agreement with the value measured here.

The plot of the experimental cross section divided by the Breit-Wigner single level formula is given in Figure 21. The points were fitted with the Thomas factor, equation 3.13 in which α = 1.185 Mev^{-1}. The curve of equation 3.13 with these parameters also appears in Figure 21 and passes satisfactorily through the lower energy cross section measurements of Baily and Stratton (1950) of Hall and Fowler (1950) and of Lamb and Hester (1957) in the extrapolation to stellar energies.

Table III is a list of the experimentally determined $C^{12}(p, \gamma)$ cross sections tabulated as a function of proton laboratory energy. Figure 19 is a log plot of the cross section. The curve in this figure is the fit of equation 4.3.

2. Target Thickness Uncertainties

The greatest source of uncertainty in the value of E_λ in equation 4.3 lies in the thickness estimates of the natural carbon targets. The indirect thickness measurement, described in IV-A-3 necessarily led to larger errors in the thickness than existed with the enriched targets. In particular, the accuracy of the cross section which enters into the calculation of the thickness was impaired by the presence of the 448 kev resonance in the $C^{13}(p, \gamma)$ reaction. At this resonance, as described in Part VII, Section A-5, half of the gamma rays produced represent decays to the 4.03 Mev state in N^{14}. This state decays with 98 percent transition

probability to the 2.31 Mev state which then decays to the ground state. Thus at the 448 kev resonance the relative yield of 2.31 Mev and 1.72 Mev gamma rays is increased four-fold over the relative yields from the tail of the 555 kev resonance. Moreover, this factor of four is approximate, with an accuracy of ±15 percent, so that the $C^{13}(p, \gamma)$ spectrum subtraction is unreliable in the energy region from 446 kev to 450 + Δt kev, Δt being the target thickness. Unfortunately, this energy region coincides with the region of maximum cross section in the $C^{12}(p, \gamma)$ reaction. Thus the enriched C^{13} targets could not provide usable data for this reaction in this region. Furthermore, a gap in Y_e in this critical energy region led to difficulties in extracting the cross section from Y_e at the higher energies. Very thin targets, say Δt = 3 kev, did not solve the problem, however, because a) the uncertainty in Δt becomes large ($\approx$ ±10 percent), b) the time dependent background corrections become more important and c) the effects of carbon deposition on the target (to be discussed in more detail below) become more serious. In the end, the enriched targets were not useful for measuring the $C^{12}(p, \gamma)$ yield above 446 kev. This was regrettable because the cross section is a monotonically increasing function of energy up to this point, and thus the uncertainty in the target thickness calculated from equations 4.1 and 4.2 was larger than the uncertainty in the yield. The target thickness, typically 10 to 15 kev at 448 kev, was estimated to have an uncertainty of ±3 to ±4 kev, caused by the above described effects. This uncertainty in target thickness leads in turn to an uncertainty in the value of the resonance energy, E_λ, of ±1.5 to ±2.0 kev, which uncertainty must be combined with those of the beam energy (±1.5 kev) and the allowable variation in E_λ in the Breit-Wigner formula that still fits

the experimental data (±0.5 kev) to obtain an overall estimate of the accuracy in E_λ of ±2.3 kev. The uncertainty in the value of γ_p^2 in equation 4.3 is ±8 percent. This uncertainty results primarily from an allowable variation of ±7 percent in γ_p^2 in the Breit-Wigner formula. The contributions from the uncertainty in target thickness and beam energy were less than 4 percent.

3. Carbon Deposition

A serious problem connected with the $C^{12}(p, \gamma)$ reaction that did not exist for the $C^{13}(p, \gamma)$ reaction resulted from carbon deposited on the target from diffusion pump oil vapor. Since the abundance of C^{13} in natural carbon is only 1.1 percent, no appreciable change in the thickness of the C^{13} target occurs through this deposition and only small corrections to the bombarding energy, equal to the thickness of the deposited carbon layer, resulted. On the other hand, for the $C^{12}(p, \gamma)$ reaction, this carbon increased the target thickness rather than changed the effective bombarding energy, and, in addition, the composition of this additional layer is unknown. The $C^{12}(p, \gamma)$ yield data was therefore checked by regularly measuring the yield at a particular energy for each of the natural targets. When this yield increased by more than two standard deviations the target was no longer used. A target of 5 kev thickness would become unusable when only 50 ev of carbon had been deposited if a one percent accuracy in σ was desired. It would have been quite difficult to achieve the accuracy in the $C^{12}(p, \gamma)$ measurements that had been attained in the $C^{13}(p, \gamma)$ case, since the accuracy in this latter case was attained by utilizing targets of thicknesses 2.5 to 3 kev, which, for the $C^{12}(p, \gamma)$ reaction, would not have been usable because of reasons (b) and (c) in Section II above.

V. EXPERIMENTAL EXAMINATION OF THE HUMBLET-ROSENFELD THEORY

J. Humblet and L. Rosenfeld (1961) have formulated a general theory of nuclear reactions using complex values for the total energy of the compound system with what they call "natural" boundary conditions, i.e., "the absence of incoming waves in all channels." Their theory leads to a total cross section which is a sum over an infinite number of terms. The Humblet-Rosenfeld single level cross section is obtained by retaining only one term in this sum. For a (p, γ) reaction this cross section is:

$$\sigma_{H\text{-}R} = \pi\lambda\!\!\!^{-2} \frac{\omega \Gamma_p \Gamma_\gamma}{(E - E_R)^2 + \frac{\Gamma_R^2}{4}} \quad . \tag{5.1}$$

This formula is quite similar to the Breit-Wigner single level formula

$$\sigma_{B\text{-}W} = \pi\lambda\!\!\!^{-2} \frac{\omega \Gamma_p \Gamma_\gamma}{(E - E_\lambda - \Delta_\lambda)^2 + \frac{\Gamma^2}{4}} \tag{5.2}$$

although certain important differences exist between the denominators in these cross sections. The quantities E_R and Γ_R in the Humblet-Rosenfeld theory are constants, independent of energy, in contradistinction to Δ_λ and Γ in the R-matrix theory (Lane and Thomas, 1958).

One of the purposes of the experiments reported here was to attempt to determine experimentally which of these two resonance expressions provides the most accurate theoretical fit to the experimental data. Initially it had been planned to make a careful (p, γ) cross section measurement on a well isolated level, in particular the 462 kev resonance in the

$C^{12}(p, \gamma)$ reaction,* to determine whether a constant width (as in the Humblet-Rosenfeld theory) or a variable width (as in the R-matrix theory) would more accurately fit the data. However, subsequent calculations, which are described below, illustrate the extreme difficulty of attempting to make an experimental distinction between the two formulae.

As described in Section III, the $C^{13}(p, \gamma)$ reaction data could not be successfully fitted to the Breit-Wigner formula at energies above 570 kev. Nevertheless, below this energy the theoretical fit was remarkably accurate. The difference between the experimental data and the theoretical fit was less that 1 percent for energies near the resonance energy, $(E_R - \Gamma \lessdot E \lessdot E_R + \Gamma)$ and it is unlikely that any change in the form of the cross section would produce a better fit to the data. In the course of this analysis of the resonance data, a seemingly little known property of the Breit-Wigner cross section was noted. This property is most easily demonstrated by observing the behavior of the cross section when $(E - E_\lambda - \Delta_\lambda)^2 \lessdot\lessdot \Gamma^2/4$. For these energies, in a (p, γ) reaction, $\sigma_{BW} \propto \Gamma_\gamma \Gamma_p / \Gamma^2$. At and above the 462 kev resonance in the $C^{12}(p, \gamma)$ reaction and the 555 kev resonance in the $C^{13}(p, \gamma)$ reaction, $\Gamma_\gamma \lessdot\lessdot \Gamma_p$ and thus $\Gamma \approx \Gamma_p$. For these reactions, then, $\sigma_{B-W} \propto \Gamma_\gamma / \Gamma_p \propto 1/P$, where P is the penetration factor; the cross section peak will thus be shifted to an energy lower than the resonance energy. In a case where other widths are present, and greater than Γ_p, the above approximation

*The total width of the 462 kev resonance is 35 kev with the next nearest level at 3.51 Mev, having a width of 7 kev. Since this level is well known to be the first excited state in N^{13}, there is the additional advantage of having no levels at lower energies to add additional terms to the cross section expression.

will no longer hold and the cross section will be proportional to P, and the maximum cross section will occur at an energy above the resonance energy.

The Humblet-Rosenfeld formula, on the other hand, behaves quite differently under these approximations. Since Γ_R is a constant, the cross section when $(E - E_R)^2 \ll \Gamma_R^2/4$ will be: $\sigma_{H-R} \propto \Gamma_\gamma \Gamma_p \propto P$. With the cross section proportional to the penetration factor, the peak will be shifted to higher energies, exactly opposite to the shift predicted by the Breit-Wigner formula. The ramifications of this difference in behavior will be most apparent in a resonance with a large total width. Furthermore, the magnitude of this difference is expected to be much greater than that produced on the wings of the dispersion curve by a constant or variable total width. Making accurate measurements of these wings is quite difficult because the yield is low compared to the peak and because the effect of distant resonances may not be negligible. There was thus good reason to believe that the 1250 kev resonance in the $C^{13}(p, \gamma)$ reaction would provide an excellent test of the two theories, since this resonance has a total width of 500 kev. (The analysis of this resonance had been originally performed using a formula of the Humblet-Rosenfeld type.) (Seagrave, 1951). To determine the cross section a computer program was written to calculate σ_{B-W} and σ_{H-R} as a function of energy for a resonance of laboratory width 500 kev and peak cross section at an energy of 1310 kev, the latter figure representing this author's estimate from the originally published data (Seagrave, 1951). After several variations of the parameters the resonance energy was fixed at 1270 kev using σ_{H-R} and 1370 kev using σ_{B-W}, a difference of 100 kev. However,

the ratio of these two theoretically calculated cross sections (Figure 18) did not show the expected proportionality to P^2 near $E = E_R$. In fact, the variation with energy of $\sigma_{H\text{-}R}/\sigma_{B\text{-}W}$ could be fitted to the function $\left[1 + A(E - E_R)\right]^2$ (equation 3.13) to 5 percent down to energies where the 555 kev resonance becomes dominant in the cross section. This fit is demonstrated by the dashed curve in Figure 18. Since it appears improbable that data with accuracy greater than 5 percent could be obtained for this wide resonance (there exist too many overlapping narrow levels, and the yield from this level is quite small), it thus cannot provide a test of the two theories.

The surprising results from the calculation at the 1250 kev resonance led to a calculation of the ratio $\sigma_{H\text{-}R}/\sigma_{B\text{-}W}$ for the 555 kev resonance in the same reaction. This calculation led to the curve shown in Figure 20 for this ratio. Included in this figure, as the dashed curve, is a plot of the Thomas factor $\left[1 + A(E - E_R)\right]^2$ with $A = 0.685$ Mev^{-1} and $E_R = 555$ kev, the values that were experimentally determined and reported on in equation 3.14. This factor can easily include all the differences between the two formulae down to 150 kev for data with an accuracy of better than 0.5 percent. Below 150 kev, the ratio can no longer be fitted by the Thomas factor, but the difference, at 100 kev, is 6 percent, much smaller than the error in the measurements at this energy. The discrepancy at low energies is easily explained in terms of the level shift parameter, Δ_λ, in equation 5.2. When $(E - E_\lambda - \Delta_\lambda)^2 >> \Gamma^2/4$, $(\sigma_{H\text{-}R}/\sigma_{B\text{-}W}) = (E - E_\lambda - \Delta_\lambda)^2/(E - E_R)^2$. Keeping the first term from a power series expansion for Δ_λ around $E = E_\lambda$ gives, $(\sigma_{H\text{-}R}/\sigma_{B\text{-}W}) \propto \left[1 + \delta/(E - E_R)\right]^2$ where $\delta = E_R - E_\lambda$. A plot of $\Delta_\lambda/\gamma^2 = -S$ for the $C^{13}(p, \gamma)$ reaction is shown

in Figure 19. The straight line approximation to this curve at 555 kev can be seen to fit quite well over a wide energy range. However, below 350 kev, the curve falls away from the straight line, which leads directly to the shape of the ratio curve of Figure 20. A similar effect, seen in the ratio curve of Figure 18, is explained by referring to the straight line approximation at 1370 kev in Figure 19.

On the basis of the above calculations it appears that the only detectable difference in the shapes of the resonance cross section is caused by the level shift; the completely different energy dependence of the total width in the resonance denominator yields an experimentally negligible difference between the two resonance shapes. It thus appears that measuring the shape of radiative capture cross sections cannot yield any clues to distinguish between the R-matrix and Humblet-Rosenfeld formulations of nuclear reactions. The presence or absence of an energy dependent level shift provides the only experimental handle to make this distinction, but, since the effect of a level shift is apparent only far from the resonance, the one level approximation is no longer valid in any theory.

The extrapolation of cross sections to lower energies is dependent on the presence or absence of a level shift. However, since both the $C^{12}(p, \gamma)$ and $C^{13}(p, \gamma)$ cross sections contain essentially identical level shift parameters, the $C^{13}(p, \gamma)$: $C^{12}(p, \gamma)$ cross section ratio at stellar energies will not depend on the resonance theory used. In any case, all experimental fits and extrapolations in this thesis were obtained by using the Breit-Wigner formula.

VI. APPLICATIONS TO STELLAR PROCESSES

The reactions described above, $C^{12}(p, \gamma)$ and $C^{13}(p, \gamma)$, are both links in the conversion of four protons to helium through the CNO cycle. In particular, the low energy cross sections must be known before the rates of reaction in stellar interiors can be predicted. It is usual to define a cross section factor S(E) for use in the reaction rate equations.

A. Reaction Rates

The mean reaction rate of a thermonuclear process can be expressed, using the notation of the review by Burbidge et al., (1957) as

$$P = n_1 n_0 \langle \sigma v \rangle_{AV} \text{ reactions cm}^{-3} \text{ sec}^{-1} \tag{6.1}$$

where n_1 and n_0 are the number densities of the interacting particles per cm^3 and $\langle \sigma v \rangle_{AV}$ is the average of the cross section multiplied by the velocity in cm^3 sec^{-1}. The cross section factor, S(E), in kev-barns is defined by the equation

$$\sigma(E) = \frac{S(E)}{E} \exp\left(-31.28\ Z_1 Z_0 A^{1/2} E^{-1/2}\right) \tag{6.2}$$

where σ is the reaction cross section, E the center of mass interaction energy in kev, Z_1 and Z_0 the charges of the interacting nuclei and $A = A_1 A_0/(A_1 + A_0)$ is their reduced mass number. Referring to the development of Caughlan and Fowler (1962), one can write in a non-resonant region with good approximation:

$$S(E) = S(0) + E \left\langle dS/dE \right\rangle . \tag{6.3}$$

For a Maxwell-Boltzman distribution in energy for the interacting particles, they found:

$$P_{nr} = 7.20 \times 10^{-19} n_1 n_0 \frac{f_o S_{eff}}{A Z_1 Z_0} \tau^2 e^{-\tau} \tag{6.4}$$

where

$$\tau = 42.48 \left(Z_1^2 Z_0^2 \frac{A}{T_6} \right)^{1/3} \tag{6.4a}$$

and

$$S_{eff}\left(T_6\right) = S(0) \left\{ 1 + \frac{5}{12\tau} + \frac{\langle dS/dE \rangle}{S(0)} \left[E_o(T_6) + \frac{35}{36} kT_6 \right] \right\} \tag{6.4b}$$

in which $S(0)$ and $\langle dS/dE \rangle$ are empirically determined constants, T_6 is the temperature in 10^6 degrees, and f_o is the electron screening or shielding factor.

The effective thermal energy is given by:

$$E_o = 1.220 \left(Z_1^2 Z_0^2 A T_6^2 \right)^{1/3} \tag{6.5a}$$

and the width of the effective range of thermal energy by

$$\Delta E_o = 0.75 \left(Z_1^2 Z_0^2 A T_6^5 \right)^{1/6} \text{ kev} \tag{6.5b}$$

It is known (Burbidge, et al., 1957 and Caughlan and Fowler, 1962) that the $N^{14}(p, \gamma)$ reaction is much slower than any of the other reactions in the CNO

chain and thus determines the reaction rate of the entire chan. The presence or absence of a resonance at low bombarding energies in the $C^{12}(p, \gamma)$ or $C^{13}(p, \gamma)$ reactions will therefore not change the rate of hydrogen burning in the chain or determine the temperature of the star.

B. The $C^{12}(p, \gamma)$ Reaction

A plot of S(E) versus the center of mass energy for the $C^{12}(p, \gamma)$ reaction is presented in Figure 23, which includes the data of Bailey and Stratton (1950), of Hall and Fowler (1950), and of Lamb and Hester (1957), as well as the fit of equation 4.3 to the experimental data. From this plot one obtains $S(0) = 1.21 \pm 0.15$ kev-barn and $\langle dS/dE \rangle = 5.81 \times 10^{-3}$ barns.

C. The $C^{13}(p, \gamma)$ Reaction

A plot of S(E) versus the center of mass energy for the $C^{13}(p, \gamma)$ reaction is presented in Figure 24, which includes the data of Hester and Lamb (1961), and of Woodbury and Fowler (1953), as well as the fit of equation 3.14 to the experimental data. From this plot one obtains $S(0) = 5.5 \pm 0.8$ kev-barn and $\langle dS/dE \rangle = 1.94 \times 10^{-2}$ barns.

The usefulness of the extrapolated value of S depends critically on the absence of resonances below the lowest energy at which experimental cross section measurements were made. In the $C^{12}(p, \gamma)$ reaction there is every reason to believe that the resonance at 462 kev is the first excited state in N^{13} from both experimental results and shell model calculations. In the $C^{13}(p, \gamma)$ reaction, however, low lying levels cannot be excluded with equal certainty. If resonances do, indeed, exist below 70 kev proton energy the above extrapolation of S(E) into this region will be invalid.

The reaction rate in this latter case will be given by (Burbidge, et. al., 1957):

$$P_r = 3.08 \times 10^{-15} \, n_1 n_0 \frac{f_r}{A^{1/2} T_6^{3/2}} S_r \Gamma e^{-\tau_r} \tag{6.6}$$

where

$$\tau_r = 31.28 \, Z_1 Z_0 A^{1/2} E_r^{-1/2} + 11.61 \frac{E_r}{T_6} \tag{6.6a}$$

$$S_r = 1.25 \times 10^4 \frac{\theta_p^2 \, 1 - \alpha_\ell E_r}{A \; K^2_{2\ell+1}(x)} \frac{\omega E_r}{\Gamma_\gamma} \tag{6.6b}$$

in which the notation of Burbidge et.al., (1957), has been used with the assumption that $\Gamma_\gamma \gg \Gamma_p$, and that the resonance E_r falls within the range $E_o - 2\Delta E_o \ll E_r \ll E_o + 2\Delta E_o$. If one neglects $\alpha_\ell E_r$, these expressions above lead to

$$P_r = 4.14 \times 10^{-8} \frac{n_H n_{C^{13}} f_r}{K^2_{2\ell+1}(3.0)} \frac{\omega \theta_p^2}{T_6^{3/2}} e^{-\tau_r} \tag{6.6}$$

Using equation 6.4 one obtains for the non-resonance reaction rate:

$$P_{nr} = 1.46 \times 10^{-14} \frac{n_H n_{C^{13}} f_o}{T_6^{2/3}} e^{-\tau} \tag{6.4}$$

The ratio of these reaction rates will indicate the relative importance of an unobserved level. If it is assumed that the electron shielding factors f_r and f_o are equal this ratio is:

$$\frac{P_r}{P_{nr}} = 2.84 \times 10^6 \frac{\omega\theta_p^2}{K^2_{2\ell+1}(3.0)} T_6^{-5/6} e^{-(\tau_r - \tau)} \qquad (6.7)$$

in which

$$\tau_r - \tau = 181.5\, E_r^{-1/2} + 11.61 \frac{E_r}{T_6} - 137.2\, T_6^{-1/3} \qquad (6.7a)$$

A plot of the ratio P_r/P_{nr} is given in Figure 26, for which $\omega\theta_p^2 = 0.01$, a typical value for a dimensionless reduced width in the light nuclei. A temperature of 15×10^6 degrees has been assumed in the plot. Figure 25 is a plot of T_6 versus E_r for the ratio P_r/P_{nr} set equal to unity. Included in the plot is the curve of E_o given by equation 6.5a.

It is interesting to note that the maximum of equation 6.7 occurs when $\tau_r = \tau$, and is, for $\ell = 0$,

$$\left.\frac{P_r}{P_{nr}}\right|_{max} = 1.1 \times 10^9\, \omega\theta_p^2 T_6^{-5/6} \qquad (6.8)$$

If a resonance were present between 60 and 70 kev, as discussed in Section III-E, then, as was shown there, $\omega\theta_p^2 \approx 1 - 3 \times 10^{-7}$. Taking the case where the resonance would be most effective, i.e., when $E_r = E_o$, we have $E_r = E_o = 60$ kev or $T_6 = 60$ which gives $(P_r/P_{nr})_{max} \approx 10$. When T_6 is not near 60, of course, this ratio will be much smaller. By referring to figure 26 it is apparent that the effect of any resonance that could have caused the increase in yield at the 92 kev data point would be significant under only most unusual conditions and, at temperatures typical of the sun and other main sequence stars, the effect becomes completely negligible.

D. Cross Section Ratio

The ratio of the $C^{13}(p, \gamma)$ to the $C^{12}(p, \gamma)$ cross section factor when extrapolated to stellar energies ($\sim$ 25 kev), is found to be 4.5 ± 0.8, a value not very different from the previously reported value of 5.1 ± 1.9 (Burbidge, et. al., 1957). The uncertainty in this cross section ratio will not be very different from the uncertainties in the individual cross sections, since the major sources of error are not removed by taking the ratio. The major sources of error are thought to lie in estimating the fraction of the gamma-ray spectrum used in measuring the yield of gamma rays, and in the estimate of the carbon contamination developed on the target surface for which a correction was applied to the $C^{12}(p, \gamma)$ yield. This last correction was made on the data obtained from the target used for the simultaneous measurement of both cross sections. Using a single target for measuring both eliminated the error resulting from uncertainties in measuring target thicknesses. Less important sources of error that are largely removed on taking the cross section ratio are those involving charge integration, the crystal solid angle, and the tabulated gamma-ray efficiency.

Climenhaga (1960) has made measurements of the $C^{12}C^{13}$ molecular band spectra from several R- and N-type stars. A curve of growth analysis led to values of 4.7:1 to 5.8:1, for the C^{12}:C^{13} ratio consistent with the cross section ratio obtained here. These selected carbon rich stars are believed to be burning on the CNO-cycle, but it is not necessary to assume that the entire cycle is in equilibrium. Provided the formation and destruction of the C^{13} present occurs by means of the reactions $C^{12}(p, \gamma)N^{13}(\beta)$ $C^{13}(p, \gamma)N^{14}$, the requirement of an equilibrium in the amount of C^{13}

present is sufficient to require that the C^{12}:C^{13} abundance ratio should be equal to the inverse ratio of their cross sections for proton capture provided that account is taken of the center of mass effects (see equation 6.4). These effects cause the C^{13}/C^{12} cross section ratio to have the value 4.1 ± 0.7 for a temperature of 15×10^6 °K. The additional terms introduced into the reaction rate because of the energy variation of S(E) have been discussed in detail by Caughlan and Fowler, (1962).

Since C^{12} can be produced in stars by helium burning, the C^{12}:C^{13} ratio is expected to be larger, in general, than the 4.1 measured here experimentally. Thus any stellar abundance observation which gives a larger ratio can be said to be in agreement with this experiment, but a single smaller ratio would cast grave doubts on our understanding of stellar nuclear processes. On the other hand, any low energy resonance in the C^{13}(p, γ) reaction would lead to a greater predicted value for the C^{12}:C^{13} ratio and could not be in agreement with the measurements of Climenhaga. In this case some other mechanisms in the CNO cycle would have to be invoked to explain the large amounts of C^{13} present in some stars.

VII. RADIATIVE CAPTURE AT THE 448 KEV RESONANCE IN $C^{13}(p, \gamma)$

A. Experimental Measurements

1. Energy and Width of the Resonance

During the course of this work a new resonance was found in the $C^{13}(p, \gamma)$ reaction at an excitation energy in N^{14} of 7.966 Mev. The excitation energy was determined by measuring the position of the resonance to be 448.5 ± 0.5 kev, with the $F^{19}(p, \alpha\gamma)$ reaction at 340.4 ± 0.4 kev (Morrish, 1949) used to calibrate the electrostatic analyzer. The excitation function of Figure 27, which shows the dependence of the count rate on the proton energy for the ground state gamma ray, indicates that the resonance has a total width of less than 400 ev. The upper limit to the width of the resonance is sufficiently small to explain the absence of an anomaly in elastic scattering experiments (Milne, 1954 and Hebbard and Vogl, 1960).

2. Positioning the Detection Crystal for Angular Distribution Measurements

An attempt was made to determine the spin and parity of this new level by carrying out angular distribution measurements. To obtain the angular distribution of the gamma rays with respect to the incident protons a 4 inch by 4 inch NaI(Tl) crystal 8.25 cm from the target was used to detect the gamma rays. The positioning of this crystal with respect to the beam spot on the target is quite critical if the distributions are to be determined accurately. In particular, there are two alignments that must be carried out with great care. First, the axis of the crystal must pass through the center of the beam spot on the target and lie in the plane of rotation. Second, the distance between target and crystal must remain

a constant as the crystal rotates about the target. The series of successive adjustments made on the apparatus to achieve this accurate alignment made it possible to measure the following quantities with the indicated accuracy:

i. Uncertainty in angular position of crystal: $\pm 0.2^{o}$

ii. Variation in distance from target to front surface of crystal: $\pm 1/4$mm.

The data was taken with the same crystal and electronic instruments as described in Section II-B for the cross section measurements and will not be further described here.

3. Corrections to the Angular Distribution Data

Several corrections were made to the angular distribution data. First, small changes in gain occurred. These were accounted for by comparing positions of the ground state transition gamma ray peak on the 100 channel spectrum plots. In this way it was possible to determine gain changes with an accuracy of $\pm 1/5$ channel at channel 80, and thus accurately to fix the channels to be summed over in each spectrum. The bias level changes mentioned in Section II-C were not observed here since the length of each run (always less than 15 minutes) was too short.

A more serious correction was applied to the spectra in the gamma energy range from 4.5 to 6.2 Mev (channels 41 through 57 in Figure 28). The majority of the pulses observed in the resonance spectrum in this region can be attributed to the increased yield of ground state gamma rays. However, 15 percent of the pulses in this region cannot be so attributed. Most of these extra pulses are caused by the simultaneous detection of two gamma rays. The gamma rays concerned are the high

energy members and one or the other of the low energy members of the three step cascade through the 3.95 Mev and 2.31 Mev states. The peaks generated in the energy range from 4.5 to 6.2 Mev by this process account for 80 percent of the extra pulses, and obscure any weak radiation from the 7.97 Mev state to the 2.31 Mev state, from the 5.10 Mev state to the ground state, or from the 5.68 Mev state to the ground state.

Another correction whose magnitude was even less well known was that due to Compton electrons produced in the target backing. Gamma rays that undergo Compton scattering in the tantalum target backing do not reach the NaI(Tl) crystal and thus reduce the counting rates. This effect can be corrected for since the backing thickness as well as the scattering coefficient is known. However, the electrons produced by this Compton scattering process can enter the crystal and give pulses indistinguishable from those produced by incident gamma rays. The spectrum and number of these electrons was determined by comparing spectra taken at $+90^{\circ}$ and -90° with respect to the beam without moving the target. At $+90^{\circ}$ the gamma rays passed through the target backing while at -90° they did not. The comparison between these spectra, after gain change and the gamma absorbtion corrections were made, showed up certain small but detectable differences. The spectra above channel 55 (Figure 28) were identical within the experimental errors. Between channel 55 and channel 45 there was a 3 percent increase in the number of counts in the $+90^{\circ}$ spectrum as compared to the -90° spectrum. Since the target was at an angle of 45° to the beam for these measurements, data taken at $+90^{\circ}$ represented gamma rays that had passed through $\sqrt{2}$ times the target thickness. Assuming the number of secondary electrons reaching the counter is proportional to the number of Compton scattered

gammas in the target backing, the electron corrections would be 2 percent at 45^{o} and again 3 percent at 0^{o}.

4. The Angular Distribution Measurements

The angular distribution data is plotted in Figure 29 for the ground state radiation. Both the resonant and non-resonant data are shown. The non-resonant data was taken at 447 kev, just below the resonant energy. Before subtracting the isotropic non-resonant contribution from the total gamma ray intensity at resonance, the non-resonant contribution was corrected to correspond to the beam energy used in taking the resonant data. This correction factor, which varied from 1.053 to 1.166, was simply the ratio of the cross sections of the tail of the 555 resonance calculated at the appropriate beam energies used.

The angular distribution of the gamma rays produced by the transition to the 3.95 Mev state is shown in Figure 30. There are several additional sources of error in this data that were not present in the ground state radiation data. These are principally the uncertainties in the large subtractions that were made from the initial sums taken over channels 25 through 43. The extrapolated tail of the ground state radiation is the largest subtraction (Figure 28). This extrapolation is uncertain because the amount of summing radiation and contributions from secondary electrons are not accurately known. Since the ground state radiation is strongly anisotropic this error will change with angle. The uncertainty in calculating the corrections to the non-resonant radiation in this energy range is not so serious since here the ground state radiation is isotropic.

Because the 448-kev resonance is superposed on a background caused by the low energy tail of the 555 kev resonance, the existance of odd-order

Legendre polynomial terms was suspected. The presence of odd-order terms would immediately determine the parity of the 448 kev resonance as opposite to that of the 555 kev state. Spectra were thus taken both at the resonance and below it at angles symmetrically distributed about 90^{o}. The presence of odd order Legendre polynomials in the distribution would show up as differences between the counting rates at $90^{o} + \theta$ and $90^{o} - \theta$. The comparison between data taken at 75^{o} and 105^{o} and between data taken at 60^{o} and 120^{o} failed to reveal any asymmetry around 90^{o} within the experimental error of ±1.5 percent. Therefore, the angular distributions were finally analyzed in terms of even-order Legendre polynomials.

A preliminary investigation of the angular distribution of the ground state gamma rays indicated that most of the anisotropy could be accounted for by a $\cos^{2}\theta$ term. This was shown by plotting the gamma ray counts against $\cos^{2}\theta$ and obtaining a straight line (Figures 29 and 30). (A $\cos^{4}\theta$ term would show up as a parabola on this plot.) For this reason data was taken at 0^{o}, 30^{o}, 45^{o}, 60^{o}, and 90^{o}, since these points are equally spaced on a $\cos^{2}\theta$ scale. A least squares fit was obtained using the method described by Rose (1953). (Since this method seems to be not generally well known, it has been presented in Appendix C.) In this calculation a constant weighting factor of unity was used throughout. The determinants used to obtain the angular distribution coefficients for fits of both P_0 and P_2 as well as P_0, P_2, and P_4 are given in Table IV for the five angles at which the data was taken. The resulting coefficients were then corrected for the finite solid angle subtended by the crystal. This finite size tends to smooth out the distribution so that each coefficient must be divided by a number less than unity to get the coefficient for a zero solid angle counter. This effect, studied by Rose (1953), leads to calculations

involving numerical integration. The integrals depend on the dimensions of the crystal, its distance from the source (target) and, in general, on the gamma ray energy. For the experimental arrangement used here, with the crystal 8.25 cm from the target, this factor is 0.840 for the $P_2(\cos\theta)$ term and 0.536 for the $P_4(\cos\theta)$ term. The factor for $P_1(\cos\theta)$, which was of interest when the possible existence of interference terms was being investigated, is 0.945. For this experiment, the coefficients are the same for both the ground state radiation and the radiation leading to the 3.95 Mev state. The values for the final angular distributions after all corrections have been made are given in Table V. The errors quoted in this table were obtained by using the matrix in Table IV, and are based on internal errors only.

5. Gamma Ray Widths

In Table VI the resonant gamma ray yields and widths are given. The yields were obtained by integrating the angular distributions; this integration, $\int \sum a_n P_n(\cos\theta)\, d\Omega$, gives a_o as a result, since all other terms vanish. The principal errors in the yield originate in uncertainties in the extrapolated tail of the gamma ray spectrum and in the efficiency of the counter. Statistical errors and errors in the current integration are negligible compared to these. The difficulties described in Section 3 above in calculating the various contributions to the gamma ray spectrum in the region between channel 41 and channel 58 allow only an upper limit to be placed upon the intensity of any radiation in the 4.3 to 6.5 Mev range.

B. The Spin and Parity Assignment

1. Introduction

The magnitude of the radiative widths of Table VI indicates that the transitions to the 1^+ ground state and 1^+ second excited state are dipole

or quadrupole transitions. Therefore the possible values of the spin of the 7.97 Mev level are $J \leq 3$. The fact that anisotropic radiation is observed shows that $J \neq 0$. Gamma-ray angular distributions have been calculated for the remaining spin assignments. For each angular distribution there are at least two unknown parameters. One of these is the ratio of quadrupole to dipole radiation or octupole to quadrupole radiation. The other may be expressed in different forms. For the 1^+, 2^-, and 3^+ assignments, the second parameter is the channel spin mixture ratio a. For 1^-, 2^+, and 3^-, the second parameter is the ratio, δ, of amplitudes for incoming proton waves, where $\delta = A_{\ell_i}/A_{\ell_j}$, ℓ_i and ℓ_j being the proton orbital angular momenta which can form the compound state. For all values of the two parameters, the angular distributions for $J = 3^+$ or 3^- are inconsistent with the experimental values, as the $P_2(\cos\theta)$ coefficient with $J = 3$ is always positive.

2. The 2^+ Assignment

The expressions for the angular distribution coefficients for the cases $J = 1$ and $J = 2$ are given in Table VII. For $J = 2^+$, the minimum value of the $P_2(\cos\theta)$ coefficient is -0.515, and this is outside the experimental limits for the ground-state gamma-ray angular distribution. Four independent measurements of the ground-state gamma-ray angular distribution gave consistent values for the Legendre polynomial coefficients, each one differing from the extreme value allowed for $J^\pi = 2^+$ by two or three standard deviations. The effect of interference of a 2^+ state with the broad 1^- state at 8.06 Mev excitation will be to introduce odd-order Legendre polynomials only, and will not change the magnitude of the $P_2(\cos\theta)$ coefficient. Therefore it may be concluded that the 2^+ spin and parity assignment cannot explain the observed ground-state gamma-ray

angular distribution. The remaining spin and parity assignments 2^-, 1^+, 1^-) in Table VII, each of which can reproduce the observed angular distributions will now be discussed in order of increasing likelihood.

3. The 1^- Assignment

In this case there are no interference terms due to the presence of the 8.06 Mev level. The ratio of the amplitude of d to s-wave formation of the 7.97 Mev level is D exp(iφ) where D is a real number and relative phase φ is the sum of the relative Coulomb phase shift at E_p = 448 kev (90.0°), the relative hardsphere phase shift (-0.5° for a radius of 4.72 fermi), and the phase shifts from neighboring resonances. The latter resonant phase shifts are expected to be near 0° or 180°, the nearest resonance at 550 kev contributing an s-wave phase shift of 4°. Thus φ is expected to be quite close to ±90°. This is in agreement with the elastic scattering data. The curves of Figure 31 with φ as a parameter show the relation between D and the magnetic quadrupole to electric dipole amplitude ratio δ that must be satisfied in order to reproduce the ground-state gamma-ray angular distribution. For φ = ±90°, the observed ground-state gamma-ray angular distribution cannot be achieved. If one starts at φ = +90°, and gradually increases φ, then at φ = 133° a closed loop appears in the right-hand side of Figure 31 at the point representing equal quadrupole and dipole gamma-ray intensities and 36 percent intensity of d-wave relative to s-wave formation of the level. As φ is further increased, the closed loop expands to reach its maximum area at φ = 180°, then shrinks to disappear again at φ = 227°. The diagram is again blank for φ = 270° and a closed loop reappears in the left-hand side of Figure 5 at φ = -72°. The point of appearance represents equal contributions of

quadrupole and dipole intensities ($\delta = 1$) and an intensity of 14 percent of s-wave relative to d-wave formation. As before, the closed loop expands, reaching its maximum extent for $\phi = 0^{o}$ and disappearing again by the time ϕ reaches 72^{o}. Since both D and δ are expected to be small, in order to minimize both, a relative phase $\phi = 180^{o}$ is needed whereas $\phi = \pm 90^{o}$ is expected. Furthermore, the minimum values of D and δ achieved in this assignment are relatively large (11 percent by intensity of d- to s-wave formation and of quadrupole to dipole decay) compared with our expectations (0.85 percent from the ratio of penetration factors for the former and 10^{-3} percent from the radiative width ratios according to the single particle model (Weisskopf, 1951) for the latter).

Another serious drawback to a 1^{-} assignment of the 7.97 Mev level is that a strong transition might be expected to the 2.31 Mev level and no such strong transition is found. The observed transitions to the ground state and 3.95 Mev level would be electric dipole, inhibited by the isobaric spin selection rule, but the transition to the 2.31 Mev state would be electric dipole with no such inhibition. One would have to rely on a small matrix element to explain the small radiative width to the 2.31 Mev state. This difficulty, combined with the large d to s-wave ratio, the unexpected relative phase, and the large magnetic quadrupole to electric dipole ratio required, serve to eliminate the possibility of the assignment 1^{-}.

4. The 1^{+} Assignment

A positive parity assignment of the 7.97 Mev level leads only to odd-order interference terms in the angular distribution caused by the presence of the broad 1^{-} state and these have been shown experimentally to be negligible. The relevant parameters for a 1^{+} resonance are the fraction of

formation by channel spin 1 ($0 \leqslant a_1^2 \leqslant 1$) and the electric quadrupole to magnetic ripole amplitude ratio δ. Since a_1^2 must be the same for both the ground state transition and the transition to the 3.95-Mev level, the difference in their angular distributions must be ascribed to different δ. The curves of Figure 32 show the relation between δ and a_1^2 for both 8-Mev and 4-Mev gamma-ray transitions. Provided $a_1^2 \approx 1$ or 0, reasonable values of δ may be obtained for the two transitions, with $a_1^2 \approx 1$ being preferred since calculations using the single particle model lead to a value for δ^2 of 0.13 percent.

Warburton and Pinkston, (1960) conclude that the $N^{14}(\alpha, \alpha')N^{14}*$ data implies that the 7.97 Mev levels has T = 0 and is a single particle excitation from the N^{14} ground state. To make such a positive parity state with a single-particle excitation requires that the excited nucleon either be kept in the 1p shell or promoted to the $1f_{7/2}$ or $2p_{3/2}$ shell. The latter two configurations are expected to have a high excitation energy. A 1^+ level can be constructed with a promotion to the $1f_{7/2}$ shell only by breaking up the C^{12} core, and leaving the two $p_{1/2}$ nucleons coupled to spin 1. The $2p_{3/2}$ shell is higher than the $1f_{7/2}$ shell, but construction of a 1^+ state does not require breaking up the C^{12} core. If the excited nucleon stays in the 1p shell, the difficulty arises of explaining why two M1 isobaric spin-forbidden transitions within the configuration are observed (to the ground and 3.95-Mev states) to be much stronger than an M1 isobaric spin-allowed transition within the configuration (to the 2.31-Mev state). In addition, the lowest unidentified 1^+ level of this configuration with zero isobaric spin is expected to be above 10 Mev excitation (Warburton and Pinkston, 1960).

5. The 2^- Assignment

For this spin and parity assignment of the 7.97-Mev state, the relevant parameters are the fraction of formation by channel spin 1 ($0 \leqslant a_1^2 \leqslant 1$) and the magnetic quadrupole to electric dipole amplitude ratio δ (expected to be small). With no further parameters, the minimum value of the $P_2(\cos\theta)$ coefficient is -0.515, which is outside the range of experimental error for the ground state transition. However, interference of a 2^- resonance with the broad 1^- level at 8.06-Mev excitation can lead to changes in the $P_2(\cos\theta)$ angular distribution coefficients. Since the 8.06-Mev level is formed uniquely through channel spin 1, only the channel spin 1 contribution to the 2^- resonance will show interference. Of the eight interference terms actually occurring, only two have been calculated explicitly. The remaining six are small. The relative phases of resonant and background radiation (d to s-wave, $\phi = 90^o$) are such that, when an average is taken over the resonance energy, the two terms expected to be most important are maximized, and four of the expected small terms average out to give a zero interference term. These four terms contain, as a factor, the amplitude ratio of d-wave to s-wave formation of the 8.06 Mev level, known to be small (Warburton, et. al., 1959, and Broude et.al., 1956). The remaining two small terms contain, as a factor, the amplitude ratio of M2 to E1 transitions for the strong E1 transition from the 8.06-Mev level. Therefore they are neglected. In order to reproduce the magnitude of the $P_2(\cos\theta)$ coefficient of the ground state transition, it is necessary that the difference of phase of the non-resonant s-wave background and the non-resonant part of the d-wave phase (d-waves are resonant) be close to 90^o, as expected theoretically. A lower limit of 300 ev is also placed on the proton width of

the resonance, in order to achieve a sufficiently large interference term. The experimentally determined upper limit to the width is 400 ev.

The curves of Figure 33 show the relation between a_1^2 and δ required to account for the 8-Mev and the 4-Mev gamma-ray angular distributions, with the resonance width as a third parameter. The value of δ is expected to be small for both radiations, and a satisfactory portion of the curves, from this point of view, is located near $a_1^2 = 0.4$. On this analysis, the difference in the angular distributions of the 8-Mev and 4-Mev radiation is not caused by different δ but by the interference with the non-resonant background being of opposite sign (and of different magnitude) for the two radiations. The required total width of the resonance, 300 ev $\leqslant \Gamma \leqslant$ 400 ev, is just within the range of detection by present elastic scattering techniques, but preliminary attempts (Hebbard and Vogl, 1960) to detect the expected small elastic scattering anomaly were not successful.

A d-wave proton width of 350 ev at 448-kev proton energy corresponds to approximately 50 percent of $3\hbar^2/Ma^2$, and would imply that the configuration is mainly a C^{13} ground state core plus a d-wave proton. For this configuration, two 2^- states may be constructed. Warburton and Pinkston (1960) identify the 5.10-Mev level as one of these with a $(p_{3/2})^8 p_{1/2} d_{5/2}$ configuration, remarking that another 2^- level is expected between 7 and 11 Mev excitation from coupling a $d_{3/2}$ nucleon to the C^{13} ground state. This $(p_{3/2})^8 p_{1/2} d_{3/2}$ configuration is consistant with the inelastic alpha particle scattering data, which implies a single particle excitation from the N^{14} ground state. The required channel spin ratio ($a_1^2 = 0.4$) implies either pure $d_{5/2}$ incident protons or else $d_{3/2}$ protons with 4 percent by intensity of $d_{5/2}$ protons.

Thus, no inconsistencies appear if a 2^- assignment is made to the 7.97 Mev level. It is felt that, although the assignments 1^- and 1^+ can reproduce the observed angular distributions, the difficulties to which these assignments lead eliminate them effectively from consideration, leaving a unique satisfactory assignment of 2^-.

APPENDIX A

Sample Calculation of the $C^{13}(p, \gamma)$ Yield

This sample calculation will be carried through for the spectrum shown in Figure 12, which was obtained from protons of laboratory energy 205 kev. The run that yielded this spectrum took 1262 seconds; the charge deposited on the target was 0.064 coulombs.

The standard gamma spectrum from the mass one bombardment of C^{13}, which is similar to Figure 19 except for a gain change, was obtained at a proton laboratory bombarding energy of 440 kev. The difference between the energy of the gamma ray from this bombardment and that from the 205 kev bombardment is (13/14) (440-250) kev = 218kev, or, since the analyzer was calibrated for 100 kev/channel, 2.2 channels. A comparison of the two spectra shows a change of just 1.2 channels at channel 74 in the position of the ground state gamma ray. Thus, a particular channel, c, must be multiplied by 1-(2.2-1.2)/74 = 73/74 to give its correct location relative to the standard spectrum.

The two regions containing A plus B and C plus D (see Figure 13) are defined by channels 57.1, 62.4, and 81.3, for a 205 kev bombardment. Because of the gain change, these channels are changed to 57.9, 63.2, and 82.4. In the region 57.1 to 62.4, the background is (4339) (1262)/219915 = 25, and in the region 62.4 to 81.3 it is (2144) (1262)/219915 = 12. The time of the background run was 219915 seconds and 4339 and 2144 were the counts recorded in channels 57.1 to 62.4 and in channels 62.4 to 81.3 respectively. The sum in channels 57.9 to 63.2 on the 205 kev spectrum is 2919; in 63.2 to 82.4 it is 523. Subtracting the background gives: $A + B \equiv x = 511$ and $C + D \equiv y = 2791$. The ratio for $B/D \equiv \alpha$, obtained from a group of spectra

taken at 440 kev proton bombarding energy, was found to be 0.1602 ± 0.0016. The straight line background above channel 54 (see Figure 13) which decreases to zero at channel 82, gave the ratio for $A/C \equiv \beta$ as 0.624. The above values for x, y, α and β can now be used in equation 3.2 to give B + D = 2791 ± 88 counts/0.064 coulomb or 43610 ± 1370 counts/coulomb.

APPENDIX B

Calculation of Nuclear Penetration Factors

The particle (proton) width, Γ_p, (equation 3.8) is written as:

$$\Gamma_p = 2P_\ell \gamma_p^2 = \frac{2kR}{A_\ell^2} \gamma_p^2 \qquad \text{(B. 1)}$$

where

$$R = 1.44 \, (A_o^{1/3} + A_1^{1/3})$$

$$k = \sqrt{\frac{2ME_{CM}}{\hbar^2}} = \left(\frac{M_1 M_2}{M_1 + M_2}\right) \frac{\sqrt{2E_{LAB}}}{\hbar}$$

$$A_\ell^2 = F_\ell^2 + G_\ell^2$$

$$\gamma_p^2 = \frac{\hbar^2}{MR^2} \theta_p^2 = \frac{\hbar^2}{R^2} \left(\frac{M_1 + M_2}{M_1 M_2}\right)^2 \theta_p^2$$

in which

F_ℓ = Regular coulomb wave function

G_ℓ = Irregular coulomb wave function

M_1, M_2 = Masses of two interacting nucleii, and

θ_p^2 = Dimensionless reduced level width.

One defines the quantities:

$$\rho = kR$$

$$\eta = \frac{Z_1 Z_0 e^2}{\hbar v} = \frac{Z_1 Z_0 e^2}{\hbar c} \left(\frac{M_p c^2}{E_{LAB}}\right)^{1/2}$$

which are dimensionless parameters used in solving the wave equation of the coulomb field. This equation, solved approximately using the WKB approximation, yields a proton width of:

$$\Gamma_p = F(E)e^{-2\pi\eta}\gamma_p^2 \qquad \text{(B. 2)}$$

in which the function F(E) is a slowly varying function of the energy, most of the variation having been accounted for by the exp $(-2\pi\eta)$ term.

The function F(E) can be obtained more accurately from other sources, which, for the development described here, are the following three:

1. The published tables of Bloch, et. al., (1948)
2. Computer calculation on the CIT Datatron 220
3. Low energy approximation

1. The tables of Bloch, et. al., give, through several defined intermediate functions, the function F(E) as a function of ρ and η. Since the product $\rho\eta$ must be a fixed constant for any particular reaction double interpolation is necessary to obtain F(E) for a given value of E. However, to obtain a curve of F(E) only single interpolation is required since either η or ρ can be fixed and an interpolation carried through in the remaining quantity.

2. More recently a computer program became available for calculating penetration factors on the CIT Datatron 220 digital computer. This program gives penetration factors with an accuracy of better than 1 percent for energies that are not too low. For the C^{13} + p or C^{12} + p cases this lower energy limit is approximately 200 kev. The quantities of interest printed out are A_ℓ^2 and k, so that F(E) can easily be calculated using equations II-A and II-B.

3. At low energies (small ρ) $F_\ell << G_\ell$ so that $A_\ell^2 \approx 1/G_\ell^2$. An asymptotic expansion of G_ℓ^2 in powers of $1/\eta^2$ can be made (Hull and Breit, 1959). The expansion must be made under the restriction that the product $\rho\eta$ be constant. The result obtained, keeping only terms to order E is

$$F(E) = \frac{\pi}{2} \frac{1 - a_\ell E}{K^2_{2\ell+1}(x)} \tag{B. 3}$$

in which $x = 8\rho\eta$ and $K_n(x)$ is the modified Bessel function of the second kind of order n. The quantity a_ℓ is

$$a_\ell = \frac{1}{3E_R}\left(\frac{1}{\ell+1}\left\{\frac{K_{2\ell+3}(x)}{K_{2\ell+1}(x)}\left[1 - 2\ell(\ell+1)\left(\frac{2}{x}\right)^2\right]-1\right\} + 2\ell(\ell+1)(2\ell+1)\left(\frac{2}{x}\right)^4\right) \tag{B. 4}$$

which, for $\ell = 0$, is

$$a_{\ell=0} = \frac{1}{3E_R}\left[\frac{K_3(x)}{K_1(x)} - 1\right]. \tag{B. 4'}$$

The function F(E) for the C^{13} + p reaction is shown in Figure 34. The smooth curve represents the author's bias in fitting the points obtained from sources 1 and 2 and asymptotic to the linear approximation of equations B. 3 and B. 4'.

APPENDIX C

Least Squares Fitting of Angular Distribution Data

The least squares method used to determine the coefficients of the Legendre polynomial expansion for the angular distribution data of Section VII-B seems to be not generally well known and, therefore, is presented here for completeness. This method was developed by Rose, (1953) who also developed, in the same article, the expressions necessary to correct the coefficients for the effects of the finite solid angle of the gamma ray detectors. This latter effect will not be discussed here.

In general, one attempts to fit a function of the form

$$\mu_i = \mu(\Theta_i) = \sum_\gamma a_\gamma A_{i\gamma} \qquad \text{(C. 1)}$$

in which $A_{i\gamma} = \phi_\gamma (\cos \Theta_i)$ and, in general, ϕ_γ could be taken as P_γ or any other function. The Θ_i are the angles at which the data has been taken and the μ_i are the counting rates at the angles Θ_i. The coefficients a_γ are desired.

We let m be the number of angles at which data is taken and let p be the number of coefficients which one assumes.

It should be noted that the two sides of equation C. 1 are not exactly equal, but that the right side represents the left as closely as possible.

The coefficients a_γ are determined from

$$M = \sum_i w_i (\mu_i - \sum_\gamma a_\gamma A_{i\gamma})^2 = \text{Minimum} \qquad \text{(C. 2)}$$

in which the w_i are the statistical weights of the data points and the minimum is found by varying the a_γ. Equation C. 2 yields the set of equations:

$$\sum_{i=1}^{m} w_i(\mu_i - \sum_{\gamma=1}^{p} a_\gamma A_{i\gamma})A_{i\beta} = 0 \qquad \text{(C. 3)}$$

If one now turns to matrix notation the subsequent development will be more compactly expressed. First, the pxp matrix C is defined by:

$$C_{\gamma\beta} = \sum_i w_i A_{i\gamma} A_{i\beta} \qquad \text{(C. 4a)}$$

that is:

$$C = \tilde{A}wA \qquad \text{(C. 4b)}$$

Defining the vectors $\underline{a}$ and $\underline{\mu}$ from the elements a_γ and μ_i can write for equation C. 3:

$$C\underline{a} = \tilde{A}w\underline{\mu} \qquad \text{(C. 5)}$$

or

$$\underline{a} = C^{-1}\tilde{A}w\underline{\mu} \qquad \text{(C. 6)}$$

Equation C. 6 can now be used to define the new matrix:

$$B = C^{-1}\tilde{A}w \qquad \text{(C. 7)}$$

By the definition of B it is clear that the normalization of the w_i does not enter into the result of equation C. 6. The matrix B has been calculated for m = 5 and for p = 2 and p = 3 in which the ϕ_γ used were Legendre polynomials. These matrices were calculated on the assumption of equal weights w_i for all i and are given in Table IV.

Error Analysis:

From equations C. 6 and C. 7 one obtains

$$\underline{a} = B\underline{\mu}$$

or, in detail,

$$a_\gamma = \sum_i B_{\gamma i}\mu_i \tag{C. 8}$$

The uncertainty in a_γ, δa_γ, is easily obtained from equation C. 8 as:

$$\delta a_\gamma = \sum_i B_{\gamma i}\delta\mu_i$$

which, since the $\delta\mu_i$ are independent variables, gives for the mean square deviation of a_γ:

$$\sigma^2(a_\gamma) = \sum_i B_{\gamma i}^2\sigma^2(\mu_i) \tag{C. 9}$$

This mean square deviation is a measure of the deviations to be expected in the coefficients a_γ on purely statistical grounds. In any actual experiment other sources of error may well exist. A clue to their existence can be found in a comparison between the mean square deviation given by C. 9 and the mean square error which is defined below. The mean square error is based on a comparison between the real coefficients a_γ^o and the coefficients a_γ defined by equation C. 8.

Rose shows that this mean square error in a_γ is given by:

$$\langle(a_\gamma - a_\gamma^o)^2\rangle_{Av} = \epsilon^2 C_{\gamma\gamma}^{-1} \tag{c. 10}$$

where

$$\epsilon^2 = \frac{M}{m - p} \tag{C. 10a}$$

and

$$C_{\gamma\gamma}^{-1} = \frac{B_{\gamma i}^{2}}{w_i} \qquad \text{(C.10b)}$$

The value of M in equation C. 10a is obtained from equation C. 2 and in both equation C. 9 and equation C. 10b the squared quantity is the square of the matrix element.

The weights w_i are typically taken as $w_i = 1/\sigma^2(\mu_i)$, which gives for equation C. 10:

$$\langle (a_\gamma - a_\gamma^{o})^2 \rangle_{AV} = \epsilon^2 \sum_i B_{\gamma i}^{2} \sigma^2(\mu_i) \qquad \text{(C. 10')}$$

Equation C. 10' can now be directly compared with equation C. 9. Since all sources of error have been included in C. 10' a comparison of C. 10' with C. 9 will serve to indicate the importance of non-statistical errors. A value of ϵ^2 much greater than unity indicates that there are errors present in the data other than those due to the finite number of counts, or that the value of p chosen was too small. On the other hand, a value of ϵ^2 much less than unity indicates that a smaller value of p might well be used to fit the data.

REFERENCES

F. Ajzenberg-Selove and T. Lauritsen, 1959, Nuclear Physics 11, 1.

C. L. Bailey and W. R. Stratton, 1950, Phys. Rev. 77, 194

R. E. Benenson, 1953, Phys. Rev. 90, 420

R. D. Bent, T. W. Bonner, and R. F. Sippel, 1955, Phys. Rev. 98, 1237

C. Broude, L. L. Green, J. J. Singh and J. C. Willmott, 1957, Phil. Mag. 2, 1006

R. E. Brown, 1963, Ap. J., 137, 338

E. M. Burbidge, G. R. Burbidge, W. A. Fowler, and F. Hoyle, 1957, Revs. Modern Phys. 29, 547

E. J. Burge and D. J. Prowse, Phil. Mag. 1, 912

G. R. Caughlan and W. A. Fowler, 1962, Ap. J., 136, 453

R. F. Christy, 1956, Physica 22, 1009

D. D. Clayton, 1962, Phys. Rev., 128, 2254

J. L. Climenhaga, 1960, Pub. Dom. Ap. Obs. Victoria, 11, 309

H. E. Gove, 1959, "Resonance Reactions, Experimental," in P. M. Endt and M. Demeur, Editors, Nuclear Reactions (Interscience Inc., New York), Chap. VI, p. 293

K. I. Greisen, 1943, Phys. Rev. 63, 323

R. N. Hall and W. A. Fowler, 1950, Phys. Rev. 77, 197

D. F. Hebbard and J. L. Vogl, 1960, Nuclear Physics, 21, 652

R. E. Hester and W. A. S. Lamb, 1961, Phys. Rev. 121, 584

J. Humblet and L. Rosenfeld, 1961, Nuclear Physics 26, 529

S. E. Hunt and W. M. Jones, 1953, Phys. Rev. 89, 1283

H. L. Jackson and A. I. Galonsky, 1953, Phys. Rev. 89, 370

W. A. S. Lamb and R. E. Hester, 1957, Phys. Rev. 107, 550

A. M. Lane and R. G. Thomas, 1958, Rev. Mod. Phys. 30, 257

D. W. Miller, B. M. Carmichael, U. C. Gupta, V. K. Rasmussen and M. B. Sampson, 1956, Phys. Rev. 101, 740

E. A. Milne, 1954, Phys. Rev. 93, 762

A. H. Morrish, 1949, Phys. Rev. 76, 1651

M. E. Rose, 1953, Phys. Rev. 91, 610

J. D. Seagrave, 1951, Ph. D. Thesis, California Institute of Technology

R. G. Thomas, 1952, Phys. Rev. 88, 1109

V. Tongiorgi, 1949, Phys. Rev. 76, 517

E. Vogt, 1959, "Resonance Reactions, Theoretical," in P. M. Endt and M. Demeur, Editors, Nuclear Reactions (Interscience Inc., New York), Chap. V, p. 253.

E. K. Warburton, and W. T. Pinkston, 1960, Phys. Rev. 118, 733

V. K. Weisskopf, 1951, Phys. Rev. 83, 1073

W. Whaling, 1958, "The Energy Loss of Charged Particles in Matter," Handbuch der Physik (Springer-Verlag, Berlin), Vol. XXXIV, p. 193

D. H. Wilkinson and S. D. Bloom, 1957, Phil. Mag. 2, 63

H. H. Woodbury, R. B. Day, and A. V. Tollestrup, 1953, Phys. Rev. 92, 1199

E. J. Woodbury and W. A. Fowler, 1952, Phys. Rev. 85, 51

Table I. Tabulation of the $C^{13}(p, \gamma_o)$ cross section as a function of proton bombarding energy in the laboratory system. The indicated percentage errors are relative errors only. These are 1 percent from 522.5 kev through 629 kev and between 1 percent and 2 percent from 295 kev through 517.5 kev and above 629 kev. The absolute error is estimated at 12 percent. This is made up of a 10 percent uncertainty in estimating the fraction of the gamma-ray spectrum used in measuring the yield of gamma rays, a 3 percent uncertainty in target thickness, and a 6 percent uncertainty in the crystal efficiency. Other sources of error are small compared to these.

Table I

$C^{13}(p, \gamma_o)$ Cross Section

Energy (kev)	Cross Section (μb)		Energy (kev)	Cross Section (μb)
92.5	5.11×10^{-4}	±36%	344	2.292
103	4.70×10^{-4}	±33%	352.5	2.532
113	1.31×10^{-3}	±20%	361	3.115
123	2.36×10^{-3}	±13%	369	3.794
133.5	4.78×10^{-3}	±10%	377.5	4.49
144	8.72×10^{-3}	±9%	385.5	5.27
154	0.0124	±8%	394	6.18
164	0.0206	±8%	402	7.28
174.5	0.0294	±7%	410.5	8.58
185	0.0398	±5%	414	9.60
195	0.0633	±4%	418.5	10.00
205.5	0.0876	±3%	424.5	11.82
212	0.115	±5.5%	427	12.07
220.5	0.145	±5%	435	14.71
229	0.178	±4%	439	15.34
237	0.213	±4%	443.5	17.45
245.5	0.279	±3%	445.5	18.66
254	0.302	±4%	460.5	27.94
262	0.416	±3%	466	30.75
270	0.495	±3%	471	35.9
278	0.641	±3%	476	41.5
286.5	0.696	±2%	481	48.3
295	0.843		486	55.1
303	0.995		492	65.9
311.5	1.123		497	81.0
319.5	1.374		502	100.2
324	1.502		507	122.8
328	1.640		512.5	156.8
332	1.806		517.5	187.6
336	1.920		522.5	241.6

Table I

$C^{13}(p, \gamma_o)$ Cross Section (Continued)

Energy (kev)	Cross Section (μb)	Energy (kev)	Cross Section (μb)
527.5	303.	600	184.4
533	413.	605	159.0
538	544.	614	128.1
543	702.	619	117.0
546	778.	624	102.4
549	831.	626	98.9
551	870.	629	90.9
554	895.	634	83.3
556.5	870.	636	81.4
559	814.	639	82.2
561.5	780.	644	72.8
564	701.	646	70.0
567	634.	649.5	67.1
569	571.	655	60.4
572	505.	656.5	59.2
574	453.	660	58.4
577	398.3	665	53.5
579.5	365.0	667	53.4
582	332.7	670	48.5
585	300.9	672	49.1
587	270.1	675	46.2
590	250.4	677	47.4
595	212.4	680	42.3
		682	44.1

Table II. Limit to Unobserved Narrow Resonances in the $C^{13}(p, \gamma)$ Reaction. All widths are in μev.

Table II

Limit to Unobserved Narrow Resonances

Proton Energy (kev)	$(\Gamma_p\Gamma_\gamma/\Gamma)_{max}$ (μev)	Γ_p = 1% of $3\hbar^2/2Ma^2$ = 30 kev				
		$\ell = 0$	1	2	3	4
450	85	1.3×10^9	2.0×10^8	8.0×10^6	1.3×10^5	1.1×10^3
400	50	8.3×10^8	1.2×10^8	4.5×10^6	7.0×10^4	4.1×10^2
350	27	5.3×10^8	7.5×10^7	3.0×10^6	4.0×10^4	1.8×10^2
300	18	2.2×10^8	2.9×10^7	9.2×10^5	1.2×10^4	4.8×10^1
250	6	8.0×10^7	1.0×10^7	3.0×10^5	4.0×10^3	1.5×10^1
200	1.6	2.0×10^7	2.3×10^6	6.1×10^4	6.4×10^2	1.9×10^0
150	.46	2.6×10^6	2.8×10^5	6.5×10^3	5.5×10^1	1.4×10^{-1}
100	.034	8.6×10^4	8.6×10^3	1.7×10^2	1.0×10^0	2.1×10^{-3}

Table III. Tabulation of the $C^{12}(p, \gamma)$ cross section as a function of proton bombarding energy in the laboratory system. The indicated percentage errors are relative errors only.

Table III

$C^{12}(p, \gamma)$ Cross Section

Energy (kev)	Cross Section (μb)		Energy (kev)	Cross Section (μb)	
195.	0.025	±95%	410.5	11.4	±5%
211	0.036	±56%	419	16.4	±5%
228.5	0.081	±38%	427	24.6	±5%
244.5	0.103	±19%	435	40.5	±5%
261	0.196	±13%	440	49.4	±3%
277	0.301	±7%	443.4	67.6	±5%
293.5	0.385	±6%	445	71.0	±3%
295	0.409	±8%	447.7	82.2	±3%
303	0.486	±8%	450	96.0	±3%
310	0.60	±6%	452.8	106.2	±3%
311.5	0.64	±8%	455.3	112.8	±3%
318	0.71	±6%	457.9	124.2	±3%
319.5	0.79	±8%	460.4	130.0	±3%
324	0.81	±8%	463	124.0	±3%
327	0.90	±5%	465.6	118.1	±3%
328	0.90	±7%	468	107.4	±3%
332	1.07	±7%	470.7	94.0	±3%
335	1.11	±4%	475.8	73.8	±3%
336	1.10	±7%	481	52.0	±3%
342	1.40	±6%	486	44.1	±3%
352	1.73	±4%	491	35.5	±3%
359	2.11	±4%	496	26.7	±3%
361	2.14	±6%	501	22.1	±3%
368	2.70	±4%	506.5	18.9	±3%
369	2.66	±6%	512	15.9	±3%
376.5	3.31	±4%	517	13.8	±4%
377.5	3.36	±6%	522	11.6	±4%
386	4.27	±5%	527	10.6	±4%
394	6.10	±5%	532	9.1	±4%
402	8.12	±5%	537	8.4	±4%

Table III

$C^{12}(p, \gamma)$ Cross Section (Continued)

Energy (kev)	Cross Section (μb)		Energy (kev)	Cross Section (μb)	
542	7.1	±4%	593	3.11	±4%
547	6.6	±4%	604	2.77	±4%
552.5	6.1	±4%	614	2.51	±4%
558	5.5	±4%	624	2.44	±4%
563	5.0	±4%	634	1.85	±5%
568	4.7	±4%	645	1.82	±5%
573	4.1	±4%	654.5	1.67	±5%
578	4.0	±4%	665	1.47	±5%
583	3.6	±4%	675	1.45	±5%
588	3.38	±4%	685	1.17	±5%

Table IV. The matrices used to calculate the angular distribution coefficients. The five columns correspond tothe five angles at which data was taken, 0^{o}, 30^{o}, 45^{o}, 60^{o}, and 90^{o}.

The matrix M_4 is used when the coefficients of both P_2 and P_4 are desired, while M_2 is used when only the P_2 coefficient is desired. (See Appendix C.)

Table IV

Angular Distribution Matrices

$$M_4 = \begin{bmatrix} \frac{25}{525} & \frac{75}{525} & \frac{115}{525} & \frac{145}{525} & \frac{165}{525} \\ \frac{232}{735} & \frac{276}{735} & \frac{160}{735} & -\frac{116}{735} & -\frac{552}{735} \\ \frac{640}{1225} & -\frac{320}{1225} & -\frac{640}{1225} & -\frac{320}{1225} & \frac{640}{1225} \end{bmatrix}$$

$$M_2 = \begin{bmatrix} \frac{1}{15} & \frac{2}{15} & \frac{3}{15} & \frac{4}{15} & \frac{5}{15} \\ \frac{8}{15} & \frac{4}{15} & 0 & -\frac{4}{15} & -\frac{8}{15} \end{bmatrix}$$

Table V. The non-resonant distributions from the close neighborhood of the 448-kev resonance were found to isotropic, within experimental error. Neither for resonant nor for non-resonant radiations were any odd-order Legendre polynomial coefficients observed. The tabulated distributions have been corrected for the finite solid angle of the detector.

The angular distribution of gamma rays to the 3.95 Mev state was analyzed only for P_o and P_2 terms. The subtractions necessary to eliminate the ground state radiation make the calculation of a $P_4(\cos \theta)$ term of doubtful value.

Table V. Resonant Gamma-Ray Angular Distributions

7.97-Mev Level to	Angular Distribution
Ground State	$P_o - (0.570 \pm 0.020)\ P_2 - (0.004 \pm 0.03)\ P_4$
3.95-Mev State	$P_o - (0.33 \pm 0.03)\ P_2$

Table VI. The cascades to the 2.31-Mev state, 5.10-Mev state, and 5.68-Mev state may all be weakly resonant at 448-kev proton energy. Only an upper limit to the strength of this cascade radiation can be given.

Table VI

Resonance Gamma Ray Yields and Widths

7.97-Mev Level ⟶	Ground State	39.5 Mev State	Other States
Yield 10^{-12} γ/p (61% C^{13})	9.7 ± 0.5	7.9 ± 0.5	≤ 0.5
$\frac{\omega\Gamma_p\Gamma_\gamma}{\Gamma}$ ev	0.012	0.010	≤ 0.0005

Table VII. For the 2^+ assignment, the amplitude ratio of f to p waves is F exp ($i\xi$).

The expression for the 2^- assignment represents the average over a narrow resonance of the major terms for interfering 2^- and 1^- levels, with a subtraction of the terms referring to a pure 1^- intermediate state. This corresponds exactly with the experimental situation. The relative phase of the s and d-waves has been chosen as described in the text. This maximizes the fourth (i.e. the interference) term in the expression above the $J^\pi = 2^-$. The sign of the fourth term must be chosen negative to fit the ground-state gamma-ray angular distribution. The quantity σ_N refers to the non-resonant cross section in the neighborhood of the resonance, while σ_R is the actual cross section at the peak of the resonance.

Table VII. Theoretical Angular Distributions

Assumed J^{π}	Angular Distribution to a 1^+ Final State
1^+	$P_o + P_2(1/2)(1 - 3a_1^2/2)\left[(1 + 6\delta + \delta^2)/(1 + \delta^2)\right]$
1^-	$P_o + P_2(1/4)\left[(D^2 + 2\sqrt{2}D\cos\phi)/(1 + D^2)\right]$ $\left[(1 + 6\delta + \delta^2)/(1 + \delta^2)\right]$
2^+	$P_o + P_2(-7/20)\left[(1 - 2\sqrt{6}F\cos\xi/7 + 8F^2/7)/(1 + F^2)\right]$ $\times\left[(1 - \delta/\sqrt{5} - 5\delta^2/7)/(1 + \delta^2)\right]$ $+ P_4(8/21)\left[(F^2 - 2\sqrt{6}F\cos\xi)/(1 + F^2)\right]\left[\delta^2/(1 + \delta^2)\right]$
2^-	$P_o + P_2(-1/2)(1 - a_1^2/2)\left[(1 - \delta/\sqrt{5} - 5\delta^2/7)/(1 + \delta^2)\right]$ $+ P_4(8/7)(1 - 5a_1^2/3)\left[\delta^2/(1 + \delta^2)\right]$ $\pm P_2(\sqrt{3/2})(a_1)\left[(1 - \sqrt{5/18}\ \delta)/(1 + \delta^2)\right]\left[\sigma_N/(\sigma_R - \sigma_N)\right]^{1/2}$

Figure 1. Energy level diagram of N^{14}. The notation is standard.

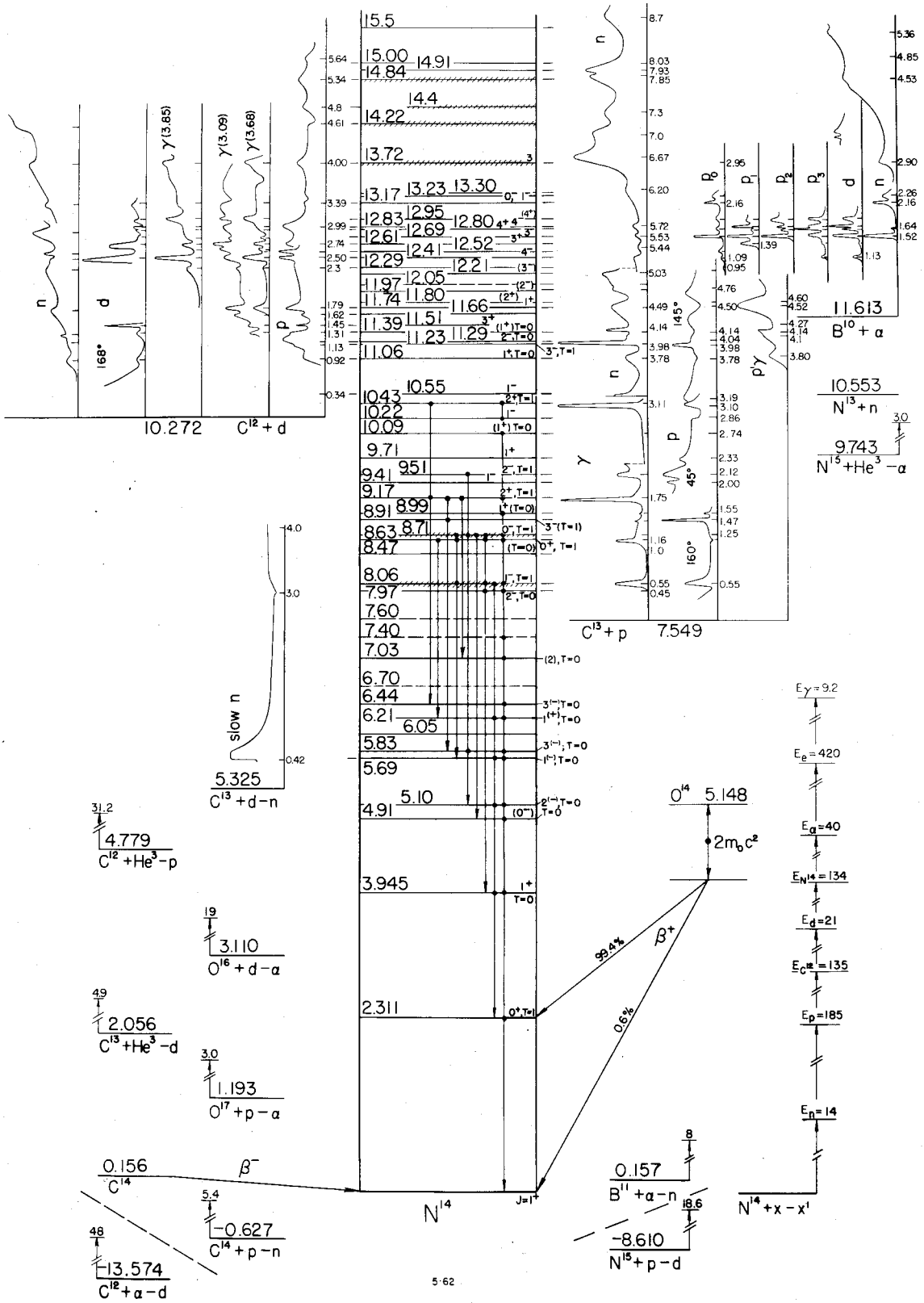
15.5
15.00
14.91
14.84
14.4
14.22
13.72
13.17
13.23
13.30
12.83
12.95
12.80
12.61
12.69
12.52
12.29
12.41
12.21
11.97
12.05
11.74
11.80
11.66
11.39
11.51
11.23
11.29
11.06
10.43
10.55
10.22
10.09
9.71
9.41
9.51
9.17
8.91
8.99
8.63
8.71
8.47
8.06
7.97
7.60
7.40
7.03
6.70
6.44
6.21
6.05
5.83
5.69
4.91
5.10
3.945
2.311
n
d
γ(3.85)
γ(3.09)
γ(3.68)
p
168°
10.272
C12 + d
p
p0
p1
p2
p3
d
n
11.613
B10 + α
10.553
N13 + n
9.743
N15 + He3 − α
γ
p
p'γ
45°
145°
160°
C13 + p
7.549
slow n
5.325
C13 + d − n
4.779
C12 + He3 − p
3.110
O16 + d − α
2.056
C13 + He3 − d
1.193
O17 + p − α
0.156
C14
β−
0.157
B11 + α − n
−8.610
N15 + p − d
−0.627
C14 + p − n
−13.574
C12 + α − d
N14
J=1+
O14
5.148
2mec2
99.4%
β+
0.6%
Eγ=9.2
Ee=420
Eα=40
EN14=134
Ed=21
EC12=135
Ep=185
En=14
N14 + x − x'
5-62

Figure 2. The pyrex apparatus used for making carbon targets by cracking methyl iodide. The tantalum target blank rests on quartz tubing placed in the center tube. This removable center tube, around which the induction coil was wound, was sealed with silicon grease to the vacuum system. The manometer was used to measure the CH_3I vapor pressure.

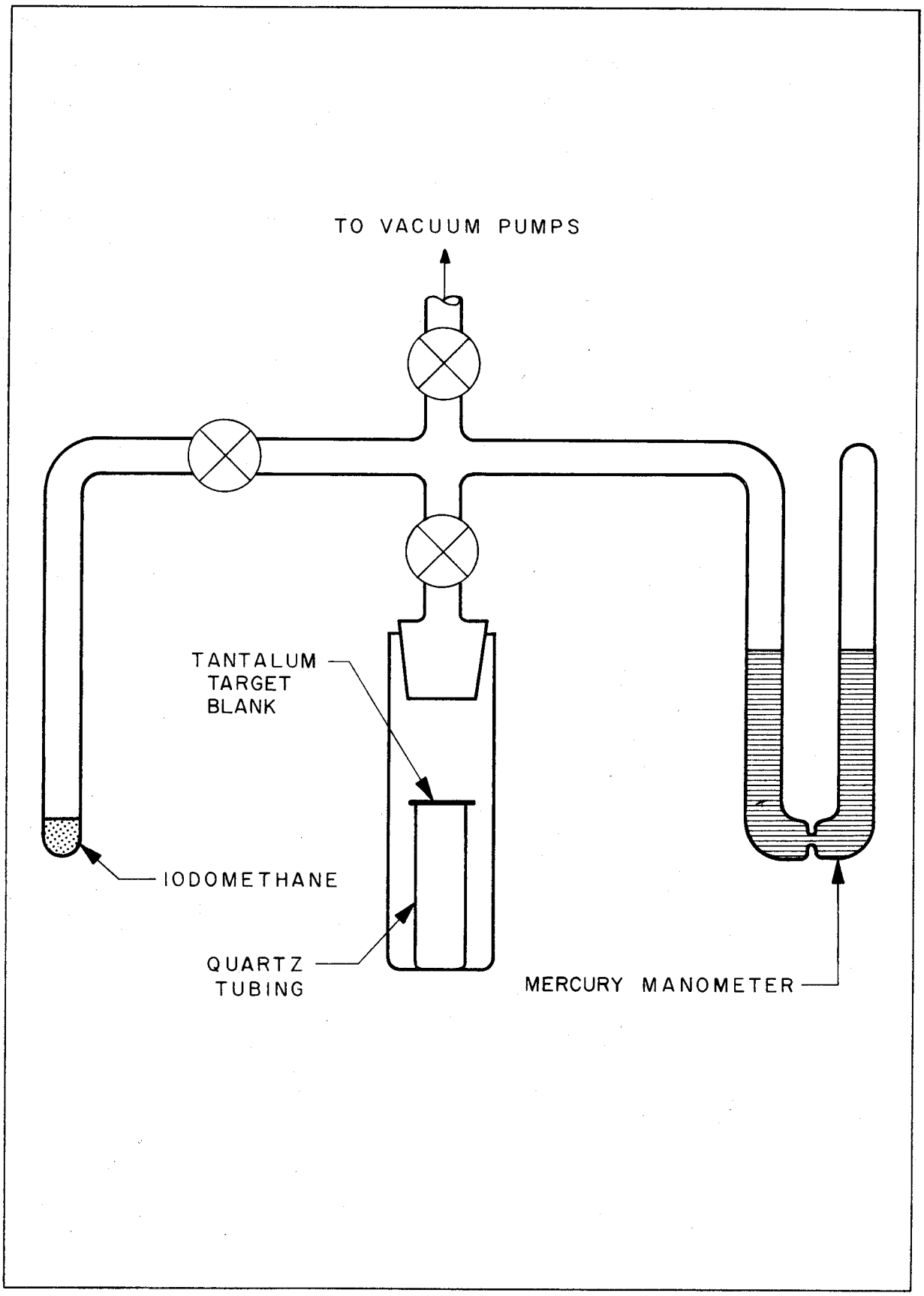
TO VACUUM PUMPS
TANTALUM
TARGET
BLANK
IODOMETHANE
QUARTZ
TUBING
MERCURY MANOMETER

Figure 3. The pyrex target chamber used for measurements above 200 kev proton laboratory bombarding energy. The center rod locates the target along the axis of the cylindrical chamber. The off-center rod, containing the quartz disc, is used for visual observations of the beam spot. When taking data, this disc is lowered out of the path between the target and the gamma detecting crystal.

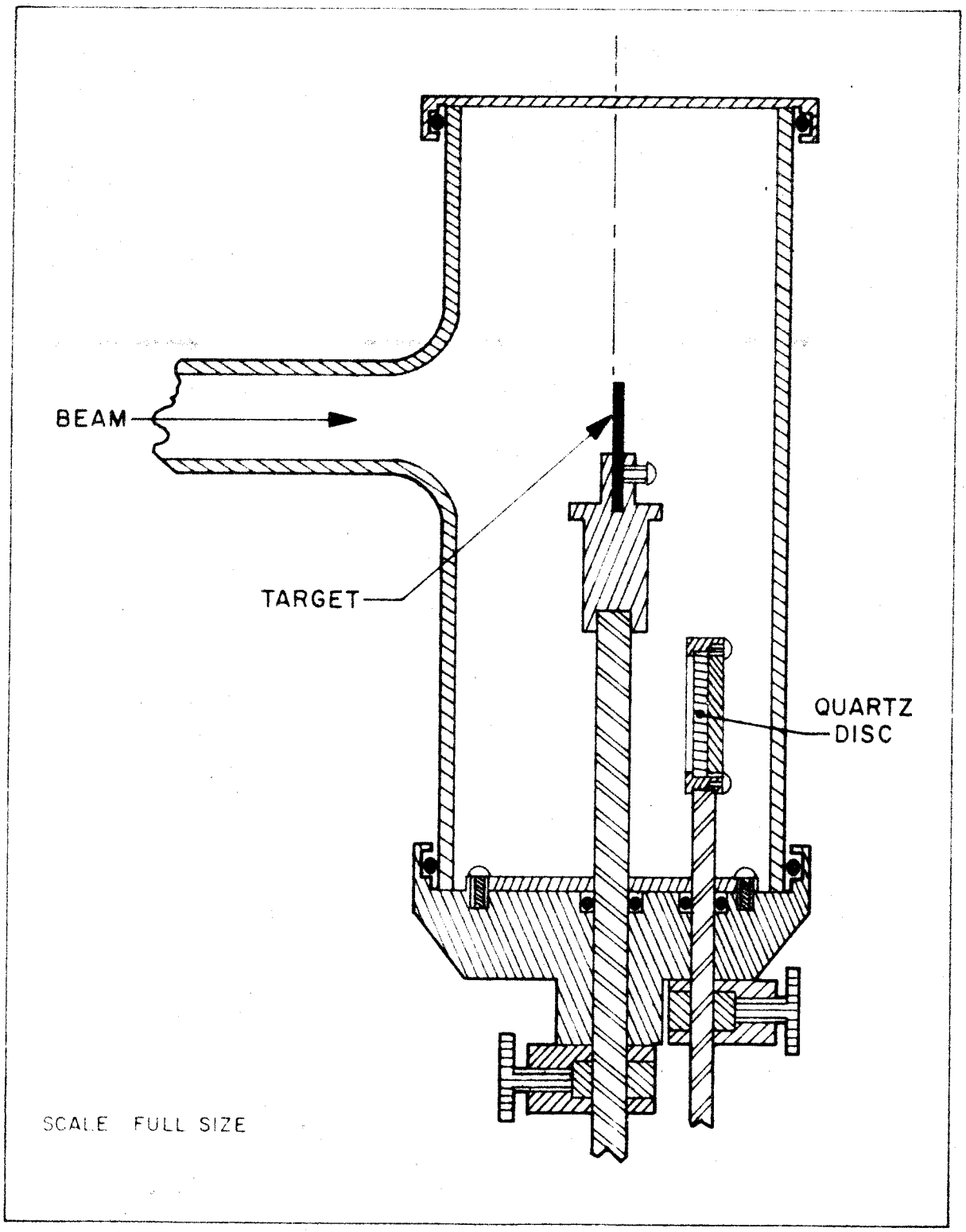
BEAM
TARGET
QUARTZ
DISC
SCALE FULL SIZE

Figure 4. The plastic scintillator used in the anticoincidence shield. The position of the 4" x 4" NaI(T1) crystal inside the shield is shown. The target, placed in the target chamber shown in Figure 9, can be located 6 mm from the crystal.

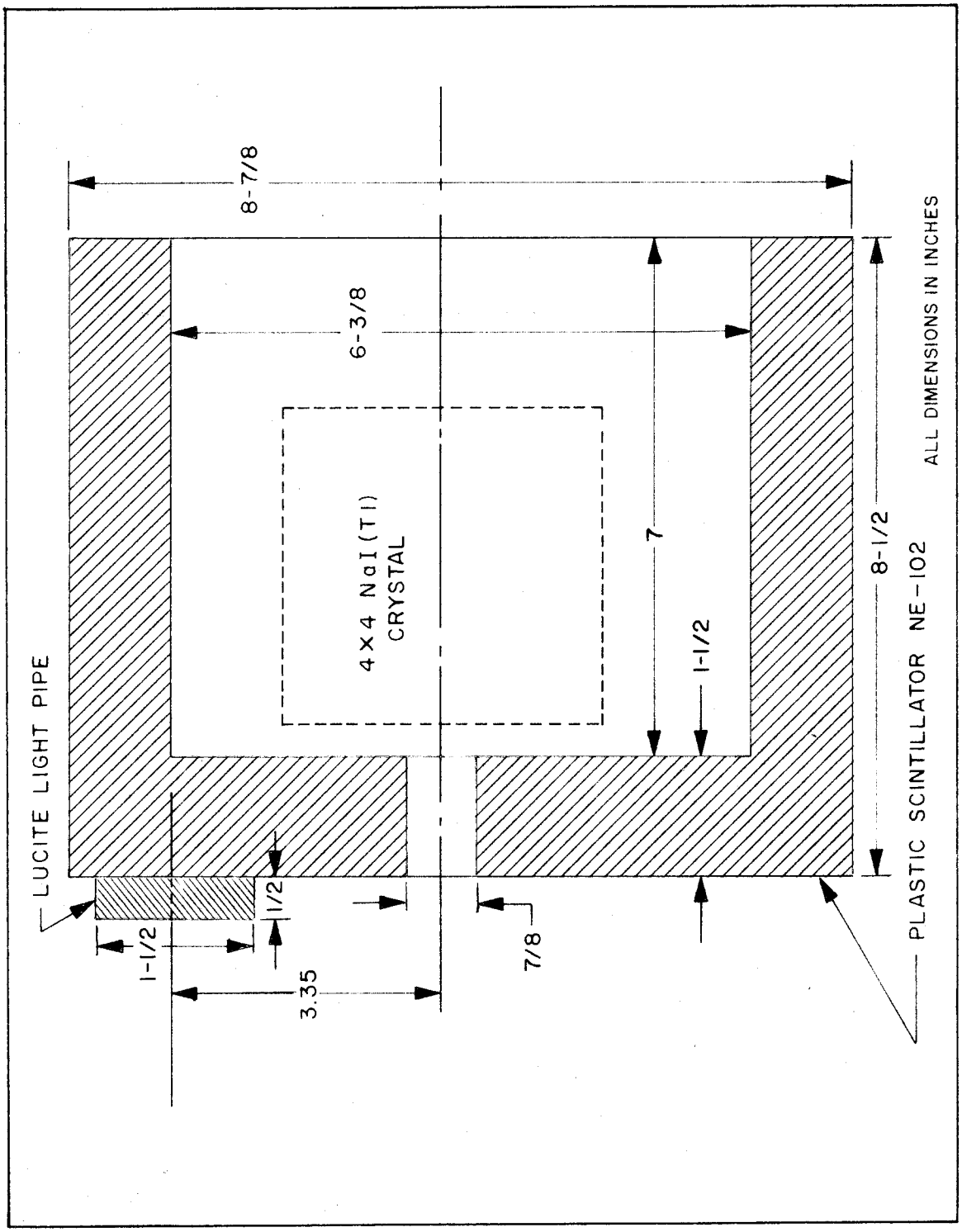
8-7/8
6-3/8
4 x 4 NaI(Tl)
CRYSTAL
7
1-1/2
8-1/2
ALL DIMENSIONS IN INCHES
LUCITE LIGHT PIPE
1/2
1-1/2
3.35
7/8
PLASTIC SCINTILLATOR NE-102

Figure 5. The brass container fabricated to enclose the plastic scintillator shown in Figure 4. The scintillator was held firmly in position by a) the shoulder on the end, which kept the scintillator concentric with the container, and b) the foam rubber compressed against the front surface of the scintillator which kept the scintillator firmly against the back of the container and prevented its horizontal movement within the container. The phototube was held against the light pipe with the indicated set screws. These screws were tightened into the base of the phototube. The "O-Ring" served to center the phototube in its cylindrical container. Light seals were effected by using black electrical tape between the surfaces of all joints that were screwed together.

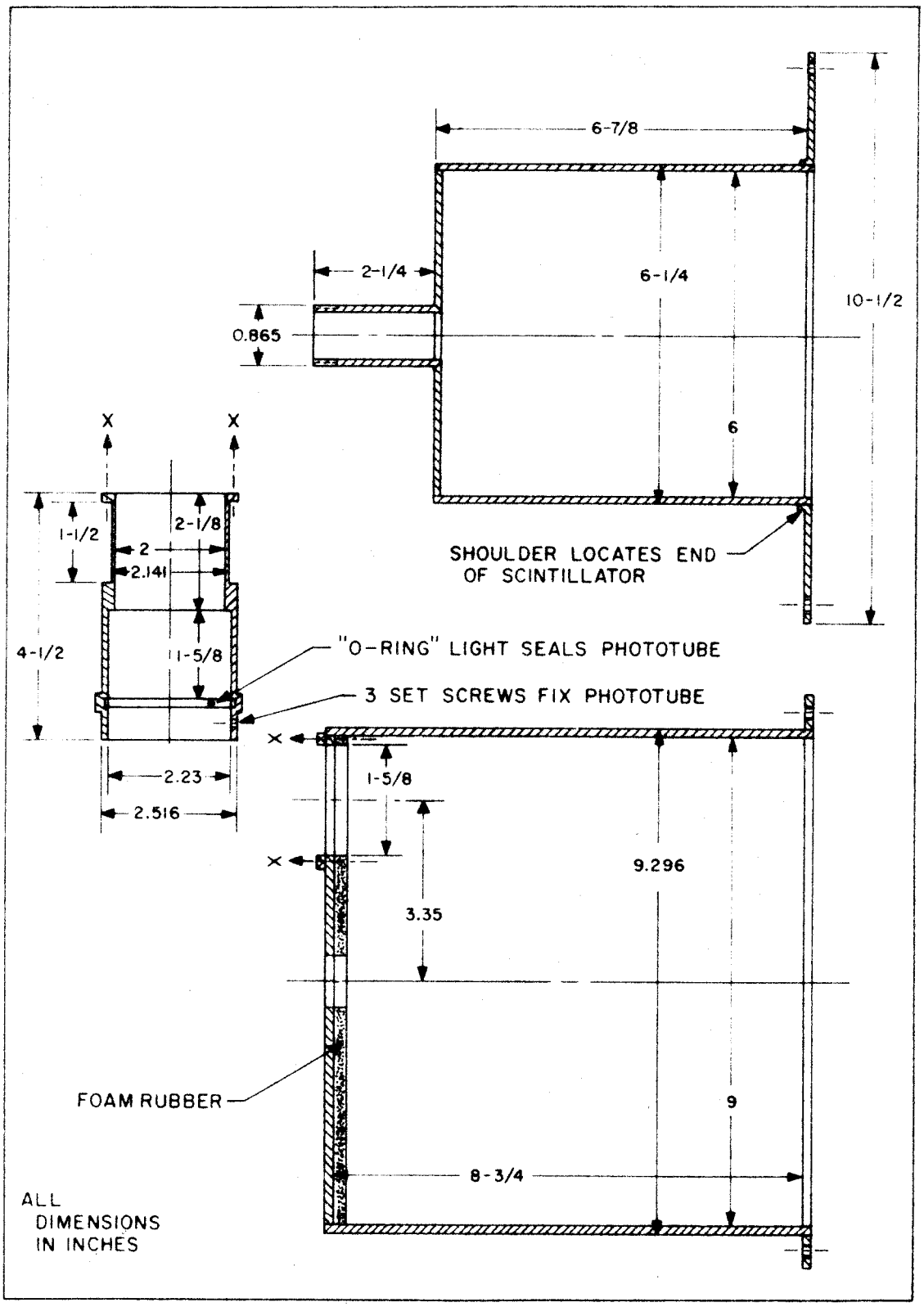
6-7/8
10-1/2
2-1/4
6-1/4
0.865
6
SHOULDER LOCATES END
OF SCINTILLATOR
X
X
1-1/2
2-1/8
2
2.141
4-1/2
1-5/8
"O-RING" LIGHT SEALS PHOTOTUBE
3 SET SCREWS FIX PHOTOTUBE
2.23
2.516
1-5/8
9.296
3.35
FOAM RUBBER
9
8-3/4
ALL
DIMENSIONS
IN INCHES

Figure 6. The anticoincidence circuit used with the scintillator of Figure 4. Both the "NaI" and "SCIN" inputs were positive. Either a positive or negative output pulse of variable amplitude was available.

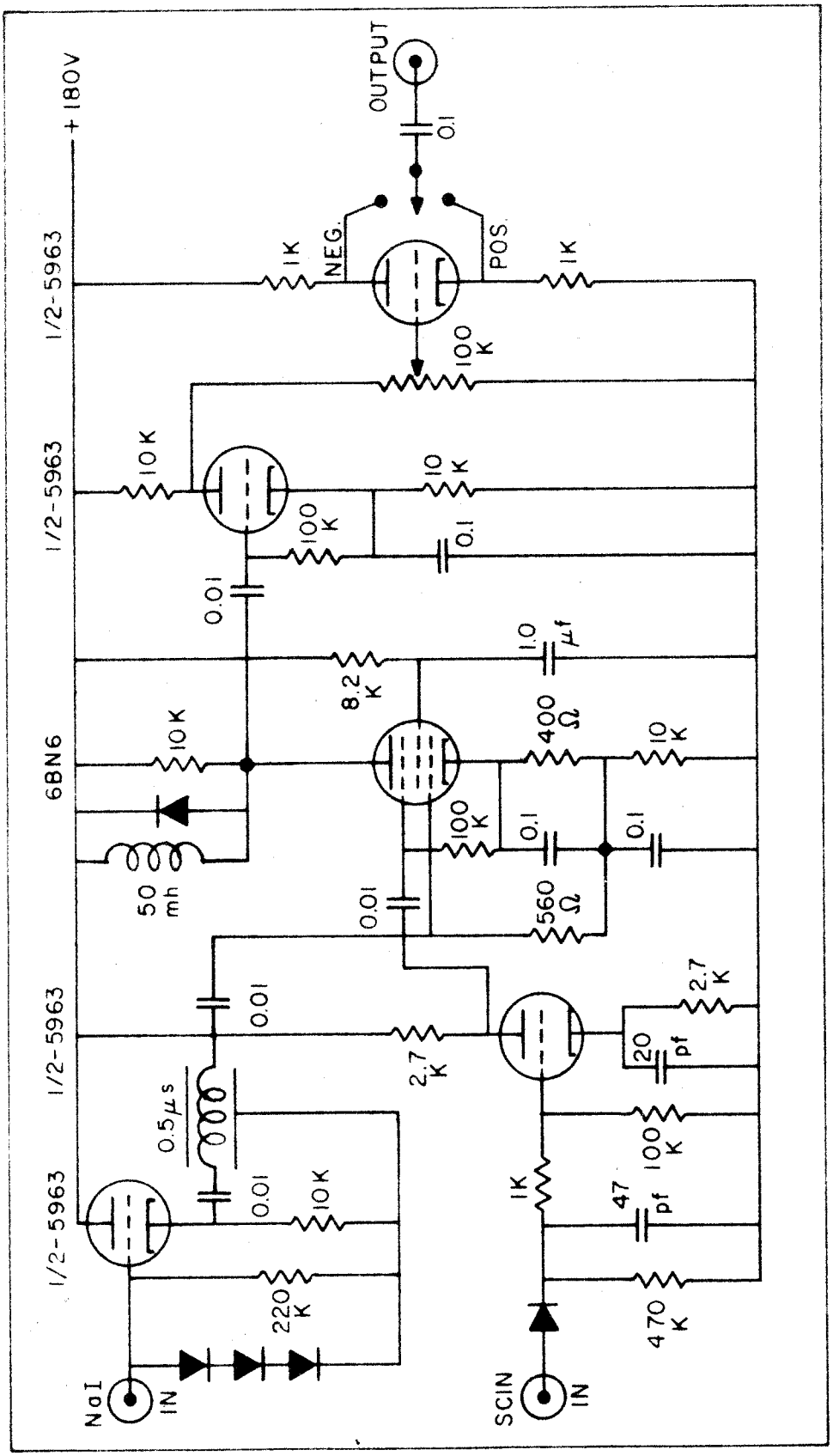
+180V
OUTPUT
0.1
NEG.
POS
1K
1K
1/2-5963
100 K
10 K
10 K
100 K
0.1
0.01
1.0 μf
8.2 K
6BN6
10 K
400 Ω
10 K
100 K
0.1
0.1
50 mh
0.01
560 Ω
2.7 K
0.01
2.7 K
20 pf
0.5μs
1K
100 K
47 pf
0.01
10 K
220 K
470 K
NaI IN
SCIN IN

Figure 7. Background spectra taken with the 4" x 4" NaI(Tl) crystal. The spectra were displayed on a 100 channel analyzer with an energy calibration of 100 kev per channel. The data points plotted represent averages over several channels and the errors are the statistical counting errors only. Included in the figure is the full energy peak of the C^{13} (p, γ) reaction at 440 kev proton bombarding energy and the limits of this peak for defining "D" in equation 3.2 at 90 kev proton bombarding energy. The solid background curve is shown in more detail in Figure 8.

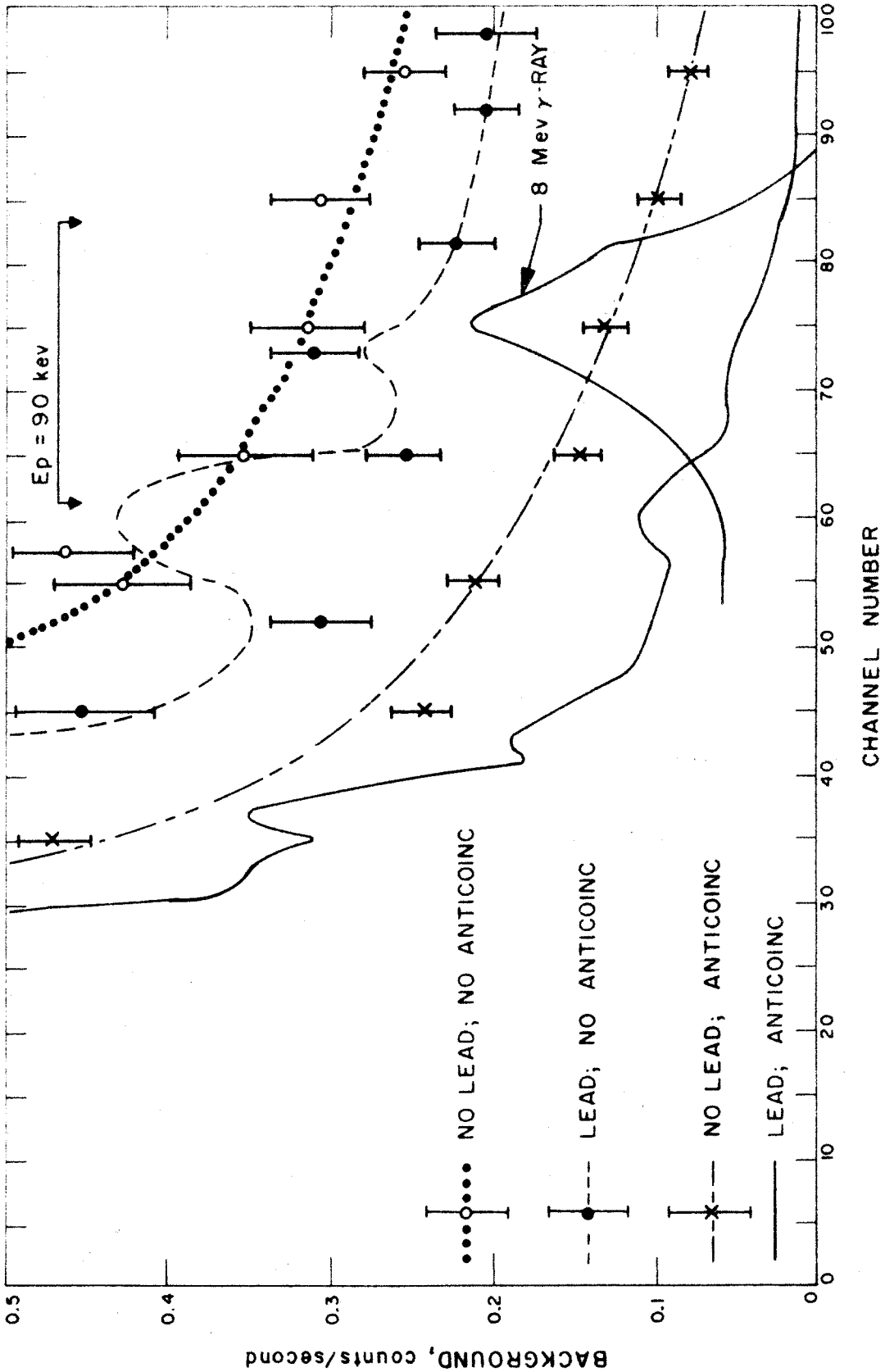
BACKGROUND, counts/second
0.5
0.4
0.3
0.2
0.1
0
CHANNEL NUMBER
0
10
20
30
40
50
60
70
80
90
100
Ep = 90 kev
8 Mev γ-RAY
NO LEAD; NO ANTICOINC
LEAD; NO ANTICOINC
NO LEAD; ANTICOINC
LEAD; ANTICOINC

Figure 8. The background spectrum of the 4" x 4" NaI(Tl) crystal taken with the lead shield and anticoincidence plastic shield in place. The 100 channel analyzer was calibrated for 100 kev per channel. The peak at channel 26 results from the detection of the 2.62 mev gamma rays produced by the decay of environmental thorium C". All the structure at higher energies is caused by cosmic rays. The error bars in the data points are those of counting statistics only. The limits of the ground state gamma peak from the $C^{13}(p, \gamma)$ reaction are shown for two proton bombarding energies. These are the limits of "D" in equation 3.2.

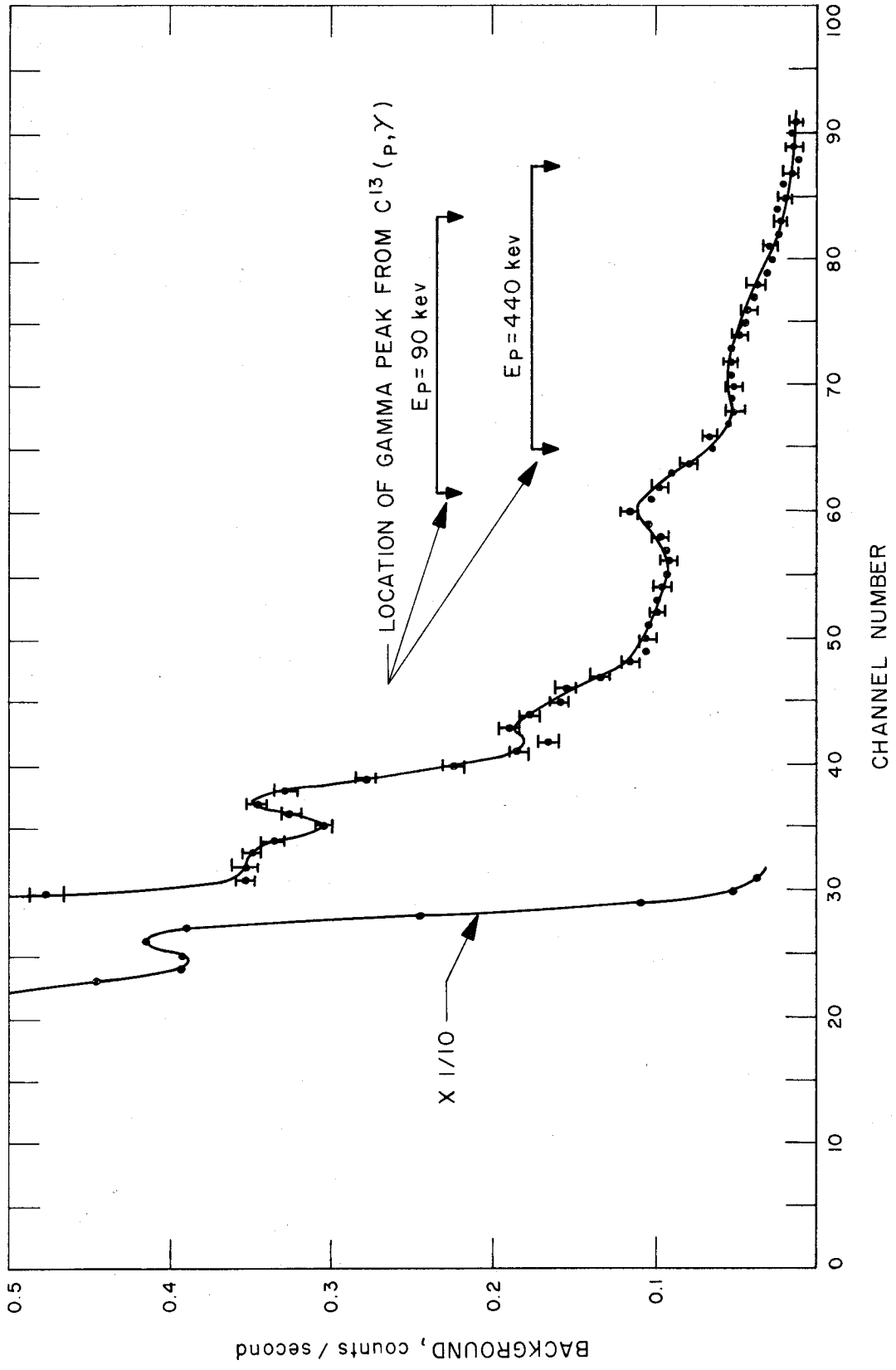
LOCATION OF GAMMA PEAK FROM $C^{13}(p,\gamma)$
E_p= 90 kev
E_p=440 kev
X 1/10
BACKGROUND, counts / second
CHANNEL NUMBER
0.5
0.4
0.3
0.2
0.1
0
10
20
30
40
50
60
70
80
90
100

Figure 9. Modifications to the pyrex target chamber of Figure 3 for use with the anticoincidence shield. The body is identical to the target chamber of Figure 3 enabling the same lid and base to be used for both. The additional tube was designed to allow the target to be located inside the shield. The brass ring was prevented from sliding further into the tube by a slight crimp in the tube. Soldered to this brass ring was a No. 24 copper wire which was used for charge integration and three bent phosphor bronze tabs which kept the target in place and provided a positive electrical contact to it. Between the aluminum cap and the target, a 1/16 inch thick quartz disc was located to serve as an insulator. The copper heat sink was pressed onto the aluminum cap.

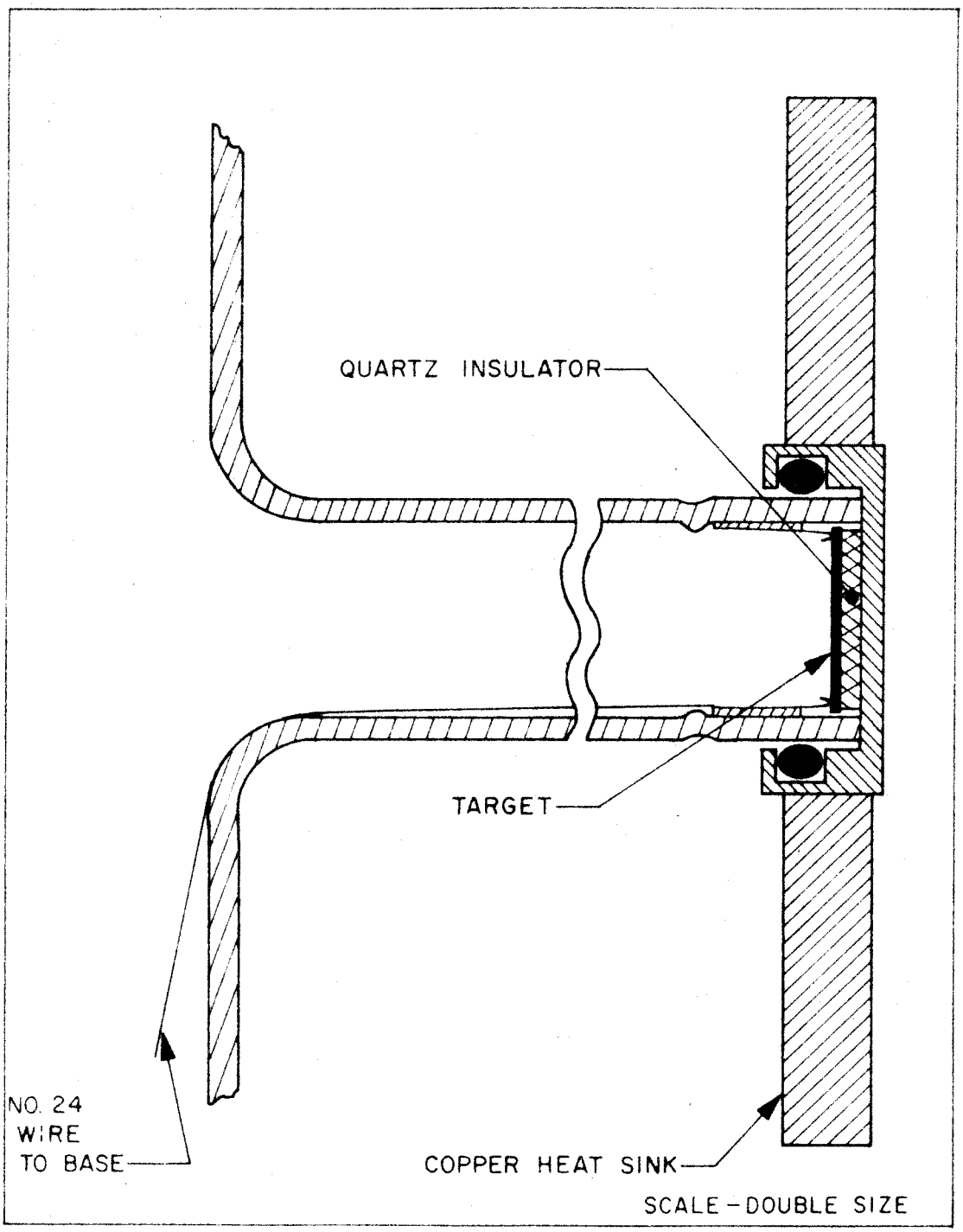
QUARTZ INSULATOR
TARGET
NO. 24
WIRE
TO BASE
COPPER HEAT SINK
SCALE – DOUBLE SIZE

Figure 10. Four gamma ray spectra obtained at the proton bombarding energies indicated. The number in parenthesis in each figure is the total duration of the runs that formed each spectrum. There have been no corrections to the data to obtain these data points. Note that at E_p = 92 kev and E_p = 103 lev there is no visual indication of the presence of the full energy gamma peak. At E_p = 113 kev, the gamma peak is just becoming visible and at 123 kev the peak is quite evident. The energy calibration is 100 kev per channel.

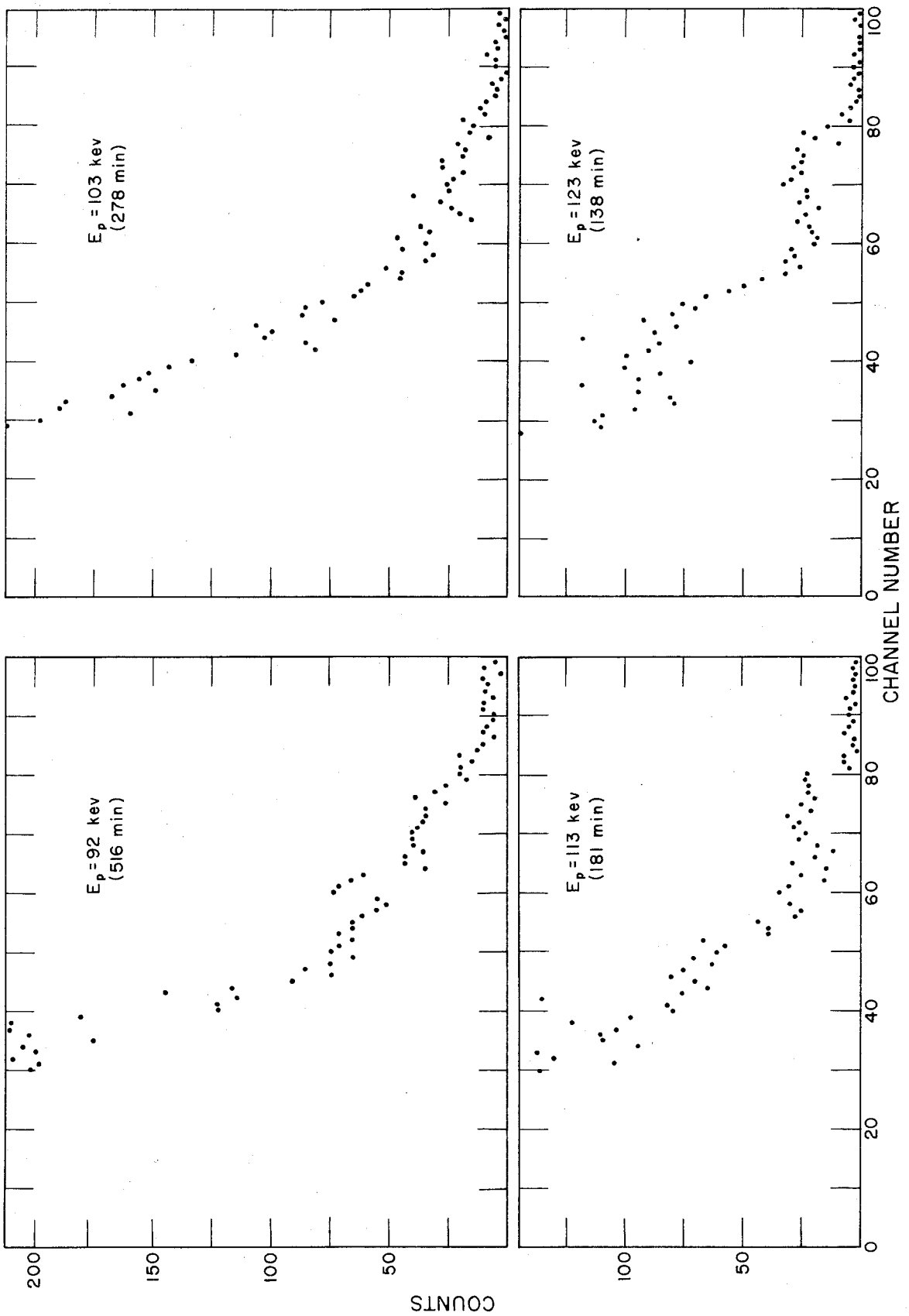
E_p = 103 kev
(278 min)
E_p = 123 kev
(138 min)
E_p = 92 kev
(516 min)
E_p = 113 kev
(181 min)
COUNTS
CHANNEL NUMBER
0
20
40
60
80
100
50
100
150
200

Figure 11. The gamma ray spectrum obtained by bombarding a C^{12} + C^{13} target with deuterons of 400 kev laboratory energy. The 100 channel analyzer was calibrated for 100 kev per channel. The high energy tail, above channel 56, is beam dependent background, i.e., not produced in the target. The peak at channel 46 (4.6 mev) is thought to be from $C^{13}(d,\alpha\gamma)\ B^{11}$.

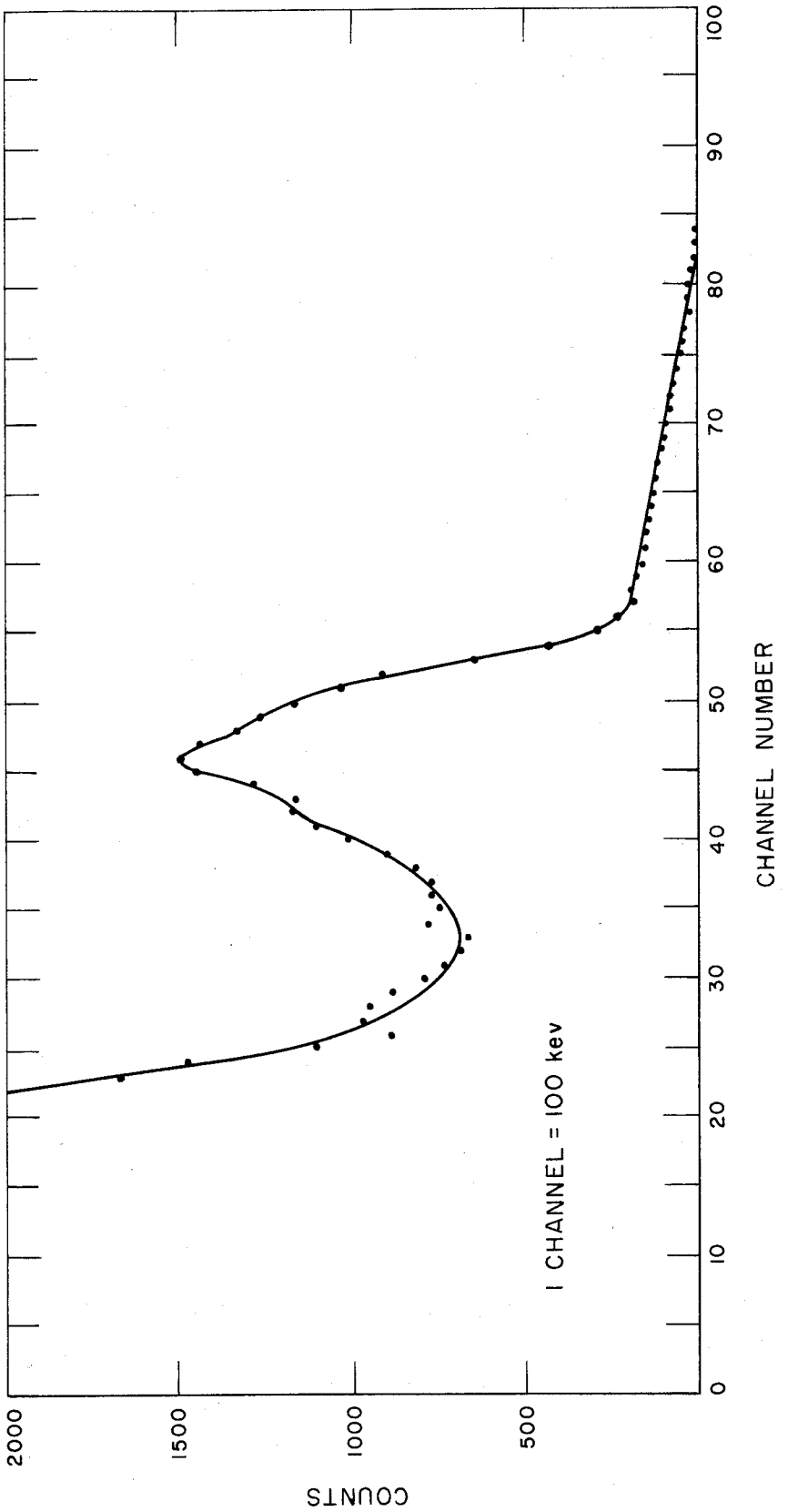
COUNTS
2000
1500
1000
500
0
10
20
30
40
50
60
70
80
90
100
CHANNEL NUMBER
1 CHANNEL = 100 kev

Figure 12. The spectrum obtained by bombarding a $C^{12} + C^{13}$ target with a 400 kev mass two proton beam. The analyzer was calibrated for 100 kev per channel. The peak at channel 46 is produced by the same reaction as the one in Figure 11, i.e., the deuteron component in the mass two beam through the $C^{13}(d, a\gamma)$ reaction. The dashed curve is the ground state gamma ray from the $C^{13}(p, \gamma)$ reaction for 200 kev proton bombarding energy. Time dependent background corrections have not been made in the spectrum, but are small and would not at all change the spectral shape.

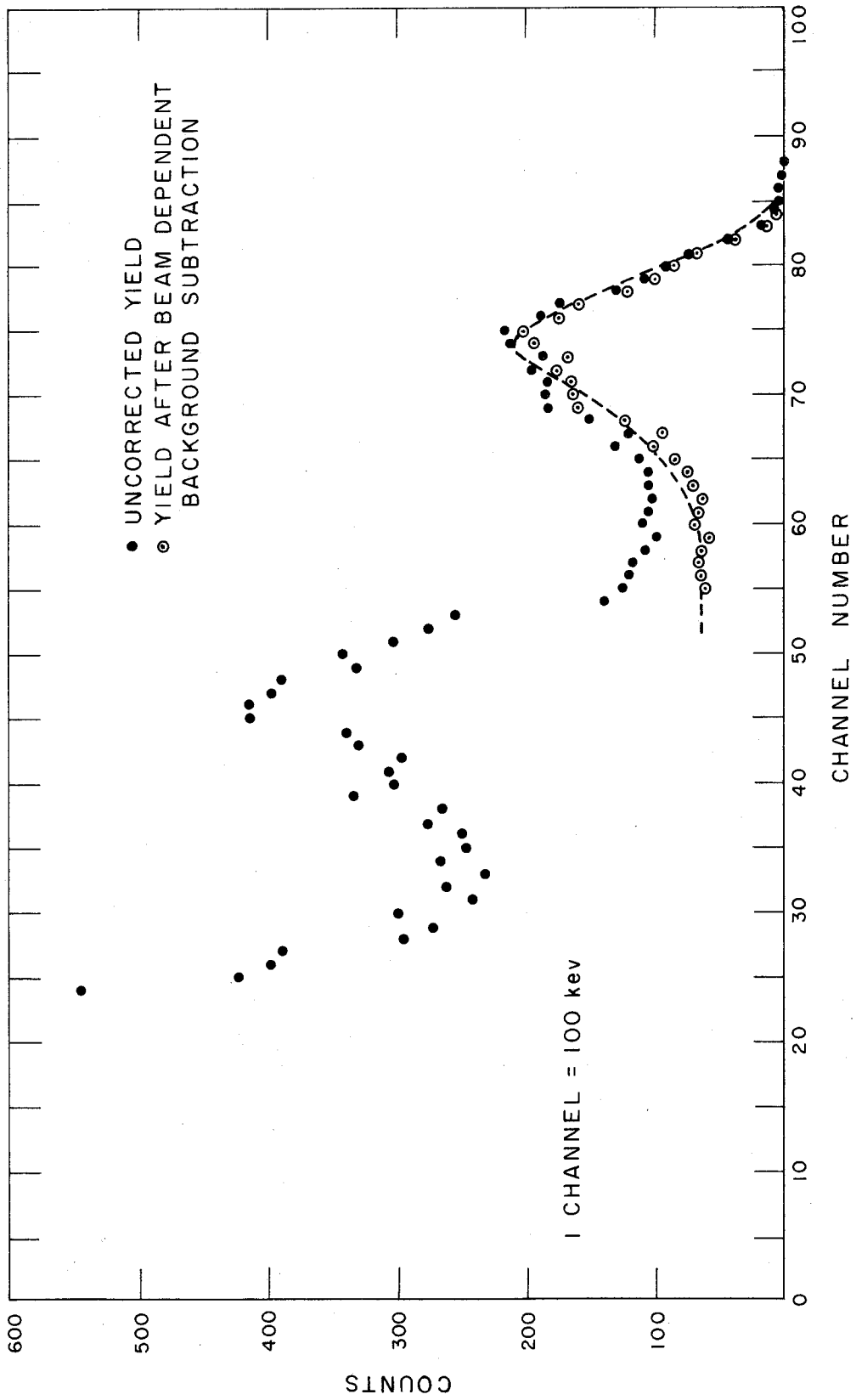
UNCORRECTED YIELD
YIELD AFTER BEAM DEPENDENT BACKGROUND SUBTRACTION
1 CHANNEL = 100 kev
COUNTS
CHANNEL NUMBER
600
500
400
300
200
100
0
10
20
30
40
50
60
70
80
90
100

Figure 13. An idealized (no statistical fluctuations) spectrum obtained from the mass-two bombardment of a $C^{12} + C^{13}$ target. The dashed curve is the deuteron spectrum alone. The regions A, B, C, and D are defined on page 26.

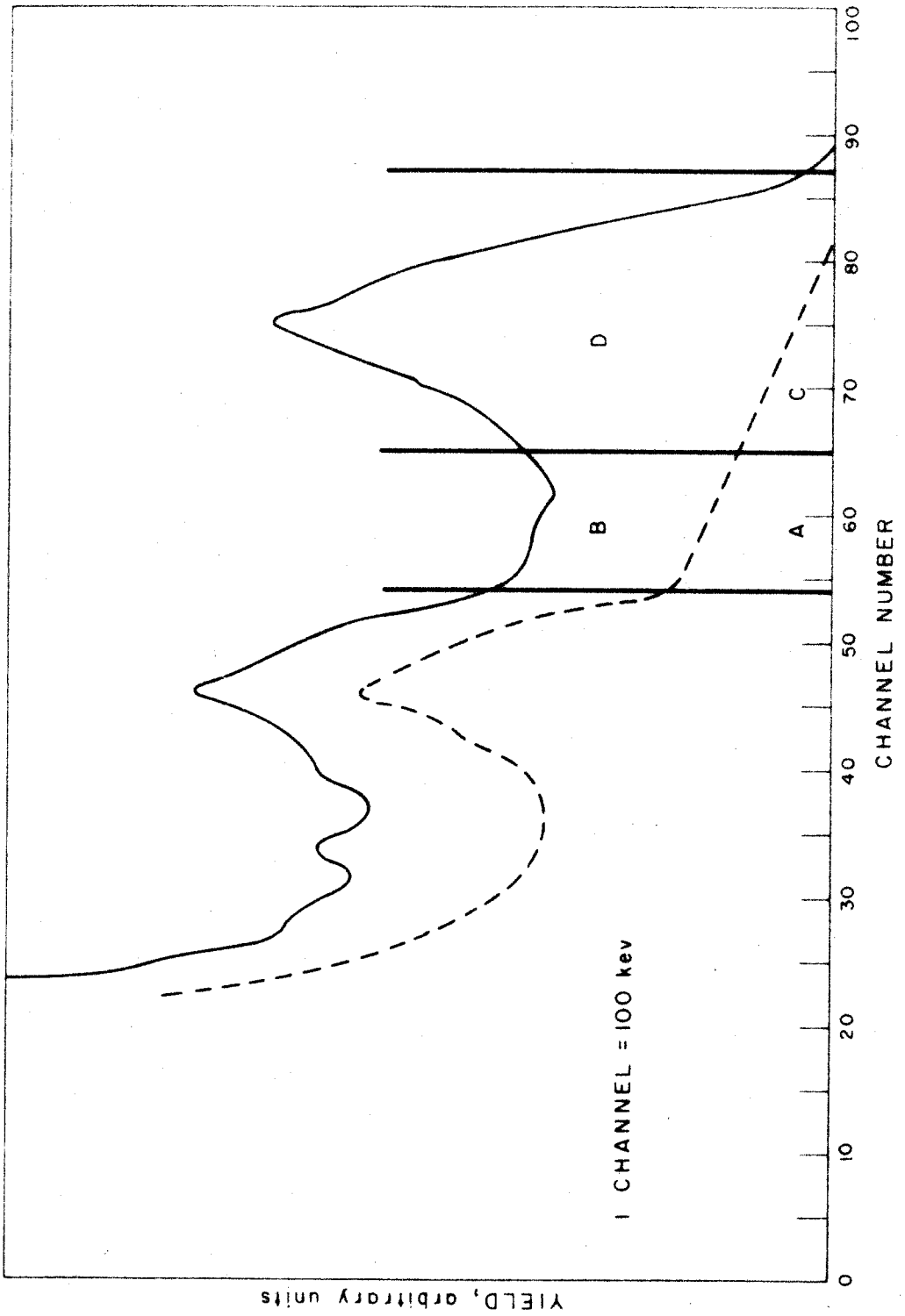
YIELD, arbitrary units
1 CHANNEL = 100 kev
A
B
C
D
0
10
20
30
40
50
60
70
80
90
100
CHANNEL NUMBER

Figure 14. The composite spectrum from the mass-two bombardment of the $C^{12} + C^{13}$ targets at an effective proton bombarding energy of 92.4 kev. The points represent the raw uncorrected data. The crosses represent the data after the time dependent background subtractions have been made. No allowance was made for gain changes in adding the individual spectra together to obtain this composite spectra. The overall running time was 516 minutes, and the error bars are statistical only.

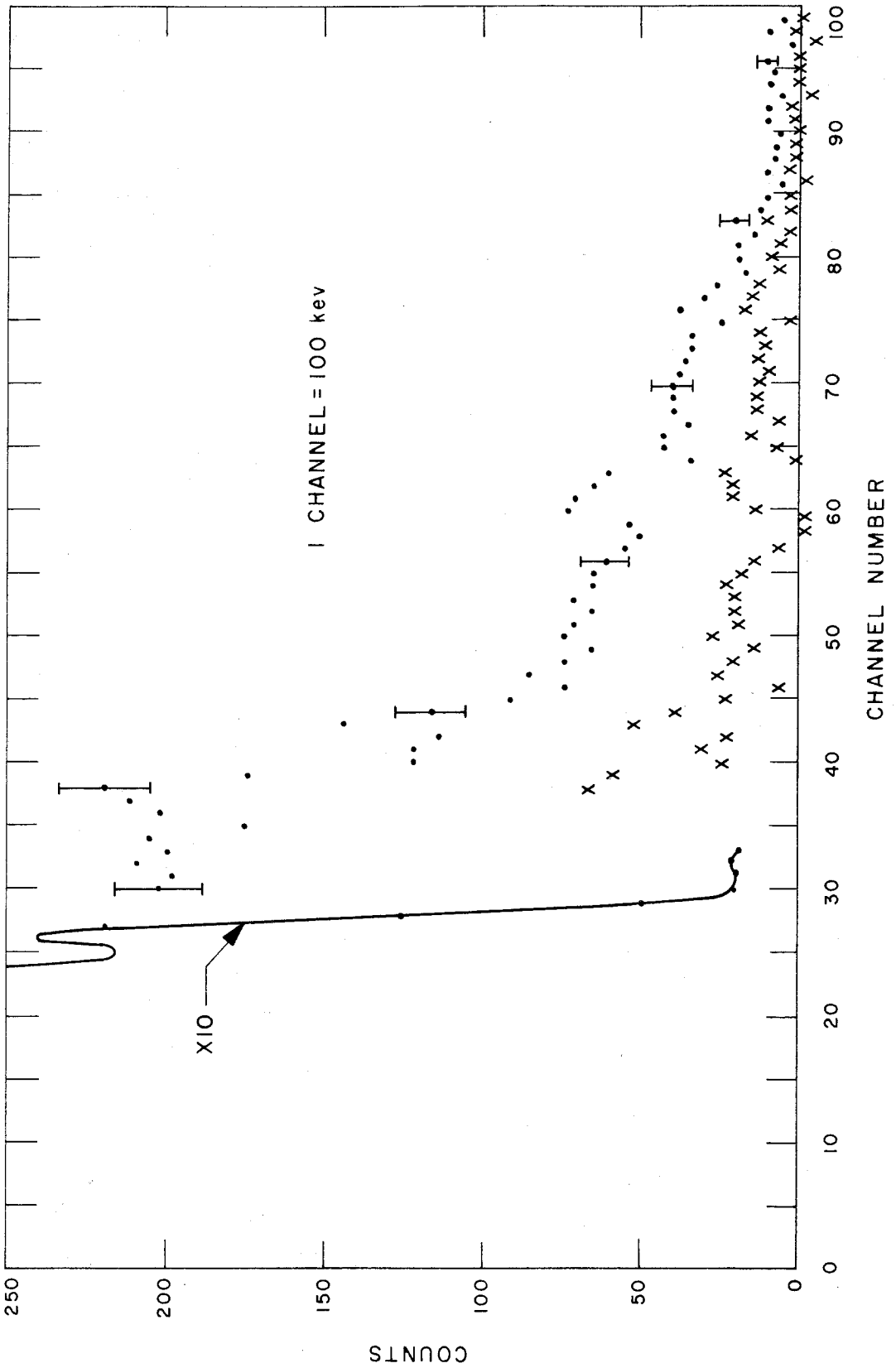
1 CHANNEL = 100 kev
X10
COUNTS
CHANNEL NUMBER
0
50
100
150
200
250
10
20
30
40
50
60
70
80
90
100

Figure 15. Excitation functions of the 448.5 kev resonance for two targets of different thicknesses. All gamma pulses of energies above 5 Mev are recorded. The dashed lines refer to the underlying non-resonance radiation. The calibration constant and beam resolution can be obtained from each of these profiles. For Figure 15a, the calibration constant is given by 448.5/0.8784 = 510.6 kev/ohm. The target width is given by 510.6 x (0.8846-0.8784) = 3.17 kev. Twice the beam width, obtained from the leading edge of the profile, is given by 510.6 x (0.8801-0.8767) = 1.74 kev.

For Figure 15b, the calibration constant is given by 448.5/0.8786 = 510.5 kev/ohm. The target width is 510.5 x (0.9028-0.8786) = 12.35 kev. Twice the beam width is given by 510.5 x (0.8803-0.8764) = 2.30 kev.

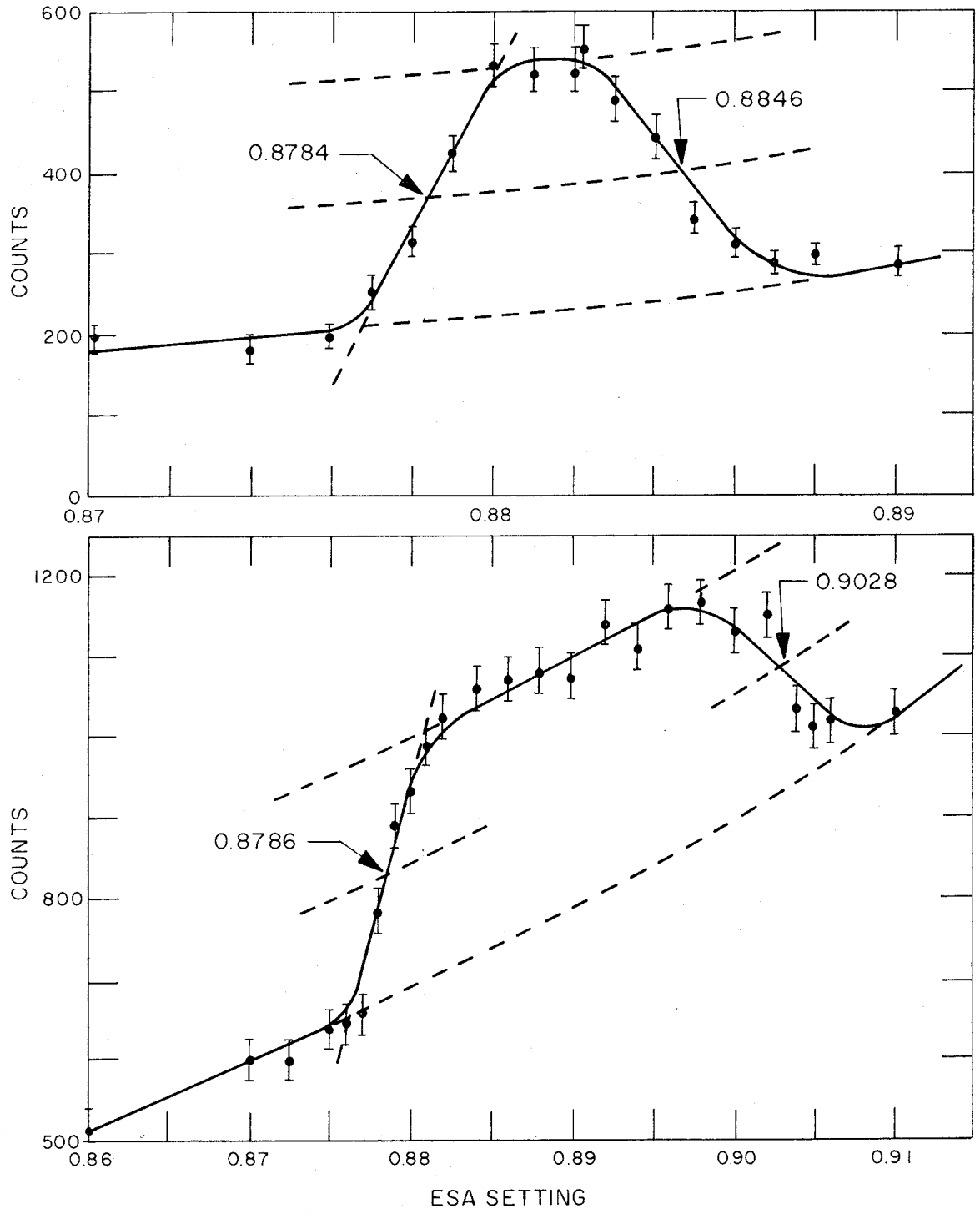
600
400
200
0
COUNTS
0.8784
0.8846
0.87
0.88
0.89
1200
800
500
COUNTS
0.8786
0.9028
0.86
0.87
0.88
0.89
0.90
0.91
ESA SETTING

Figure 16. The experimentally measured $C^{13}(p, \gamma)$ cross section divided by the computed cross section of the 555 kev resonance, using the resonance parameters of equation 3.14. The solid curve is the plot of equation 3.13 with $a = 0.685\ Mev^{-1}$ which was fitted to the experimental points. The error bars are shown only for the low energy points obtained with the mass-two beam. The point at 92.4 kev has been omitted from this plot but would be located at 3.97 ± 1.43.

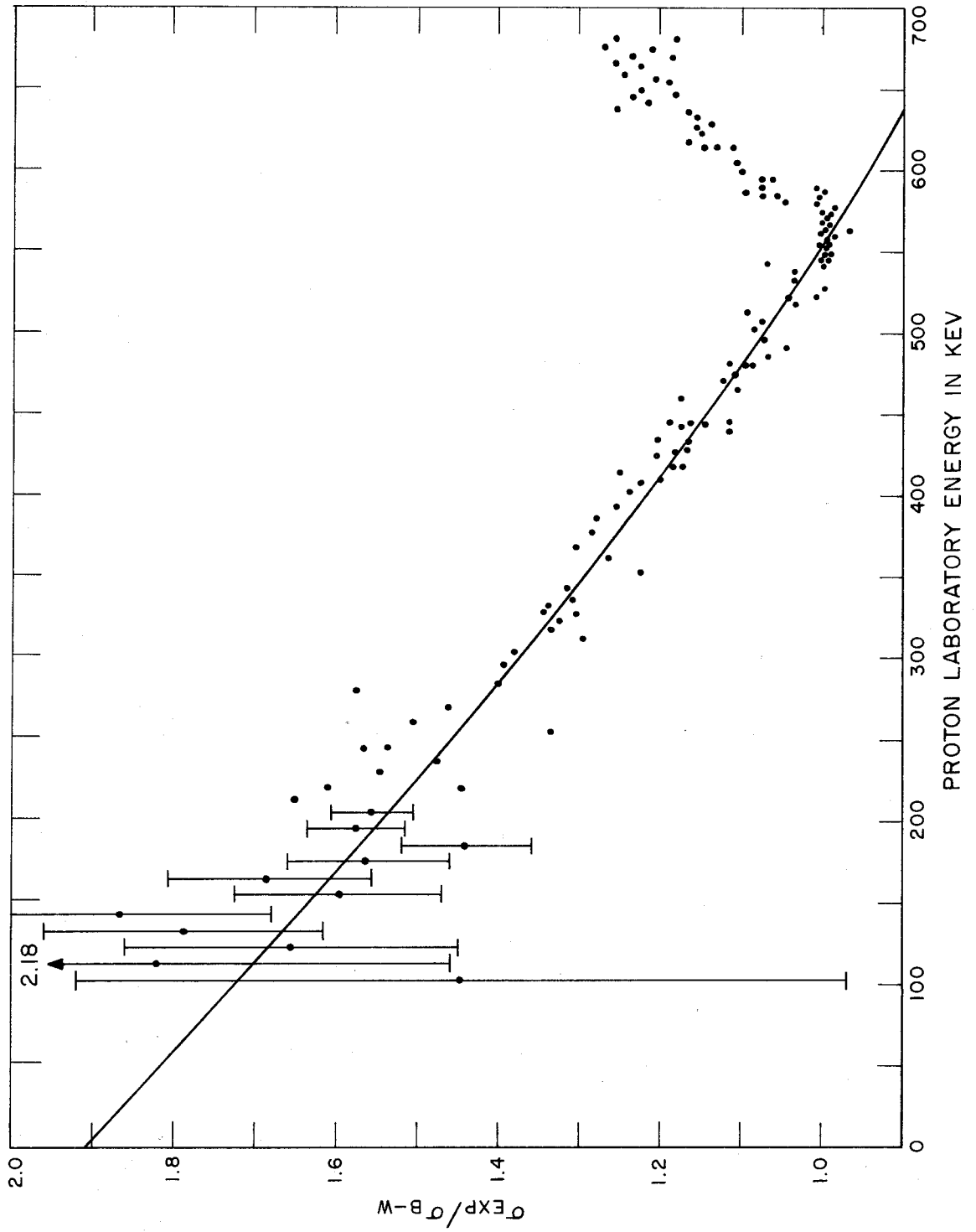
2.18
2.0
1.8
1.6
1.4
1.2
1.0
$\sigma_{EXP}/\sigma_{B-W}$
0
100
200
300
400
500
600
700
PROTON LABORATORY ENERGY IN KEV

Figure 17. The cross section for radiative capture of protons by C^{13} with emission of the ground-state gamma ray is shown. The errors due to counting statistics are shown for the low energy data. The solid curve of this figure is the plot of equation 3.6 multiplied by equation 3.13 with the parameters of equation 3.14. The dashed curve is a plot of equation 3.6 alone.

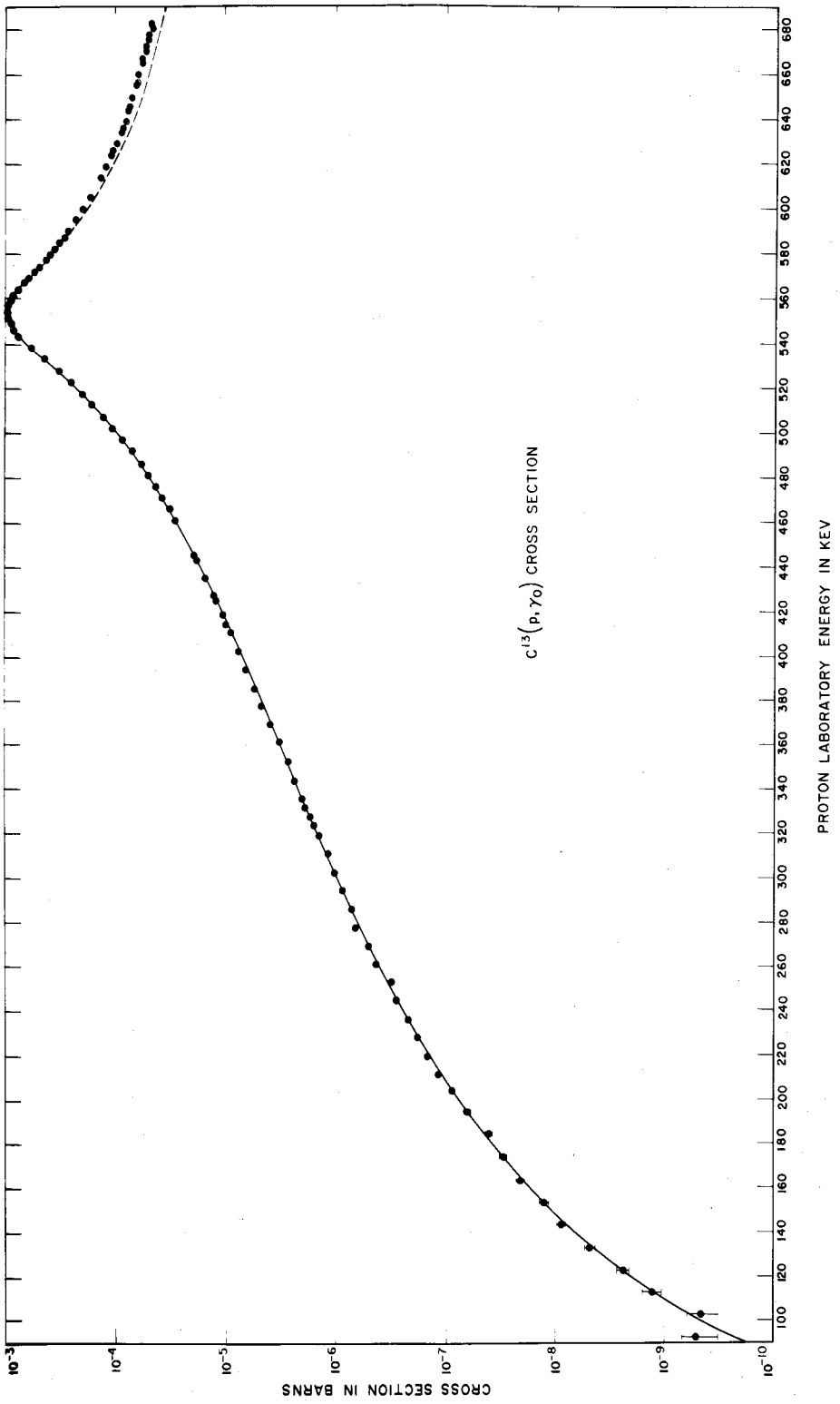
$C^{13}(p,\gamma_0)$ CROSS SECTION
CROSS SECTION IN BARNS
10^{-3}
10^{-4}
10^{-5}
10^{-6}
10^{-7}
10^{-8}
10^{-9}
10^{-10}
100 120 140 160 180 200 220 240 260 280 300 320 340 360 380 400 420 440 460 480 500 520 540 560 580 600 620 640 660 680
PROTON LABORATORY ENERGY IN KEV

Figure 18. A plot of the ratio of equation 5.1 to equation 5.2 for the resonance at 1250 kev in the $C^{13}(p, \gamma)$ reaction. The dashed curve is an attempted fit to the ratio with equation 3.13, which equation provides a 5 percent fit down to proton energies of 500 kev.

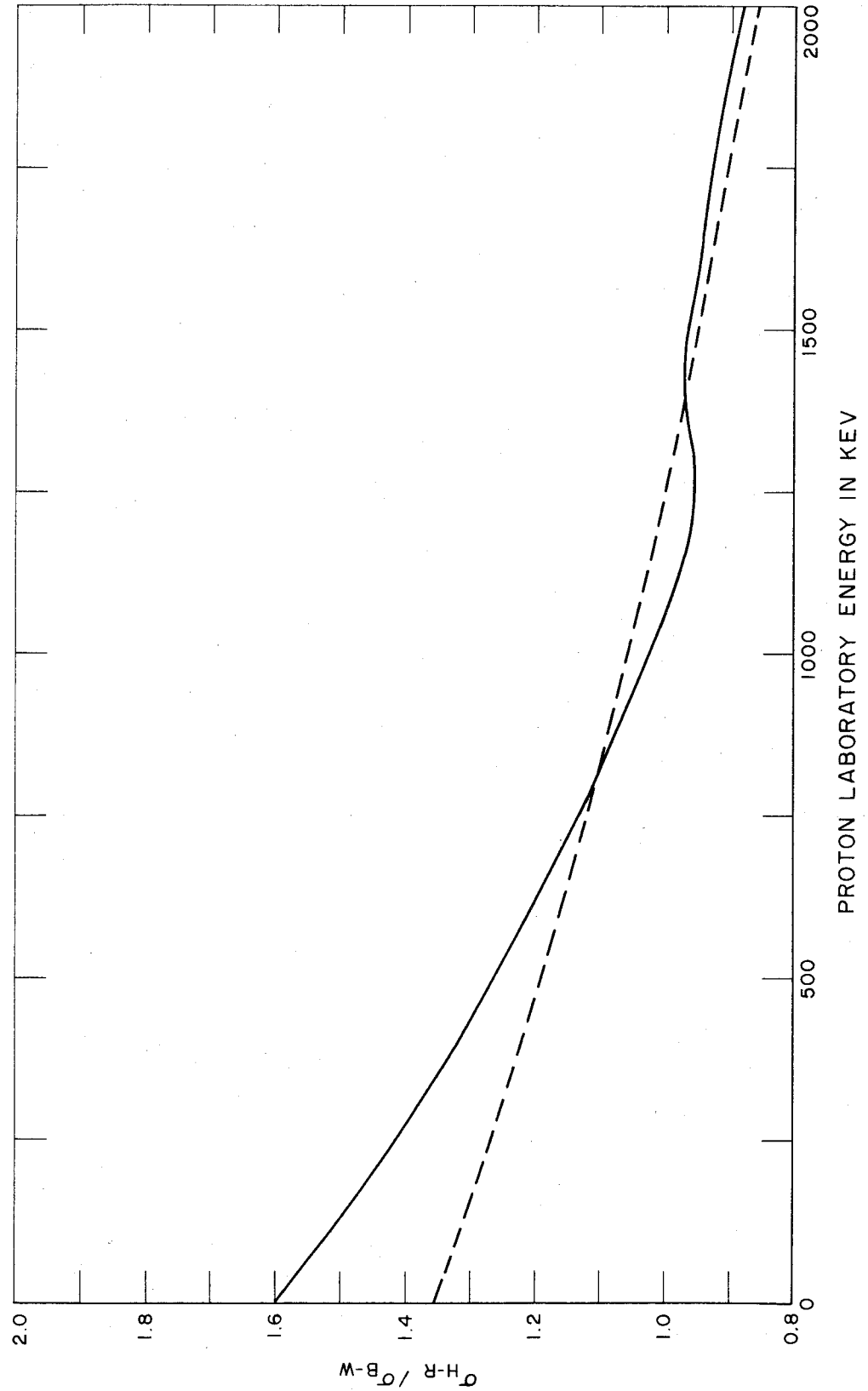
2.0
1.8
1.6
1.4
1.2
1.0
0.8
$\sigma_{H-R}/\sigma_{B-W}$
0
500
1000
1500
2000
PROTON LABORATORY ENERGY IN KEV

Figure 19. A plot of the quantity $-S = (FG' + GF')/(F^2 + G^2)$ where F and G are the regular and irregular coulomb wave functions for s-wave protons incident on C^{13}. The dashed curves are straight line fits to -S at the energies indicated. The sources for this curve are referenced in Appendix II and are the same as those for the penetration factor.

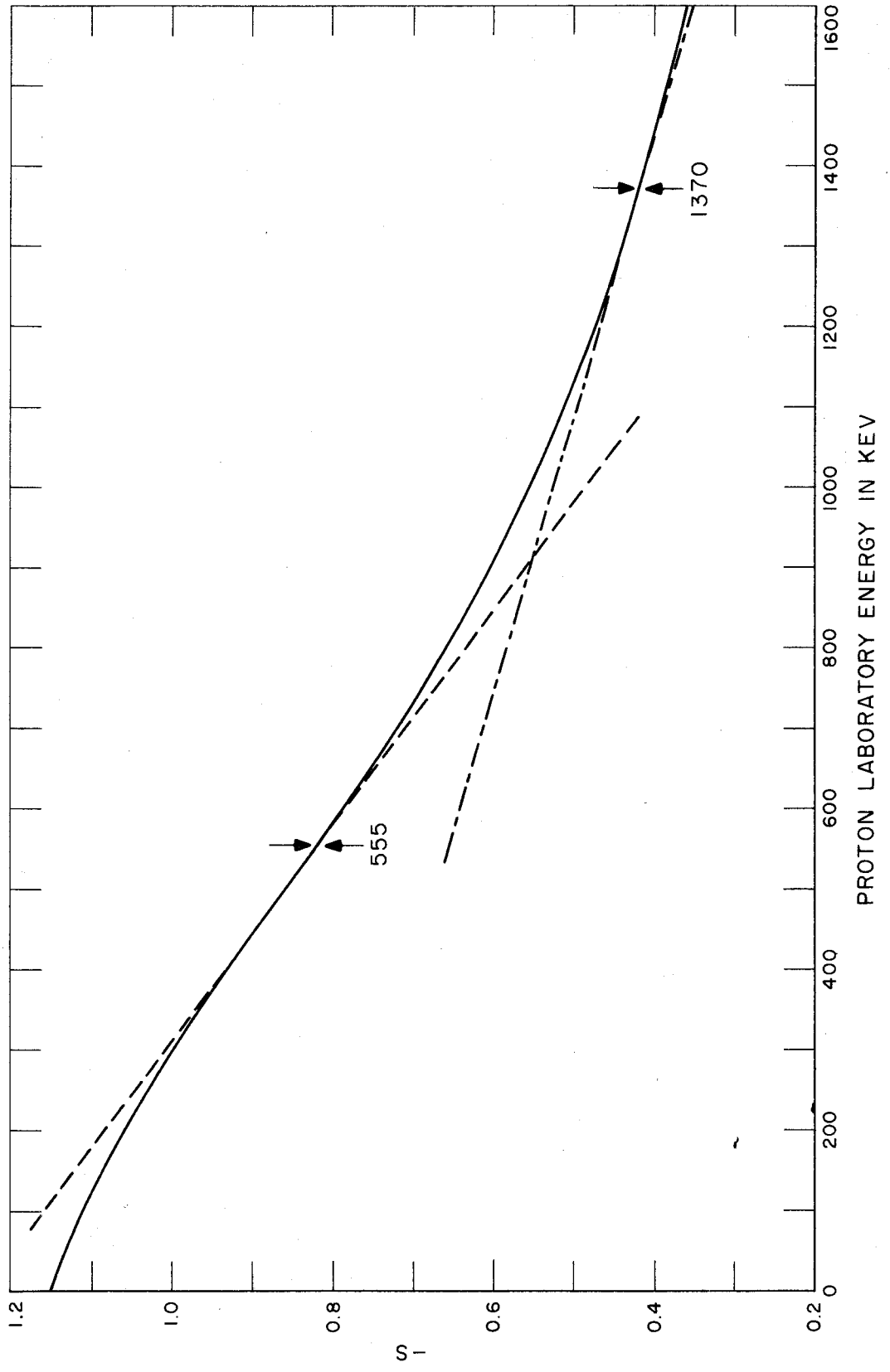
1.2
1.0
0.8
0.6
0.4
0.2
S−
0
200
400
600
800
1000
1200
1400
1600
PROTON LABORATORY ENERGY IN KEV
555
1370

Figure 20. A plot of the ratio of equation 5.1 to equation 5.2 for the 555 kev resonance in the $C^{13}(p, \gamma)$ reaction. The dashed curve is the experimental fit of Figure 16 to this ratio. Note that the energy dependence of the ratio is completely masked by the experimental curve.

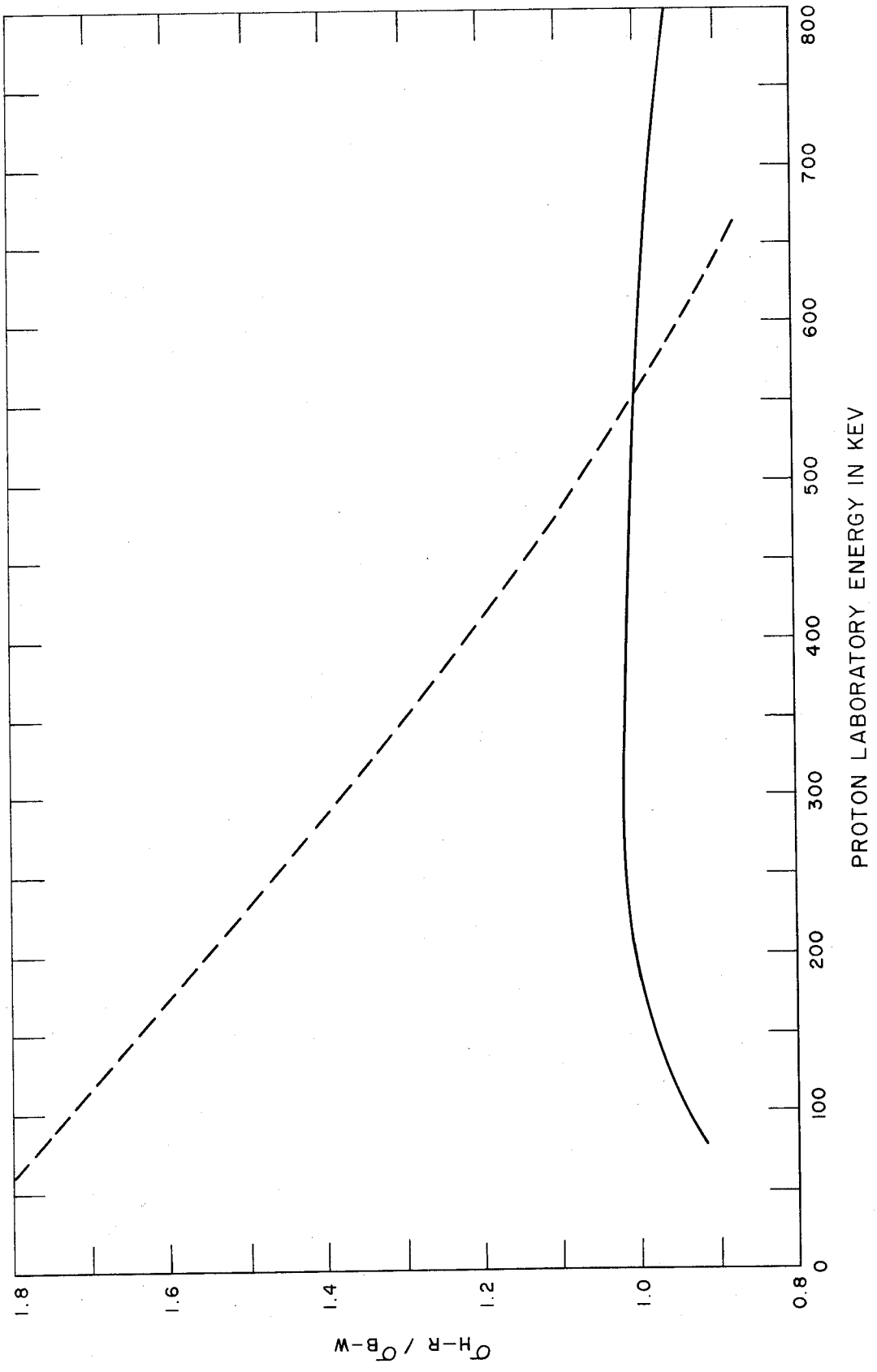
PROTON LABORATORY ENERGY IN KEV
0
100
200
300
400
500
600
700
800
$\sigma_{H-R} / \sigma_{B-W}$
0.8
1.0
1.2
1.4
1.6
1.8

Figure 21. The $C^{12}(p, \gamma)$ experimental cross sections divided by the computed cross section of the 462 kev resonance using the parameters of equation 5.3. The absolute cross sections reported by Bailey and Stratton (1950) by Hall and Fowler (1950) and by Lamb and Hester (1957) have been treated similarly and the results are also shown on this figure. The solid curve, the experimental fit to the data using equation 3.13 with $\alpha = 1.185$ Mev^{-1}, gives the expected form of the deviation from the single level formula and is the best fit to all the points. Although no errors are shown, the deviations from the solid curve of this figure are consistent with the experimental errors over the whole energy range.

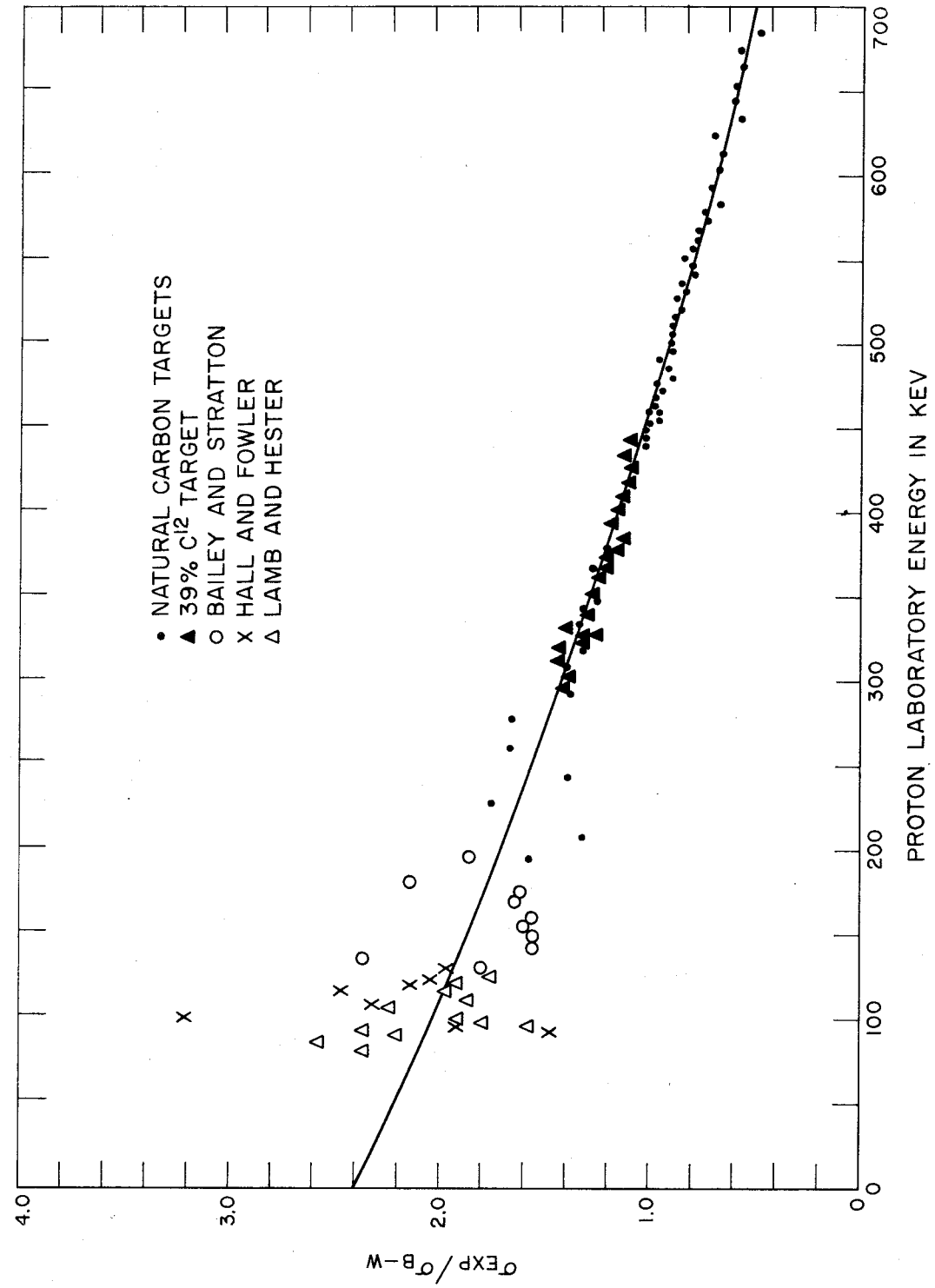
• NATURAL CARBON TARGETS
▲ 39% C12 TARGET
○ BAILEY AND STRATTON
× HALL AND FOWLER
△ LAMB AND HESTER
σEXP / σB-W
PROTON LABORATORY ENERGY IN KEV
0
1.0
2.0
3.0
4.0
0
100
200
300
400
500
600
700

Figure 22. The cross section for radiative capture of protons by C^{12} is shown. The solid curve is a plot of equation 3.6 multiplied by equation 3.13 with the parameters of equation 4.3 and $\alpha = 1.185$ Mev^{-1}. Typical uncertainties are shown at intervals in the energy range.

Figure 23. The cross section factor S(E) in kev-barns is shown for the $C^{12}(p, \gamma)$ reaction. The solid curve is derived from the solid curve of Figure 22 for the cross section and is extrapolated to zero energy.

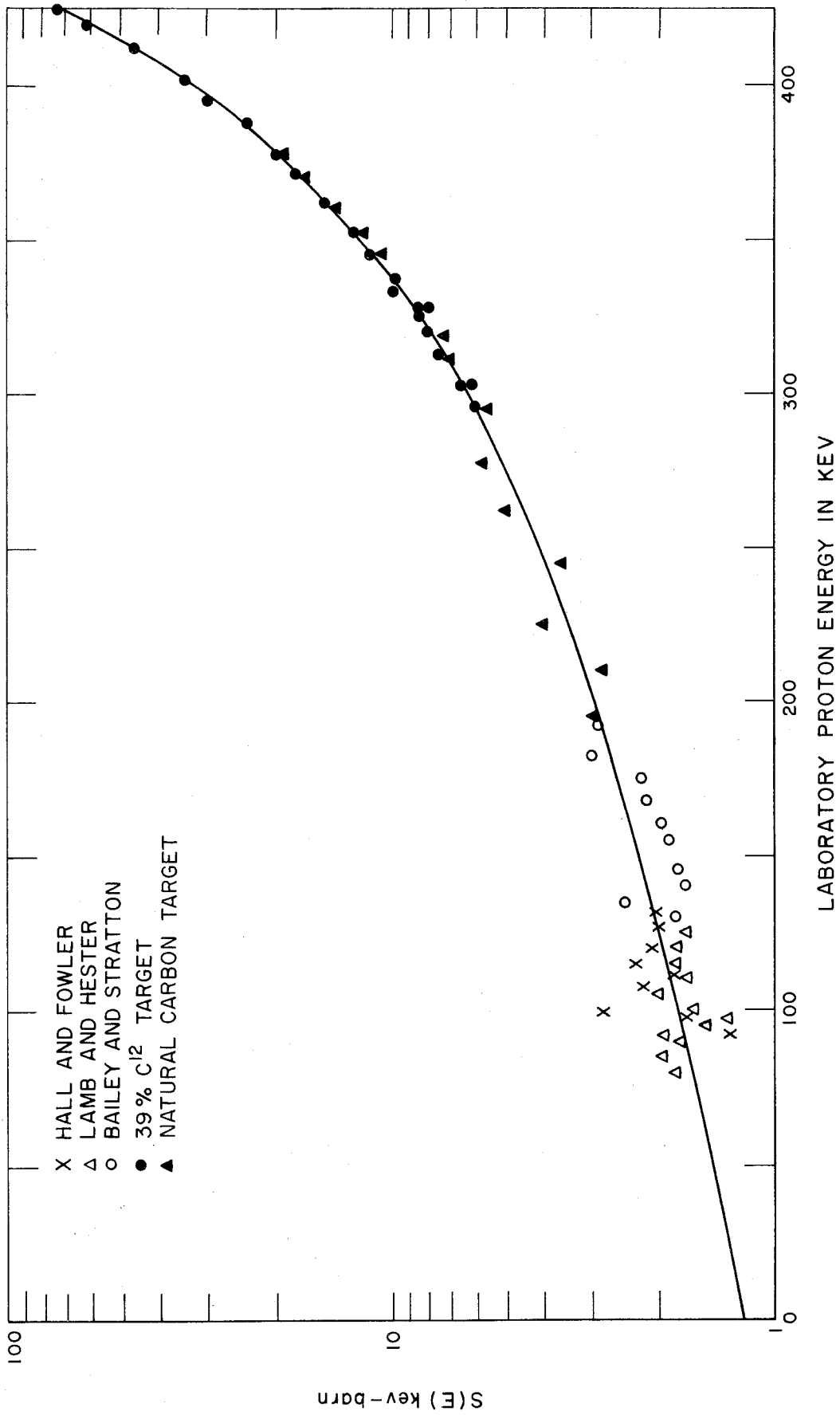
X HALL AND FOWLER
Δ LAMB AND HESTER
○ BAILEY AND STRATTON
● 39 % C12 TARGET
▲ NATURAL CARBON TARGET
S(E) kev-barn
100
10
1
0
100
200
300
400
LABORATORY PROTON ENERGY IN KEV

Figure 24. The cross section factor S(E) in kev-barns is shown for the $C^{13}(p, \gamma)$ reaction. The solid curve is derived from the solid curve of Figure 17 for the cross section and is extrapolated to zero energy. The data points of Hester and of Woodbury and Fowler are also included.

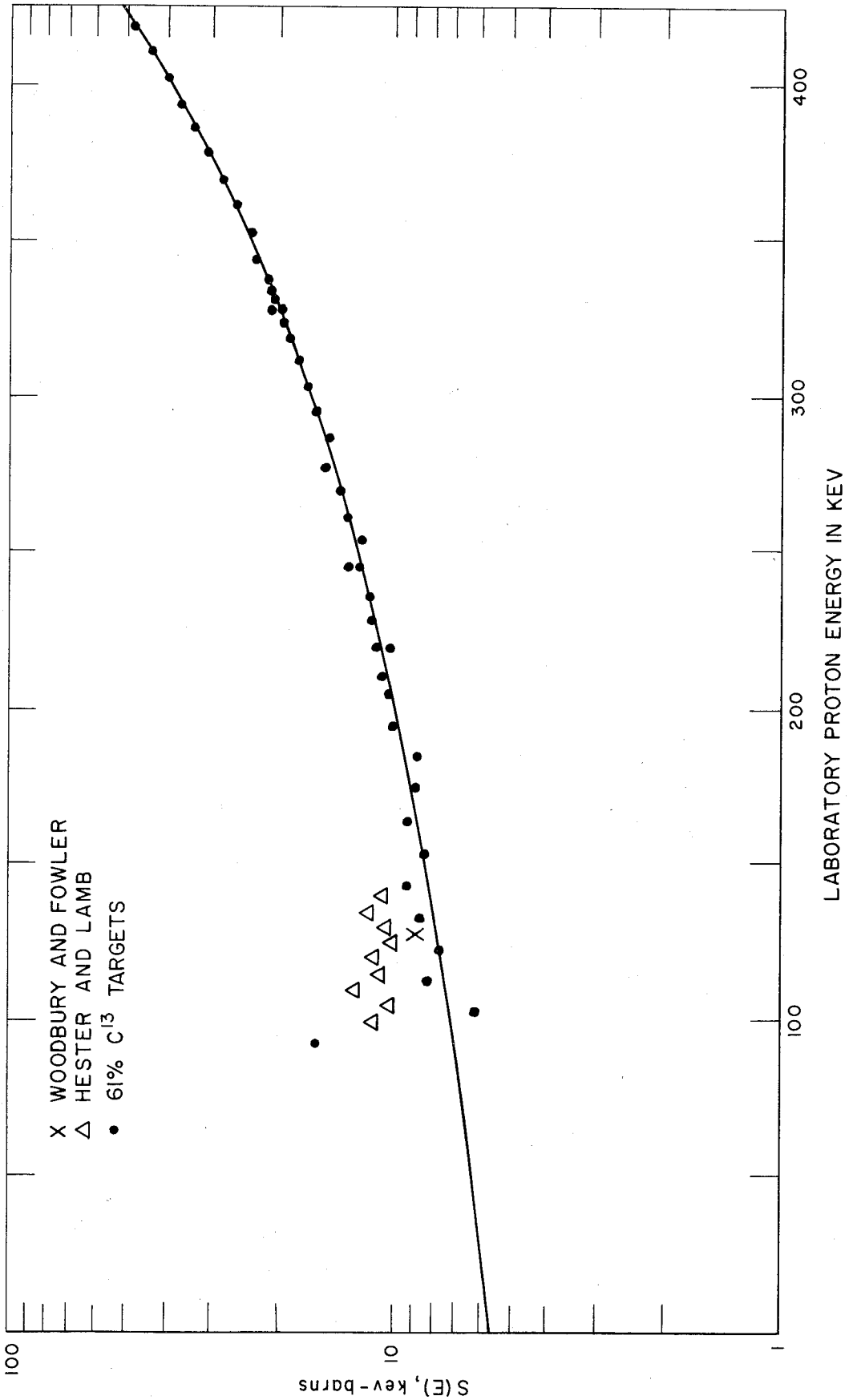
X WOODBURY AND FOWLER
△ HESTER AND LAMB
• 61% C13 TARGETS
S(E), kev-barns
100
10
1
100
200
300
400
LABORATORY PROTON ENERGY IN KEV

Figure 25. A plot of equation 6.7 in which the ratio P_r/P_{nr} has been set equal to unity, and the reduced width to 1 percent of the Wigner limit. A resonance of this width in the region between the solid lines of the figure would dominate the $C^{13}(p, \gamma)$ reaction rate. If a resonance falls above or below these lines, the non-resonance cross-section would dominate the reaction rate. The dashed curve between these limits is a plot of equation 6.5a, the energy at which a resonance would be most effective in increasing the $C^{13}(p, \gamma)$ reaction rate.

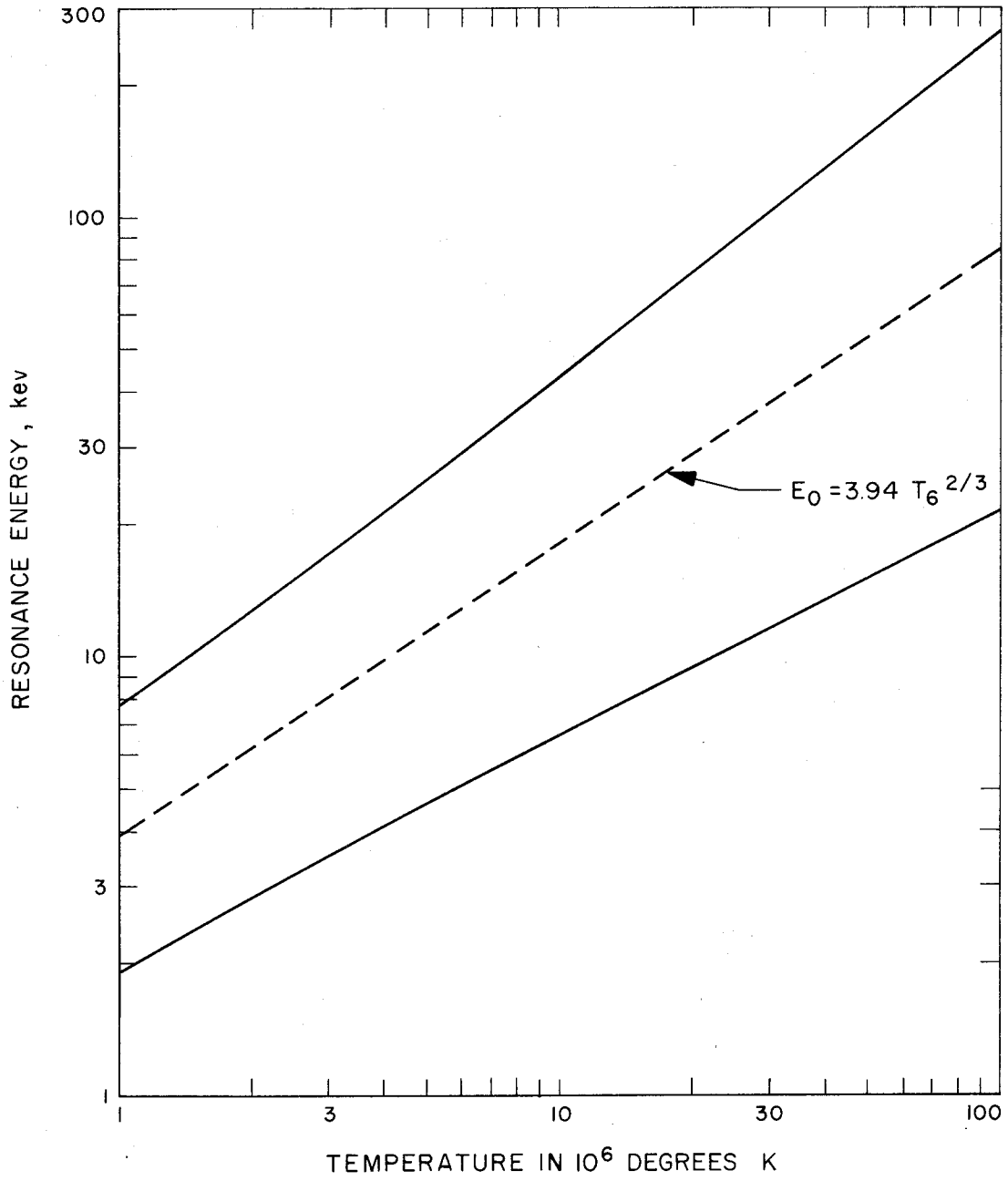
300
100
30
10
3
1
RESONANCE ENERGY, kev
$E_0 = 3.94\ T_6^{2/3}$
1
3
10
30
100
TEMPERATURE IN 10^6 DEGREES K

Figure 26. A plot of the ratio of equation 6.7 for a reduced width of 1 percent of the Wigner limit. The effective thermal energy of equation 6.5a was taken as 25 kev. The dashed line indicates the points at which the resonant and non-resonant reaction rates are equal.

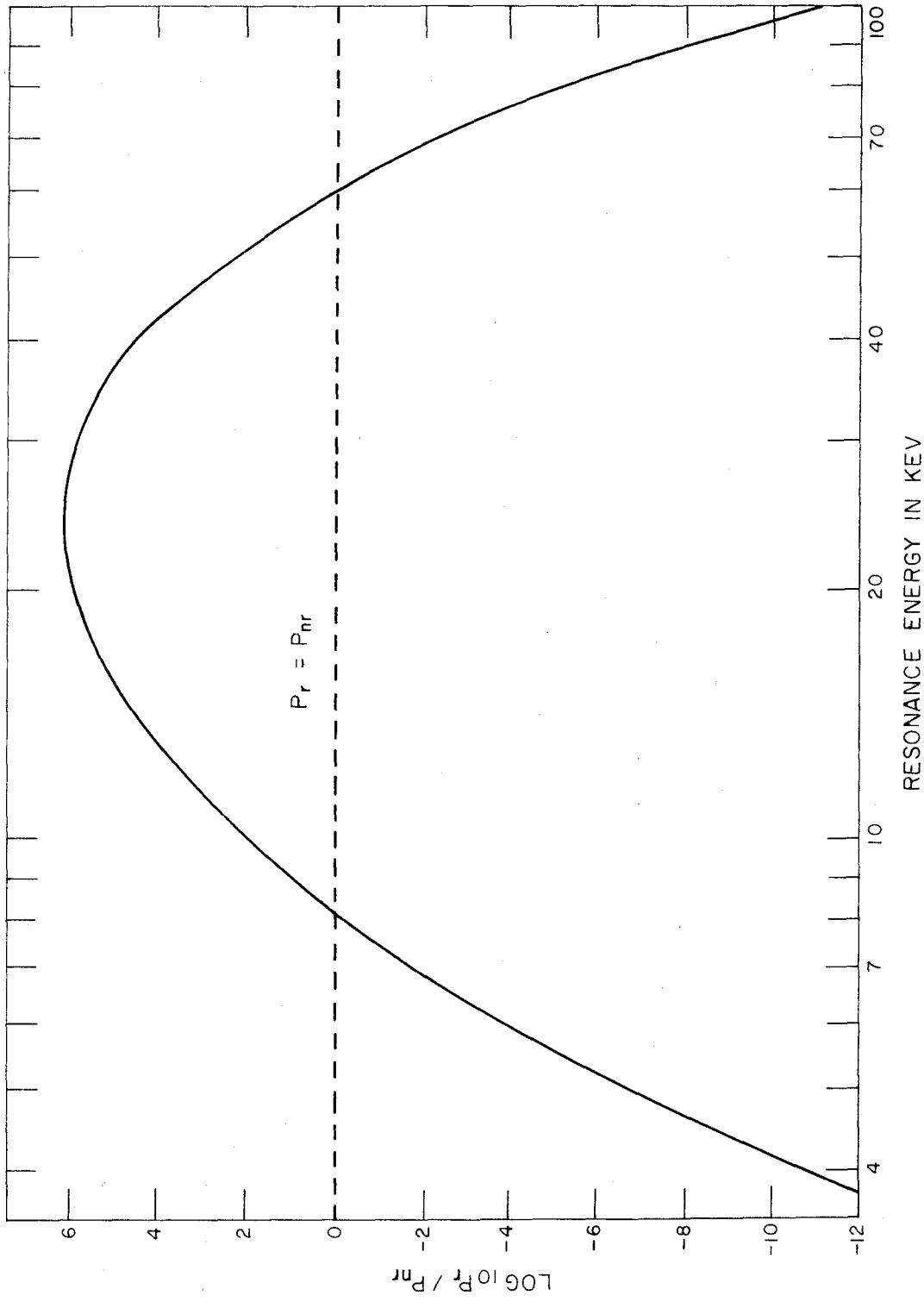
$P_r = P_{nr}$
$\log_{10} P_r / P_{nr}$
RESONANCE ENERGY IN KEV
6
4
2
0
-2
-4
-6
-8
-10
-12
4
7
10
20
40
70
100

Figure 27. The excitation function for the narrow 448 kev resonance in $C^{13}(p, \gamma)$ is shown. All pulses above 3.5 Mev are recorded. The particular run used to determine the upper limit of 400 ev to the resonance width is plotted. The dashed lines show the underlying non-resonant radiation taken to higher energies.

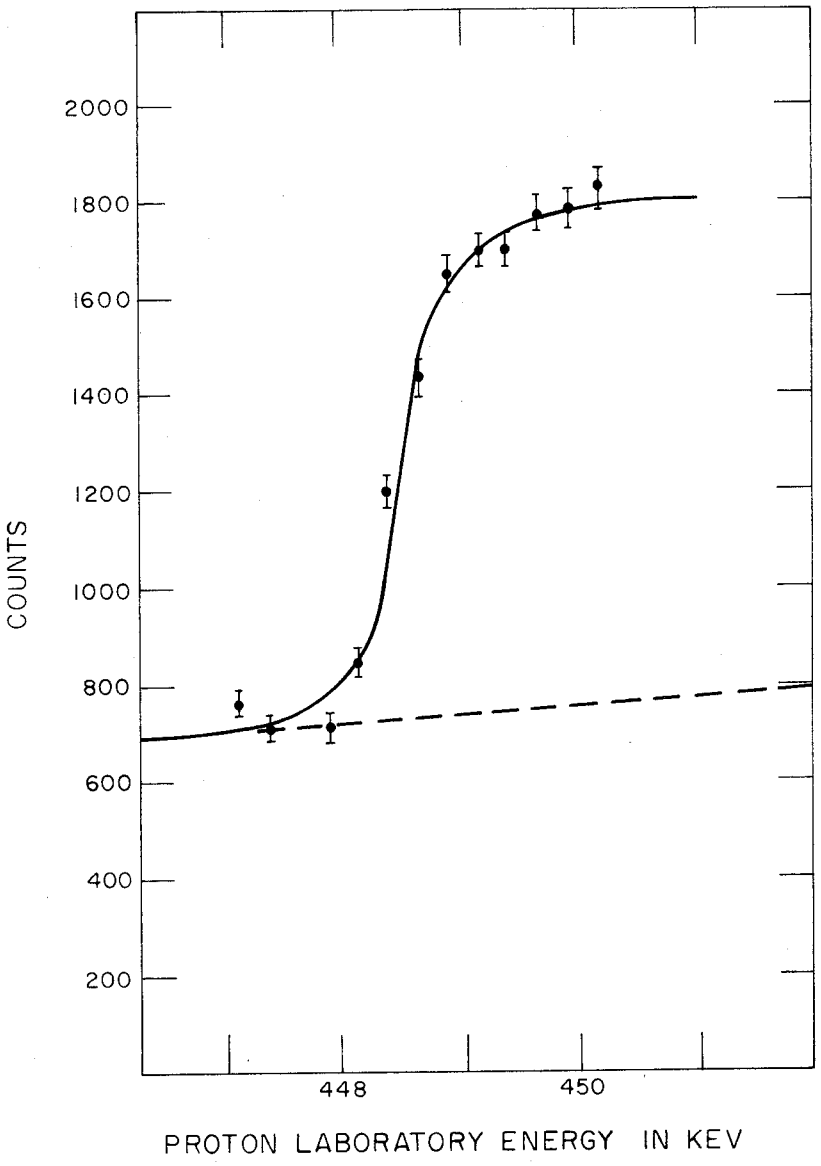
2000
1800
1600
1400
1200
1000
800
600
400
200
COUNTS
448
450
PROTON LABORATORY ENERGY IN KEV

Figure 28. The gamma-ray spectra observed at and below the 448-kev resonance are shown. All the gamma rays marked (except for the K^{40} radiation and the 2.35-Mev gamma ray from the $C^{12}(p, \gamma)$ reaction) are associated with transitions in N^{14}. The gamma rays marked at 5.10 and 5.67 Mev may be weakly resonant, but the peaks observed are explained in the text. The spectra displayed, taken 6 kev apart in energy, represent the yield integrated over a sphere, being the weighted sum of a number of spectra at different angles.

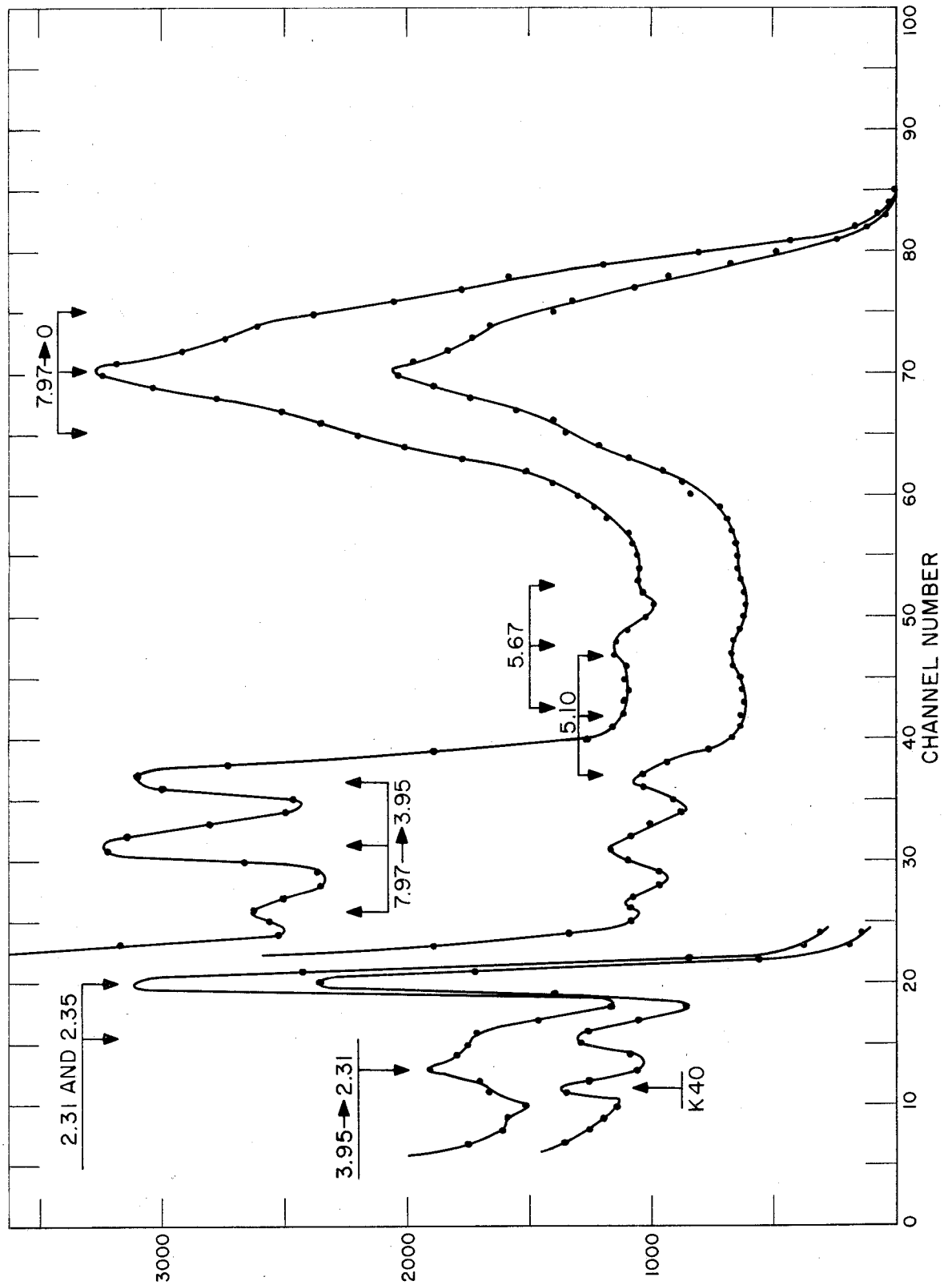
7.97→0
5.67
5.10
7.97→3.95
2.31 AND 2.35
3.95→2.31
K40
3000
2000
1000
0
10
20
30
40
50
60
70
80
90
100
CHANNEL NUMBER

Figure 29. The angular distribution of gamma rays from the 7.97-Mev level (and non-resonant radiation from this energy region) to the ground state is shown. The non-resonant distribution has been renormalized to correspond to the same proton energy as that for which the resonant + non-resonant radiation angular distribution was measured. An absorption correction has been made, but no correction has been made here for the finite solid angle of the detector. The least-squares fit to the experimental points is shown.

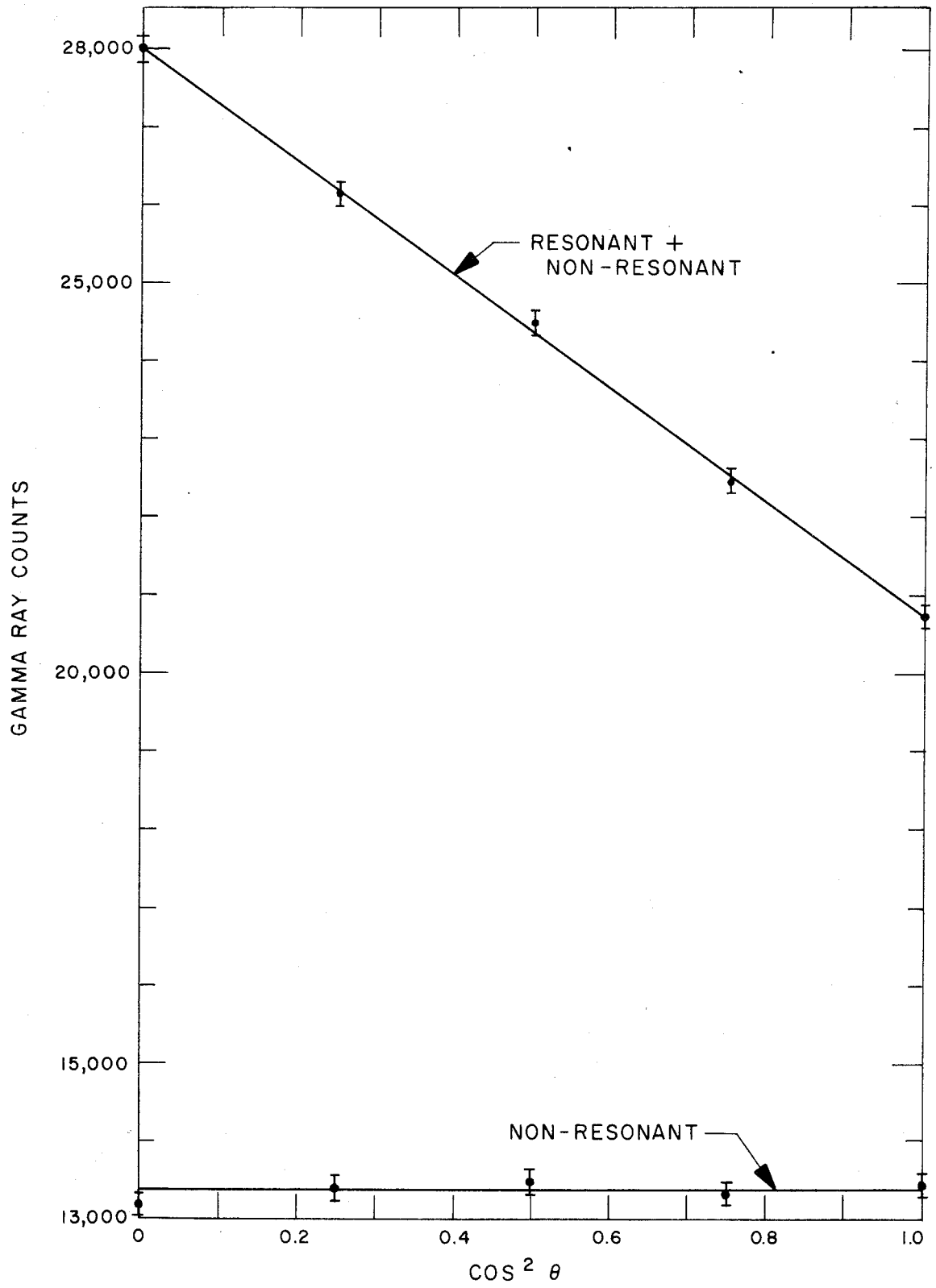
28,000
25,000
20,000
15,000
13,000
GAMMA RAY COUNTS
RESONANT +
NON-RESONANT
NON-RESONANT
0
0.2
0.4
0.6
0.8
1.0
COS 2 θ

Figure 30. The angular distribution of gamma rays from the 7.97-Mev level (and non-resonant radiation from this energy region) to the 3.95 Mev state is shown. The non-resonant distribution has been renormalized to correspond to the same proton energy as that for which the resonant + non-resonant radiation angular distribution was measured. An absorption and electron scattering correction has been made, but no correction has been made here for the finite solid angle of the detector. The least-squares fit to the experimental points is shown.

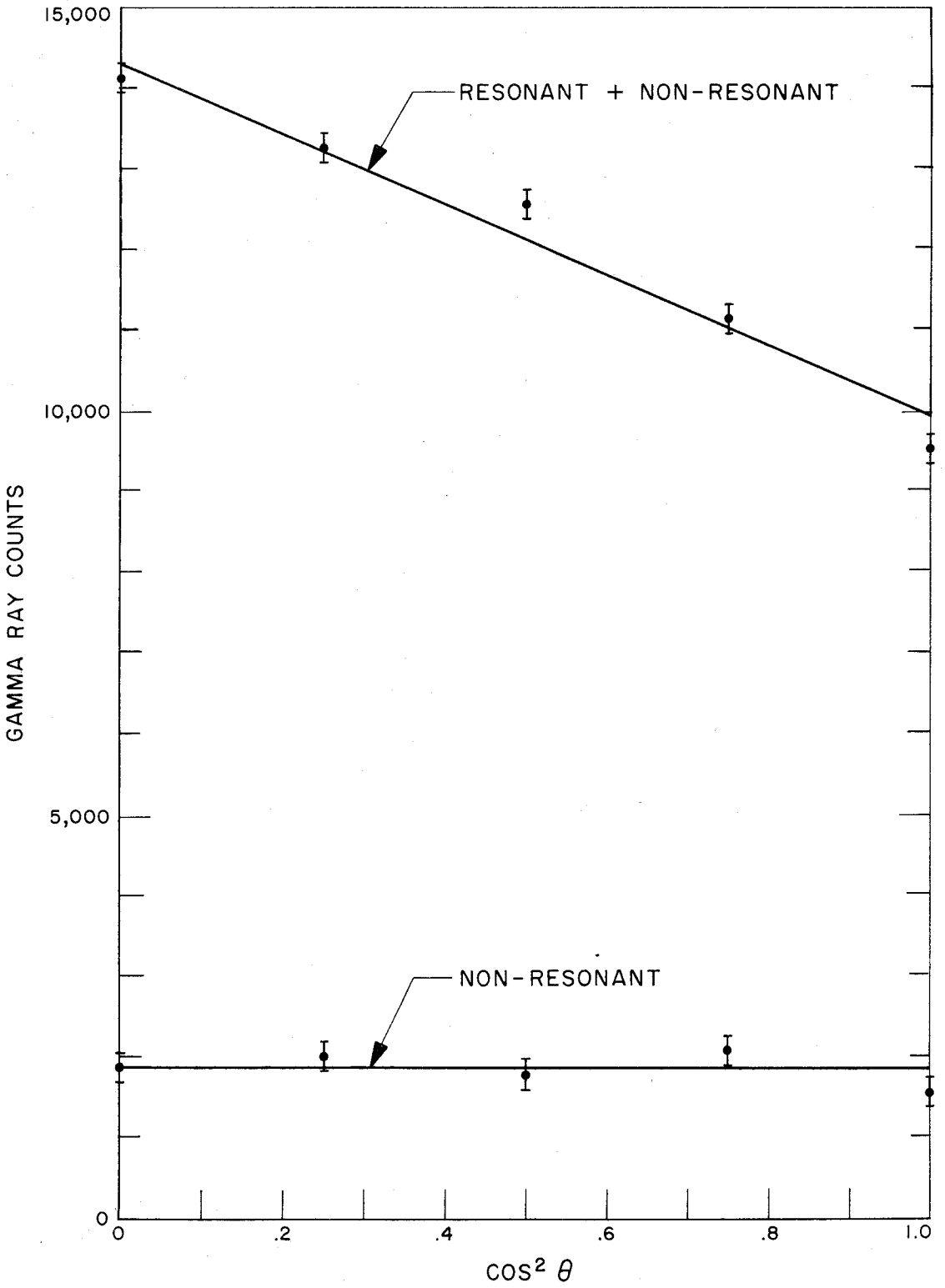
15,000
10,000
5,000
0
GAMMA RAY COUNTS
RESONANT + NON-RESONANT
NON-RESONANT
0
.2
.4
.6
.8
1.0
cos² θ

Figure 31. The relation between δ (the M2/E1 amplitude ratio) and D ($De^{i\phi}$ is the d/s wave amplitude ratio) is shown, for the ground-state gamma ray from the 7.97 Mev level, assuming $J^{\pi} = 1^{-}$. The phase angle ϕ is a further parameter, causing the closed loops on the diagram to expand or contract within the limits indicated. For the expected phase angle $\phi \approx \pm 90^{\circ}$, the diagram is blank, showing that the ground state gamma-ray angular distribution cannot be achieved.

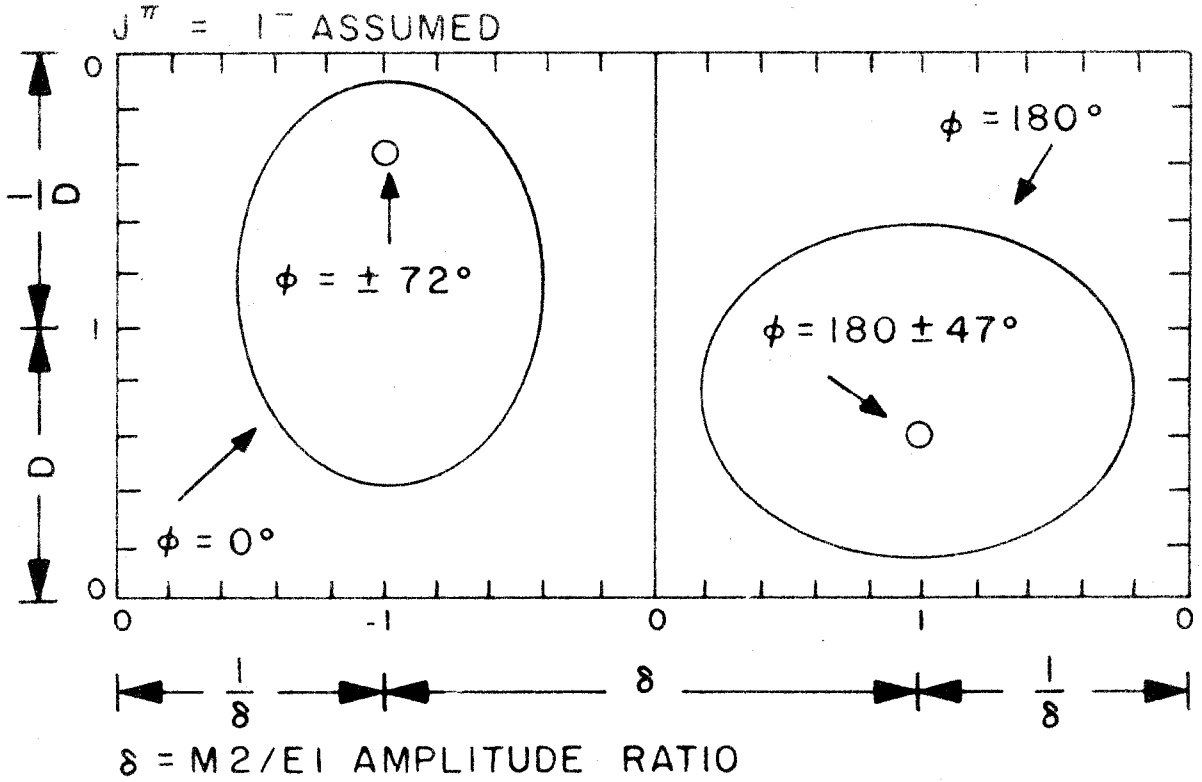
J^{π} = 1^- ASSUMED
0
-1
D
1
D
0
ϕ = ± 72°
ϕ = 0°
ϕ = 180°
ϕ = 180 ± 47°
0
-1
0
1
0
$\frac{1}{\delta}$
δ
$\frac{1}{\delta}$
δ = M2/E1 AMPLITUDE RATIO

Figure 32. Assuming a 1^+ level at 7.97 Mev, the gamma-ray angular distributions to the ground state and the 3.95 Mev state lead to the relation between a_1^2 and δ pictured above. Both transitions must have the same value of a_1^2, and as δ is expected to be small, values of a_1^2 close to 0 or 1 are preferred. From the point of view of angular distributions only, the assignment $J^\pi = 1^+$ cannot be ruled out, but difficulties in accounting for other experiments, as discussed in the text, eliminate this assignment.

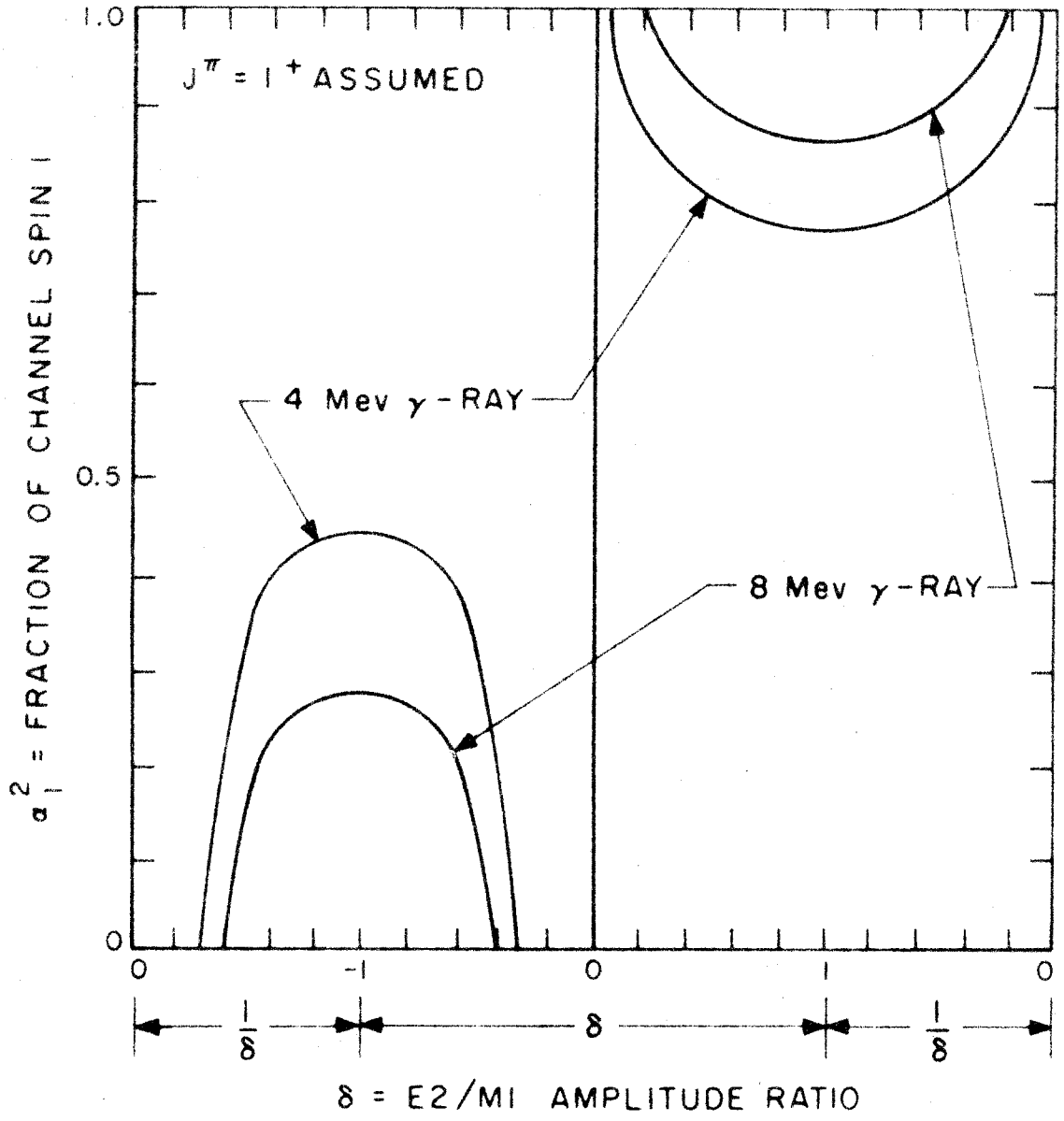
1.0
0.5
0
$J^{\pi} = 1^{+}$ ASSUMED
4 Mev γ-RAY
8 Mev γ-RAY
a_1^2 = FRACTION OF CHANNEL SPIN 1
0
-1
0
1
0
$\frac{1}{\delta}$
δ
$\frac{1}{\delta}$
δ = E2/MI AMPLITUDE RATIO

Figure 33. The preferred assumption of $J^{\pi} = 2^{-}$ for the 7.97-Mev level leads to the relation between δ and a_1^2 shown here. Interference of the 2^{-} resonance with the 1^{-} background (required to explain the groundstate gamma-ray angular distribution) leads to the existence of a third parameter. This parameter is the width Γ_p of the 2^{-} resonance. The diagram contains information for two values of this parameter: one is the experimental upper limit to the width, and the second is the minimum width required by the ground-state gamma-ray angular distribution. Since the M2/E1 amplitude ratio is expected to be small and a_1^2 must be the same for both transitions, the only satisfactory portion of the diagram is close to $a_1^2 = 0.4$, with Γ_p 350 ev. The channel spin ratios for pure $d_{5/2}$ and pure $d_{3/2}$ incoming proton waves are indicated on the diagram.

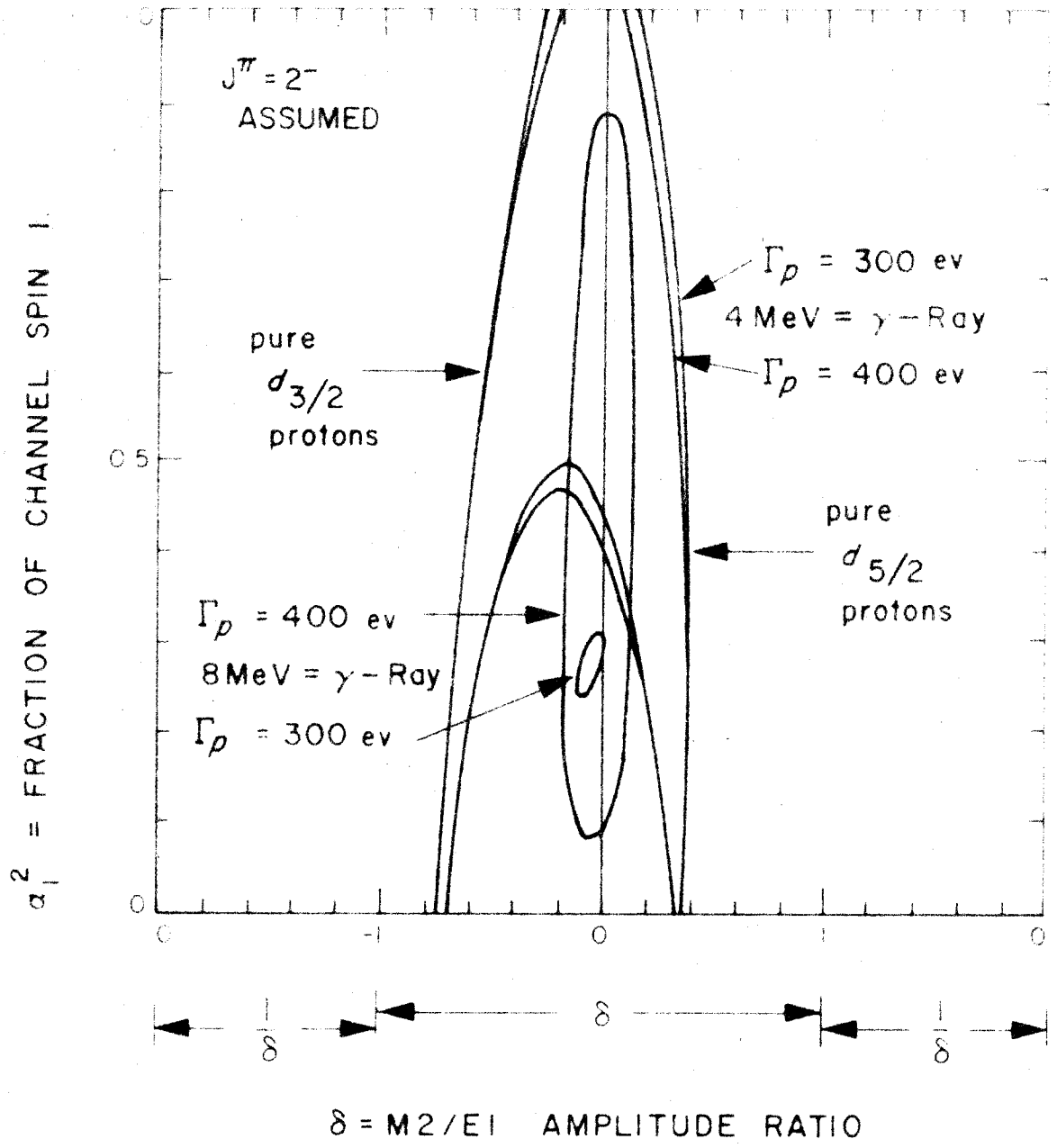
$J^{\pi} = 2^-$
ASSUMED
Γ_p = 300 ev
4 MeV = γ – Ray
Γ_p = 400 ev
pure
$d_{3/2}$
protons
pure
$d_{5/2}$
protons
Γ_p = 400 ev
8 MeV = γ – Ray
Γ_p = 300 ev
a_1^2 = FRACTION OF CHANNEL SPIN 1
0
0.5
1.0
-∞
-1
0
1
+∞
$\frac{1}{\delta}$
δ
$\frac{1}{\delta}$
δ = M2/E1 AMPLITUDE RATIO

Figure 34. The residual penetration factor, $(2\rho/A_o^2)\exp(2\pi\eta)$, plotted as a function of energy for C^{13} + p. The dashed curve is the low energy linear approximation. The solid curve represents the author's bias in fitting the calculated points with a curve that is tangent to the low energy approximation.

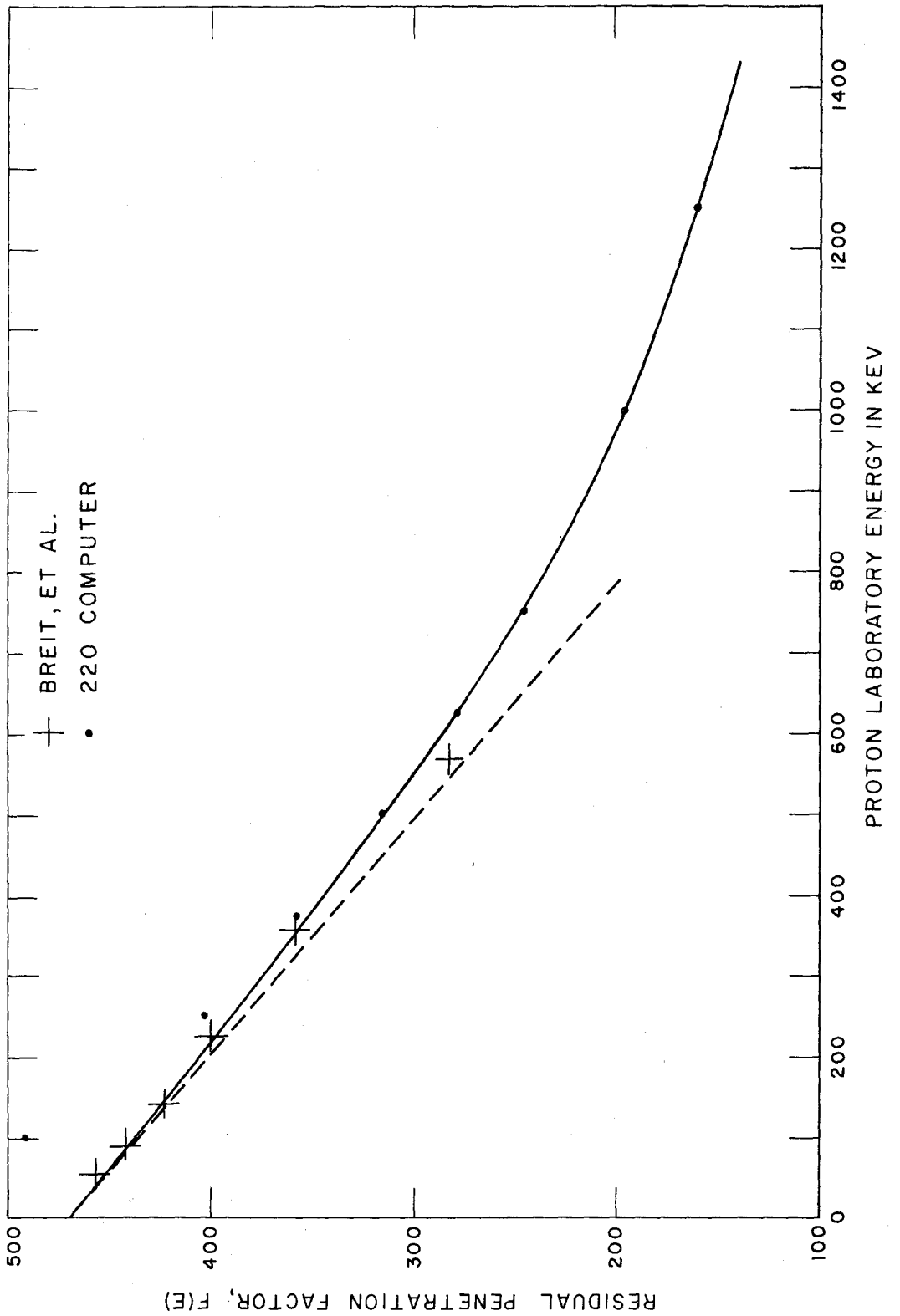
BREIT, ET AL.
220 COMPUTER
RESIDUAL PENETRATION FACTOR, F(E)
PROTON LABORATORY ENERGY IN KEV
500
400
300
200
100
0
200
400
600
800
1000
1200
1400